A STUDY OF SURFACE ZONE DETERIORATION OF NICKEL LEADING TO FATIGUE CRACK INITIATION IN LOW CYCLE FATIGUE

By

JESA H. KREINER

Diplom Ingineur

University of Belgrade

Belgrade, Yugoslavia

1961

Submitted to the Faculty of the Graduate College
of the Oklahoma State University
in partial fulfillment of the requirements
for the Degree of
DOCTOR OF PHILOSOPHY
May, 1979

Thesis
1979D
K92s
cop.2

OKLAHOMA STATE UNIVERSITY LIBRARY

A STUDY OF SURFACE ZONE DETERIORATION OF NICKEL LEADING TO FATIGUE CRACK INITIATION IN LOW CYCLE FATIGUE

Thesis Approved:

C E Price
Thesis Adviser

A. H. Sowa

John C. Lloyd

Ladislaus J. Fila

Norman N Durham
Dean of the Graduate College

1032773

ACKNOWLEDGMENTS

This study depended on help and guidance of many persons as does any complex effort, and this author wishes to express his appreciation to all who made this research possible:

First and foremost, the author wishes to express his appreciation and gratitude to Dr. C. E. Price, the dissertation adviser, for his guidance and unceasing encouragement throughout all phases of this work. Thanks are due to Professor L. J. Fila, for his many helpful suggestions in editing of the thesis.

The Huntington Alloys Company provided the material. The School of Mechanical and Aerospace Engineering of Oklahoma State University provided help in machining the samples and certain parts for the construction of experimental equipment. The Delsen Corporation of Glendale, California, and Northrop Corporation of Hawthorne, California, must be thanked for permitting the author to perform some experimental work in their facilities.

Finally, the author wishes to acknowledge the years of understanding and encouragement afforded to him by his parents, Mr. and Mrs. Herman Krajner, and his wife, Yael, throughout this undertaking.

TABLE OF CONTENTS

LIST OF TABLES

LIST OF FIGURES

NOMENCLATURE

A_L	coefficient of hardening, linear case
A_x	hardening exponent, exponential
b	fatigue strength exponent
B_L	constant, linear case
B_x	coefficient of hardening, exponential
C	fatigue ductility exponent
DPH	Diamond Pyramid Hardness number
H_o	initial hardness in annealed condition
H_v	Vickers hardness
K	cyclic strength coefficient
n	cyclic hardening exponent
N	number of cycles of bending
P_x	hardening exponent, exponential
Q_x	coefficient of hardening, exponential
S	deflection setting
W	indenter weight
$\Delta\varepsilon_T$	total strain range
ε	strain
ε'_f	fatigue ductility coefficient
σ	stress
σ'_f	fatigue strength coefficient

CHAPTER I

INTRODUCTION

It is of paramount importance that phenomena leading to fatigue damage be understood, as fatigue failures represent usual failure in industrial products (15, 18, 27). Major consideration must be given to fatigue in the design of all types of transportation vehicles, power equipment, and so forth. To avoid catastrophic failures from cyclic loading, considerable attention has been given in recent times towards the study of all changes in characteristic features associated with fatigue (45) as shown on Figure 1. The importance of the influence of a few cycles of high loading on a structure cannot be overemphasized (8, 45). It is a frequent occurrence that a temporary overload causes yielding (or macroscopic plastic strains) so that the part will have its life expectancy sharply reduced to below 10^5 cycles, generally referred to as low cycle fatigue (57, 59).

In homogenous metals, fatigue cracks start at the surface except in cases where internal defects exist (43, 52). Cracks commence either from irregularities on the surface which existed prior to cyclic loading or irregularities created by cyclic loading (12, 22, 31, 43, 51).

The environment also plays a significant role - although different environmental parameters have different effects on fatigue strength. For example, while it has been reported by Wadsworth and Hutchins (72) that fatigue behavior of gold at room temperature is unaffected by

absence or presence of air and that small cracks were initiated after the same number of cycles, the same was not true for copper and aluminium. Smith and Shahinian (62) have found that the varying of partial pressures of both oxygen or water vapor resulted in different degrees of surface deterioration. Snowden (64) has concluded that presence of oxygen, nitrogen and water vapor affect fatigue in lead. Masuda and Duquette (44) found that the crack initiation processes are accelerated in aggressive aqueous environments. Crack initiation is also influenced by changes in temperature and strain rate (65). Crack propagation is, as well, affected by the environmental factors (13, 32, 61).

Coffin and Tavernelli (8, 67) have examined the strain hardening characteristics unique to several specific metals. Similar studies and relationships were done by other researchers (58). Quesnel and Meshii (56) investigated localized strain behavior prior to crack initiation.

The effects of fatigue on life of a metal subjected to cyclic loading can be delayed by slowing down the rate of damage accumulation and/or by repair of the affected areas. This repair can be accomplished by removing a layer of material from the surface. Indeed, removal of the material of the affected areas extended the lifetime of the part (51).

Up to crack initiation, pure metals usually workharden to a saturation level at which time initial cracking occurs. These results were reported by Alden and Backofen (1), Davies et al. (12), Young and Grenough (78) and others. Kramer (31) offered an interesting suggestion that the influence of the environment on fatigue consists in affecting the rate of change of properties of the surface, namely the increase of strength of a surface layer with the number of cycles, with

the crack initiation being independent of stress amplitude and environment. The surface layer, as defined by Kramer, refers to a depth approximately 50 - 100 μm underneath the surface. This layer is substantially more affected by the cyclic loading than the remaining volume of the material, as the unconstrained layers at the surface are capable of sustaining much larger strains than the remainder of the material. The existence of the phenomenon of volume saturation hardness has been recognized for some time as indicated by cyclic hysteresis curves but the rate of the hardening process is known to be a function of the amplitude of the imposed strains.

Kramer (31) suggests that after the material is subjected to cyclic stress, the strength of the surface layer goes up, and often, when this stress reaches a critical value, the fatigue crack initiation commences.

For this study, microhardness measurements were utilized to monitor hardness changes at different depths of the surface layers as the fatiguing process went on. This provided assessment of the validity of Kramer's hypothesis. If there existed a critical value of the surface stress, then cracking should commence at the time when this stress level was reached, independent of the nominal strain amplitude. If the surface characteristics varied with depth, then the microhardness readings taken at different depths would show that.

Leiss (39), Nakano and Sandor (50), Plumbridge and Ryder (52) and most of the researchers (9, 13, 47) recognize that it is convenient to divide the study of the fatigue process into the stages designated by Forsyth (20):

Crack initiation which involves microprocesses of different nature than crack propagation.

Stage I - crack growth which is crystallographic in nature.

Stage II - crack growth which is non-crystallographic in nature and primarily controlled by stress-intensity at the crack tip.

The changeover from the Stage I to the Stage II process as shown in Figure 2 is governed by the ratio of shear to normal stress at the crack tip. The same phenomena are found in both low and high cycle fatigue with only the relative length of the respective periods changing.

CHAPTER II

FATIGUE DETERIORATION OF SURFACES/FATIGUE CRACK INITIATION

Most of the research into the fatigue phenomena tends to be qualitative. Its purpose is to describe and interpret the sequence of events which results in fatigue fracture. In order to accomplish that, microscopic examinations of test specimens are made so that presence of cracks may be established at the earliest time, and their behavior closely monitored until the ultimate failure occurs.

Likewise, the microstructure of the material is also subjected to thorough examination with particular emphasis on the effects that cyclic stressing produces so that the type and nature of the damage may be identified. These research studies have been accomplished in terms of microscopic entities such as dislocations (9, 11, 22, 40, 53, 54, 55), slip boundaries (1, 15, 16, 48, 52, 69), environmental conditions (13, 36, 44, 61, 62, 64, 72), etc.

The research into various mechanisms has resulted in a number of major accomplishments. It is known now that the failure is caused by initiation and growth of localized microcracks and that fatigue does not result in a general degradation of material except for fatigue softening of some previously hardened materials. Therefore, the industry has now a qualitative and quantitative indicator of the capability of a material in terms of size and location of microcracks.

Also, of perhaps even greater importance has been the identification of parameters which affect the fatigue behavior of materials (24, 68). A listing of these would include: the surfaces as the most likely site for crack initiation, inhomogenous plastic deformation, e.g. slip bands, grain boundary rumpling, etc., as the predecessors of crack initiation; inclusions and other second-phase particles as stress concentrations within the material which promote crack initiation; the plastic strain amplitude which is highly significant at high loads, the response of material at the tip of the growing crack, e.g., the shape and the size of plastic zone, hardening/softening, plastic relaxation as the controlling influence on the crack growth rates, etc. Each of these parameters has, in turn, provided new areas of research and development on the fatigue problem: surface treatments (shot peening), surface coatings, slip homogenization, removal of inclusions, low-cycle fatigue and the cyclic stress strain curve and the application of fracture mechanics to fatigue crack growth.

A great deal of research effort has been devoted to the investigation of what happens to the material in the earliest stage of the fatigue process, namely prior to the initiation process, as well as the locations where cracks commence and grow as illustrated in Figure 3.

When a cyclic stress is applied to a metal, the individual grains begin to show fine slip markings. As the process of stressing goes on, some of these lines become more visible and easier to detect. These slip bands may extend themselves to the grain boundaries (69). Along with the formation of slip bands, and frequently within them, ridges and depressions (extrusions and intrusions) develop, serving subsequently as the nuclei of the crack. A majority of the contemporary

explanations proposed for the formation of extrusions and intrusions are based on dislocation theory and involve motion of dislocations and particularly cross slip of screw dislocations.

Feltner and Beardmore (15) reported that in germanium, a material in which dislocations will not move at room temperature, fatigue fracture does not exist.

Slip band crack initiation has been investigated by many researchers (1, 24, 36). At low temperatures (less than 0.4 of melting temperature) grain boundary crack initiation appears to arise from geometrical deformation of the surface alone. Crack initiation was observed at as low as 1.7 K. Grain boundary cracking has been observed at almost all temperatures and strain rates (65). It was suggested by Cotrell and Hull (10) that what happens is sliding of material in and out of slip bands thus creating intrusions (grooves). It was also suggested that dislocations traversed back and forth along paths which were shifted in random fashion with respect to previous paths. As a result of this random distribution, the surface acquired a roughened appearance and the stress was redistributed. The later slip occurrences would tend to happen more in the valleys which were formed previously. These valleys would become deeper and deeper and thus eventually result in cracks as shown on Figure 1.

The visibility of the slip bands depends primarily on the stress level and number of cycles. As the stressing proceeds, some of the lines become stronger in at least a portion of their length (15, 36, 68). They do not necessarily extend to the grain boundaries (76). The cracks appear to initiate primarily in these intense bands. While electropolishing can and does remove the lighter slip bands easily, the

removal of the darker ones is much more difficult. These bands are therefore justifiably named "persistent" slip bands. Thompson, Wadsworth and Louat (70) have shown that in copper, a layer of thirty microns deep has to be removed if these are to be polished out. The important feature associated with this removal is that the lifetime of the specimen can be extended almost indefinitely with the periodic removal of surface layers weakened by presence of slip bands.

When fatigue testing is conducted at a low level of stress, some of the slip band markings assume appearances of dots or very short lines. This suggests that at higher stresses, there are more active centers operating. When the stress level is raised, continuous lines emerge.

Laird and Smith (37) postulate that the mechanism of crack initiation at large strain amplitudes is the same slip band form of initiation as at small strain amplitudes but, at the higher strain level, the segment of time spent in emergence of the crack is much shorter. Wood (76), however, is of the opinion that slip bands develop into microcracks only at small strains levels while at higher strains, cracks initiate at grain boundaries.

Watts (74) concluded that while slip bands which were removed through electropolishing do not reappear immediately, when they do reappear, they very much resemble the original bands.

Dependent on the strain level in specimens the hardness saturation will occur at different times of the fatigue process. In low cycle fatigue saturation may occur within the first 10 cycles, while in high cycle fatigue, the phenomenon may take up 50% of the total lifetime (52). In a study of hardness variations caused by cyclic loading,

Davies et al. (12) have shown that saturation occurred during the first 10% of life.

It is worth noting that the surface hardness saturation and bulk hardness saturation happenings do not always coincide timewise. Nakano and Sandor (51) proved that the strain range within the material may be substantially below that one experienced by the surface.

In pure single phase materials, the fatigue crack will commence either at grain boundaries or at prominent slip bands (56). Feltner and Laird (16) have concluded that alloying with substitutional atoms to achieve a more planar slip character will produce a more homogenous slip distribution as well. A detailed description of surface deterioration and crack initiation is given by Alden and Backofen (1).

In commercial multiphase alloys fatigue cracks generally occur in areas of microstructural defects such as inclusions, pores, inhomogenuities and the like (15) as shown in Figure 3. Inclusions represent the most frequently encountered defect. Several factors affect the influence of the inclusion in promoting the crack initiation. These are size of inclusion, its shape, its location relative to the surface, its deformability, properties of the matrix...Role of the inclusions has been studied extensively both for ferrous and non-ferrous materials. Another frequently encountered problem involves gas pores found in materials such as the one shown in Figure 4 where fatigue cracks often initiate.

While slip band crack initiation is common to many metals, the bands where cracking initiates most frequently is at or near the grain boundaries. Grain boundary cracking is a result of the inability of the surrounding grain to flow and deform, and thus accommodate a grain

which is deforming plastically (24, 68). When large strains are encountered within grains due to the motion of slip bands and the grain boundary is unable to take up the strain, a separation at the boundary will originate and a crack will initiate.

When the cyclic stresses to produce deformation of the whole testing specimen, the material may either work-harden or work-soften, depending on its original condition (8, 11). These changes in the material can be detected through a number of methods, the most prominent being: etching, optical microscopy, optical moire fringes, reflective X-ray topography, electron microscopy, microhardness measurements, acoustic emission, Mösbauer effect and other methods. Some of the more recently developed methods which have yet to be widely adopted are holograms, acousto-elasticity, radio-frequency spectroscopy and others.

Results of this study are primarily based on simultaneous use of microhardness measurements, optical and electron microscopy and X-ray diffraction methods.

CHAPTER III

OBJECTIVE AND SCOPE OF RESEARCH

Research Objective

The objective of the research discussed in this dissertation was to examine and clarify the phenomena of surface changes leading to the fatigue crack initiation in Nickel 200 alloy. This research was conducted in a fundamental way in order to discover new information and gain insight into the possible mechanics of the events associated with fatigue crack initiation.

The equipment available at the beginning of this study was a plate bending machine manufactured by Budd Manufacturing Company, Model VSP-150, variable plate bending machine capable of fully reversed bending mode. This machine operates at variable frequencies ranging from 750-2000 Hz. The procedure was to subject a sample to fatigue in fully reversed bending, at a given deflection, for 'N' cycles, then to remove the sample and take hardness readings in the Leitz microhardness tester, reinsert it into the machine, continue the cycling process, remove the specimen again, take microhardness readings and repeat the sequence until a crack initiated. While preliminary tests confirmed the writer's belief that the indentation produced by the microhardness tester did neither affect the behavior of the specimen nor influence any results, the mounting and dismounting of the specimen proved to be

a cause for concern as did the high frequency of the equipment. The specimens could easily get bent or twisted during the mounting process. Furthermore, it was difficult to stop the machine instantaneously with the specimen being in the position of zero deflection. The speed of the machine (750 Hertz) made it difficult to keep close observation on the changes in the surface. The writer felt that the period of interruption of the test was long and that recovery mechanism may hinder the accuracy of the results.

This caused the writer to decide to design, construct and test a compact fatigue testing machine that would be compatible with the Leitz microhardness tester and indeed, mount on its stage. Thus, this became the first major task of this dissertation. The final model not only achieved this objective, but was also sufficiently versatile to be compatible with an optical microscope and an X-ray diffraction stress analyzer. The original scope of work was expanded and monitoring capability transcended from microhardness into recording of residual stress levels and recording of the visual deterioration of the surface through optical and scanning electron microscope photography.

Scope of Research

The actual work in this dissertation was confined to:

1. Development of an experimental testing machine for controlled bending.
2. Conduction of test programs to obtain monotonic and cyclic properties of the material in the fully annealed state. Also, to ascertain if the material conformed with the Manson-Coffin Criterion.

3. Evaluation of strains induced into the material for the specific geometry of the test specimens at the selected initial deflection levels.
4. Conduction of a test program to assess changes in material hardness, increase in residual stresses, observation of the micromechanisms of surface deterioration via optical and electron microscopy.
5. Evaluation of the test results and development of mathematical models which predict the pattern of changes. This work included writing of two computer programs.

CHAPTER IV

EXPERIMENTAL PROCEDURES

Introduction

In order to verify that stress cycling influences the strength of the surface layer of the metals and that when a critical value is reached the crack initiates, a number of experiments were conducted. The material selected for this study was nickel, an f.c.c. metal, because of its importance and wide use in many industrial applications (25).

Experimental work was performed in six major areas. First, the monotonic tensile properties of the material were established. The second task accomplished was the determination of the cyclic properties of nickel. Next, the effects of stress-cycling in low cycle fatigue (LCF) on surface hardness were investigated by conducting fatigue tests on the stage of a microhardness tester. The surface was simultaneously investigated through optical and electron microscopy. Finally, investigation of the residual stresses in the surface through X-ray diffraction analysis was performed.

Experimental Philosophy

The complete experimental program and the associated equipment were developed around a basic approach that fatigue induced deterioration of the specimens can be evaluated through a two-step testing

process. The two steps embodied in this process are: (1) produce bending fatigue damage in a group of specimens under rigorously controlled conditions; and (2) evaluate the deterioration of the surfaces of the specimens by subjecting them to a completely reversed fatigue bending tests. The evaluations of the deterioration of the surfaces were done through means of microhardness measurements, optical and electron microscopy, and X-ray diffraction. Also stress analysis and strain gage methods were utilized. The degree of damage and deterioration of the specimens may be inferred from the magnitude of the difference in the initial state of the specimens and the one existing after the cycling took place.

Experimental Equipment Requirements

Two types of experimental testing equipment are required to perform the two-step test described in the opening paragraph of this chapter. These are: (1) equipment required to produce controlled bending and instrumented to measure important bending parameters; and (2) equipment to assess the damage created by cyclic bending.

The preliminary work leading to this research effort was performed on the Budd VSP-150 variable speed plate bending machine capable of performing fully reversed bending. On this machine it is possible to vary the RPM and, therefore, the frequency as well. Through varying of the eccentricity, the magnitude of the deflection could be varied as well, therefore allowing for the control of the stress and strain levels. The frequency range of 750-1000 Hz was not well suited for low cycle fatigue for two reasons: (1) a specimen would have to be dismounted from the machine for assessment of the damage; and (2) the

speed of the machine would make it almost impossible to stop after a small number of cycles have occurred.

Therefore, an alternate piece of equipment was designed and fabricated fully capable of both precise control of the bending process and allowing for the "in-situ" inspection of the deterioration process. Figure 5 shows this developed piece of equipment - the bending machine.

Material Selection

The material used in all experimental work was Nickel 200 which is commercially pure wrought nickel obtained from the Huntington Alloys Company, Hunginton, West Virginia (26). This nickel was received in the form of cold-drawn bar and strip, from heat number batches #N11E6A and #N2147A, respectively. Upon the machining and surface preparation, the material has been fully stress relieved by annealing. The chemical analysis of the material by weight percentage of nickel is given in Table I.

The choice of this material resulted from the following considerations:

1. Nickel has a rather high strain hardening capacity, hence the potential for large hardness variations during the cyclic stressing. Therefore, the problem of small differences in hardness values for repeat indents is very small.
2. Nickel possesses excellent hardness for the microhardness reading for a wide range of loads commencing with 5 grams through 2000 grams, thereby enabling use of the complete range of the Leitz microhardness tester. In this study indenter weights of 15, 50, 200, 300 and 500 grams were utilized.

3. Nickel 200 is of face centered cubic structure like copper but has not been studied nearly as much (7).
4. It was shown that Nickel 200 regardless of its condition (hard or soft) had hardness ranges well within the capabilities of available equipment.
5. Nickel 200 is a good representative for a multitude of nickel alloys (Monel, Hasteloy, Incoloy, Inconel...) so it is conceivable that many conclusions drawn from this study could be useful in extending them to these (26). All of these alloys are available in many forms and extensively utilized in industry (71). Also, the effectiveness of coatings done with these materials on different base materials would be ascertained under cyclic loading conditions.
6. It has been established that nickel is one of the highest stacking-fault energy metals although its precise value is a matter of discussion. In a recent study, Carter and Holmes (6) found it to be 120-130 mJM^{-2} which is in line with value of 140 mJm^{-2} cited by Hartzberg (24) and Kuska (34), and shown in Figure 6. The stacking faults are planar defects which occur when stacking sequence of identical crystallographic planes is interrupted. For that reason, nickel has essentially undissociated dislocations and that means ease of cross-slip.

Specimens

Prior to preparation of the main group of specimens, it was necessary to establish the geometry of the specimen and the heat treatment

for it. The configuration utilized in the preliminary studies is shown in Figure 7. Subsequently, the geometry of the specimen was altered and its size drastically reduced. The area of the principal interest, namely the neck, was, however, retained. The final geometry of the specimen is shown on Figures 8 and 9. These specimens were utilized subsequently with the Budd VSP-150 variable speed plate bending machine as well as on the specially designed bending machine.

This geometry was chosen for several reasons: (1) stress and strain gradient exist along the gage length of the specimen, thus resulting in a fatigue damage gradient which could be inferred through microhardness changes; (2) the location of failure was predetermined through geometry of specimen but without a considerable stress concentration factor; (3) the same specimen could be used in both low and high cycle fatigue and both with the Budd VSP-150 plate bending machine and the specially designed unit; (4) the specimen would fit the stages of optical and scanning electron microscope as well as under the head of the X-ray diffraction stress analyzer as shown in Figures 22, 23 and 24; (5) all specimens could be machined from one part of one piece of plate, thereby minimizing material variations.

In order to obtain the monotonic and cyclic properties of Nickel 200, specimens were designed and made for the respective tests. Their geometries are shown on Figures 10 and 11, respectively, and are in conformance with ASTM standards. It also became necessary to design special holding grips for the cyclic stress-strain test as shown on Figure 12.

Specimen Preparation

The Nickel 200 used in this experimental work was comercially pure metal donated by Huntington Alloys and was received as cold rolled annealed plate.

In the as-received condition, the Nickel 200 had a rather difficult surface to polish as a result of abrasive blasting and/or pickling processes utilized to remove oxides, scale, tarnish and discoloration (26). The rough surface necessitated a series of polishing operations which were accomplished with decreasing grades of emery cloth (4). All specimens were made by the same machinist in the Oklahoma State University's machine shop and the specimens were essentially identical. The specimens were stored in desiccators.

The heat treatment given to all the polished test specimens consisted of vacuum annealing (≈25Pa) for one hour at 750^{o}C. The heat-up time was 30 minutes. Subsequently, the specimens were furnace cooled overnight. The surface grain size thus obtained was 100-200μm (28). The advantage of this size grains was that it allowed for hardness readings to be taken within individual grains even with loads of 500 grams.

The specimen preparation consisted of coarse to fine sequences. For coarse grinding silicon carbide papers were utilized of increasing fineness, namely: 180, 240, 320, 400 and 600 grit. During the successive grinding operations specimen was held at right angles to the scratches produced on the previous paper subsequently levigated alumina of grade C, then of grade A and finally of grade B were used. Some specimens were etched for pronounced clarity of optical micrographs.

The etchant used consisted of a solution of 50% nitric and 50% acetic acid and equal mount of distilled water. Etching time was 10 to 12 seconds.

Design of the Bending Machine

A significant time of the total effort invested in this research was spent in the design fabrication, and development of the bending machine. The design objectives for the bending machine and the associated instrumentation were as follows:

1. To produce controlled bending on specimens suitable for subsequent damage evaluation.
2. To produce and accurately measure the different levels of deflection of the specimens and the corresponding strain.
3. To have a capability of testing several types of specimens of different geometries.
4. To have the means of recording the numbers of cycles elapsed during testing.
5. To have the capability of stopping the motion at any time during testing for observation purposes.
6. To have the capability of reversing the direction of rotation at any time during testing.
7. To have means of aligning the specimens and ensuring reproducibility of test results.
8. To provide for instantaneous and automatic shut-off once the specimen is broken.
9. To provide for easy replacement of specimens since each test requires a new specimen.

10. To be fully compatible with equipment for evaluation of fatigue damage, i.e., the Leitz Microhardness tester and be easily mounted and dismounted from its stage.
11. To enable optical microscopic monitoring throughout the testing sequence.
12. To be fully compatible with the Rigaku X-ray Diffraction Stress Analyzer.

To meet these design objectives, the unit shown schematically in Figure 13 was designed.

An overall photograph of the machine as mounted on the stage of the Leitz Microhardness Tester is shown on Figure 14. Also shown are the close-up views of the unit and the Rigaku X-ray Diffraction Stress Analyzer in Figures 15 and 16. The complete set of drawings of components for this machine are included as Appendix D.

Development of Procedures and Techniques

The task of cycling a specimen in the fixture shown on Figures 5 and 14 is sufficiently complex so that a relatively brief account of the techniques of setting up a specimen will be presented. While such information may be of limited interest, it should be of invaluable aid to anyone interested in extending the experimental work of this dissertation.

To help understand the following account of procedures and techniques it is suggested that the reader freely refer to Figures 5, 8, 9, 13 and 14.

Let us suppose that the task about to be performed is to cycle a specimen at the deflection setting number S=3 and the initial strain

level of 8480 microinches/inch and at a frequency of 4 rpm and at room temperature and humidity. The environment can be, of course, controlled, as well. The procedural sequence to accomplish that is as follows:

An aluminum test specimen of identical geometry is first installed in the machine so that the proper eccentricity, i.e. deflection level, is set "in situ" with it. Only then a test specimen made of the Nickel 200 is installed.

Subsequently, a carefully prepared specimen, see Figure 8, long side from the neck, is inserted into the grip of the clamp of the machine after it was carefully aligned with the axis of the grip and the specimens pushed inward until the stop groove of the toggle clamp. The clamp is then closed.

The free side (short side from the neck) of the specimen is then gently placed into the groove of the clamp mounted on the base and a machinist parallel alignment block inserted between the toggle clamp and base mounted clamp to ensure identical mounting process and test repeatability. Care must be given during the mounting process so that no axial, transverse or torsional loads are applied to the specimen. The block is now removed and the "on" button activated. The machine begins the cycling process in the 1/2 cycle mode, and later on in the desired mode of operation. The wiring schematic shown in Figure 17 explains the switching sequence. The specimen is now stopped in the horizontal position which may be ascertained through the use of a small leveling device, and microhardness measurement is made. The lens of the microhardness tester is then positioned away from the specimen and the cycling continued until next data point is to be taken.

The relationships between the deflection setting S, force required to effect it, the deflection at the neck of the specimen and the corresponding strain level at the neck are shown in Table II. On Figure 18 it is shown the relationship between the force at the clamp and the neck deflection and on Figure 19 the relationship between the neck strain and neck deflection. The gage utilized for the determination of strains associated with different deflection settings were made by Magnaflux Co. and of the PA-06-045-AA-350 type. These gages are made specifically for the low cycle fatigue.

Limit switches are built into the machine in such a way as to shut the machine off automatically and instantaneously if the specimen breaks.

CHAPTER V

RESULTS

Properties of Material

Monotonic Stress-Strain

Monotonic tensile properties were determined on four specimens. All experiments were performed with a 20,000 lb. Instron testing machine as shown in Figure 20.

The tension tests were performed according to the ASTM E8 standard and the tensile specimens were designed in compliance with the same standard. The geometry and dimensions of the specimens are shown on Figure 10.

The following data were obtained for the Nickel 200 alloy in fully annealed condition.

0.2% Yield Strength = 11,900 psi . . . . . 82.0 MPa

Ultimate Tensile Strength = 57.500 psi . . 396.5 PMa

Modulus of Elasticity = 30.4×10^6 psi . . 209.6 GPa

Strain to Failure = 30%

The monotonic stress-strain curves for the Nicel 200 are shown on Figure 21 and 22.

Cyclic Stress-Strain

The incremental step method proposed by Landgraf, Morrow and Endo (39) was utilized to determine the cyclic stress-strain curve on the Nickel 200 material. With this method, a specimen is subjected to blocks of gradually increasing and then decreasing strain amplitudes to determine the cyclic stress-strain curve. In this manner, the cyclic stress-strain curve can be obtained by the use of one specimen rather than several ones (14). After a few strain blocks, the material cyclically stabilizes. A continuous plot of the hysteresis loops results in a series of superimposed loops and when the tips of the loops are joined, the cyclic stress-strain curve is obtained.

The tests were performed on a MTS closed loop testing machine using 0.5 inch (12.7mm) diameter specimens which had an effective gage length of .65 inch (16.5mm) inch. The strain was applied in a programmed manner and was recorded with a clip-on gage. The testing was done at a constant strain rate of 5×10^{-4} sec^{-1}.

Figure 23 shows the cyclic stress-strain curve for the Nickel 200 alloy obtained by the incremental step method. This method has been shown to have excellent agreement with the conventional method in which the cyclic stress-strain curve is obtained by joining the tips of stable hysteresis loops for several comparison tests at different constant strain amplitude.

The cyclic hardening exponent is defined by the following power relationship between cyclic stress and plastic strain range:

$$\sigma = K \varepsilon_p^{n} \quad (1)$$

where

σ = stable stress amplitude

ε_p = stable plastic strain amplitude

n = cyclic strain hardening exponent

K = cyclic strength coefficient

The following data on the Nickel 200 alloy was obtained.

Elastic modulus E = 27.112 x 10^6 psi	186.94 GPa
Cyclic strain hardening exponent K = 0.118	0.118
Cyclic strength coefficient n = 96 Ksi	661.92 MPa

Strain-Life Curve

Fatigue resistance of a material can be estimated by superimposition of the elastic and plastic strain components. According to Hertzberg (24) based on the work done by Manson and Coffin, the total strain amplitude may be shown by:

$$\frac{\Delta\varepsilon_T}{2} = \frac{\sigma_f'}{E} (2N_f)^{6} + \varepsilon_f' (2\,Nf)^{C} \quad (2)$$

Where:

$\Delta\varepsilon_T$ = total strain range

σ_f' = fatigue strength coefficient

$2N_f$ = number of load reversals to failure

b = fatigue strength exponent

ε_f' = fatigue ductility coefficient

C = fatigue ductility exponent

In case of Nickel 200 the following values were obtained

$\varepsilon_f' = 0.226$

$C = -0.361$

$\sigma_f' = 84400$

$b = -0.0448$

and the total strain life curve equation reads

$$\frac{\Delta\varepsilon_T}{2} = 0.00282\ (2N_f)^{-0.0448} + 0.226\ (2N_f)^{-0.361} \tag{3}$$

The graph showing the relationship between reversals to failure and strain amplitude is shown on Figure 24.

Measurements of Microhardness Variations

The phenomena which bring about deterioration within the surface layers have been studied extensively through a number of methods. Most frequently these utilized both optical and electron microscopy, formation of the slip bands, their rate of growth, developments of the first cracks and associated mechanisms. Dislocation interactions were also of interest throughout this work, with particular regard to type of dislocations, their arrangements, stacking fault energy, strain levels, etc.

It has been demonstrated in a number of investigations that changes in microhardness values closely follow and indicate the damage induced into the materials caused by static and or cyclic loading (1, 5, 12, 18, 22, 23, 29, 30, 56, 58, 60, 79).

Since about 1930 when this type of measurement was introduced both in the United States and Europe, it became apparent that the 136^{o}

diamond pyramid test provided constant hardness numbers irrespective of the load applied with the exception of very light loads. Also, it was noted that the same indenter could be used for all materials from the hardest to the softest.

The indenter is made of diamond and is in the form of a square base pyramid with an angle of 136^{o} between faces (41, 42). The faces are highly polished and free from imperfections. The apex must be point sharp.

The hardness number DPH is given by the formula (42):

$$DPH = \frac{2P \sin\frac{\theta}{2}}{d^2} \tag{4}$$

where

P = applied load (kg)

d = mean diagonal of the indentation (mm)

θ = angle between opposite faces of diamond = 136^{o}

In case of Vickers hardness:

$$H_v = 1{,}854 \frac{P}{d^2} \left(\frac{Kg}{mm^2}\right) \tag{5}$$

With the 136^{o} indenter, the depth of the indentation is approximately 1/7 of the length of the diagonal. The plastic zone underneath the indent extends through a depth of approximately 2d.

Kicks Law (79) is assumed to be valid and in the equation:

$$L = ad^n \tag{6}$$

L = load (kg)

d = mean diagonal (mm)

a = constant

n = constant, usually its value is 2

The relationship between the load and the hardness numbers has been a subject of many investigations but a definitive judgment is yet to be established (42, 78). Young and Rhee (79) reported on work done by Chen and Hendrickson in which they found a decrease in hardness below 5 gram load on surfaces of low dislocation density silver. In a different study, Braunovic and Haworth[6] examined grain boundary hardening of iron and concluded that the hardness was higher at lower loads. Lysaght and DeBellis (42) reported that microhardness values vary depending on the type of measurement taken, i.e. Knoop or Vickers. In the case of Vickers, they found an increase in hardness readings with larger loads. Same was also reported by the makers of the Miniload tester, i.e., Leitz Co.

The hardness readings eventually stabilize within a range in which hardness becomes independent of the load and stays constant. This effect occurs in materials as soft as copper or as hard as hardened martensitic steel. Batchelder (3) reports an increase in Knoop microhardness with the light loads. This investigator found that in all cases, the microhardness values obtained with the 15 and 50 gram loads were always substantially higher than those obtained with the higher value loads.

The possible causes for the apparent increase in hardness numbers obtained with lower value loads may be attributed primarily due to two reasons:

1. Elastic recovery of the material after the load has been removed.
2. Errors in reading small indentations.

Lysight and deBellis (42) reports that differences in appearance may be attributed to design of the testing mach: procedure, geometry of the indenter, vibrations, loading ra ity and the like.

Before this study was commenced, a new indenter tip was purchased for the Leitz Microhardness Tester used and the machine recalibrated and certified. Periodic checks on test block assured uniformity of readings and accuracy of the machine. This was done because it is possible to damage the tip of the diamond and thus obtain erroneous readings with the blunted tip.

The microhardness tester's scale light was always turned on at least 15 minutes before commencing work. In case of very small indents, where they were likely to be more variations in readings, both diagonals were read five times each, the minimum and maximum values discarded and the remaining values averaged. The Leitz Miniload has a limiting magnification of 400x.

Every time an indentation was obtained which appeared grossly distorted, the indentation was repeated. A hydraulic damping mechanism for controlling the rate of descent of the indenter was adjusted to allow an indenter time of 15 seconds which is equivalent in this instrument to an indenter velocity of approximately 33 microns per second. The descent time for the indenter was held constant for the machine at 15 seconds; the hold time is 15 seconds which provided for the total time from activation of the release for the indenting mechanism of 30 seconds. A stop watch was utilized to time each period from the release of the indenter until it was manually raised from the test block by cam rotation. Thus, it is felt, the testing repeatability was

ensured and the influence of dwell time eliminated.

Davies et al. (12) and Kramarenko and Kulikovskaya (29, 30) looked into microhardness as an ideal way to identify fatigue induced changes both quantitatively as well as qualitatively. They found that microhardness is a good indicator up to 75% of the total life. In a recent study, Purcell (55) looked into hardening in front of a growing crack while Grosskreutz (72) studied effects of beryllided surface layers of Ti-8Al-1Mo-1V alloy on improvement of fatigue strength through microhardness measurements. Beisman (6) studied changes of microhardness of ferrite in Low Carbon Steel adjacent to fatigue fractures and found the values to be double that of the initial value. In another Russian study, Hartmut (23) concluded that critical degree of deformation corresponding to the onset of measurable hardening was the same in both static and fatigue experiments. Same study indicated a fourth degree polynomial fit of changes in microhardness versus number of cycles. Robinson and Shabaik (58) have determined that microhardness is a function of the strain. Fila (13) investigated effects of strain amplitude and environment using microhardness as well. Smith and Price (63) evaluated surface behavior of shot peened Nickel 200 subjected to cycling loading via microhardness testing. The results of this study are grouped in graphs showing changes in microhardness as a function of number of flexing cycles and microhardness as a function of test loads. Two complex computer programs were written as a part of the study in order to generate graphs of each case studied involving different deflection settings (five values of S), different indentor weights (five weights, namely W=15 gm, 50 gm, 200 gm, 300 gm and 500 gm) and different number of bending cycles (nine values N=0; 0.5; 1; 2; 4; 8;

16; 32 and 64). A total of 25 test specimens were tested through microhardness evaluation. Five specimens were tested at each deflection level and the data summarized as shown in Appendix C. The numerical results are summarized in Table III. Interpretative plots are given in Figures 25 to 31. The measured data were fitted through exponential and linear approximation and errors were computed for each case.

Figures 25 to 28 show the development of hardness as a function of cycles. Figures 25 and 27 are plotted with linear axes and Figure 26 with log-log axes. Figure 28 shows the example of test data taken at the deflection level S=1 and with the indenter test load of W=200 gm together with their exponential and linear approximation. Figure 25 shows the errors associated with the approximations as does Table IV.

The interpretation of the data shows that a pattern of hardening exists and that the influence of the level of deflection and thus strain imposed, can definitely be established. It is interesting to note that the layers closest to the surface, i.e., measured with the indenter weight of 15 grams, showed the fastest rate of hardening. Higher loads at the same deflection setting showed slower pace of hardening.

The effect of indenter weight on the hardness readings was also investigated reflecting the depth effects of the hardening process. Figure 30 shows the example of the hardness readings after sixteen cycles at the deflection level S=1. The data were fitted both by exponential and linear approximation curves as shown in Figure 31. Table V shows the errors associated with the two approximations.

The relationships between the parameters have been developed and are shown and discussed in Chapter VI entitled Discussion.

Measurement of Residual Stresses by X-Ray Diffraction Method

Since crack initiation and first stage crack propagation occur during cyclic bending in the surface areas which are subjected to the highest stress levels, these areas are monitored and examined by many different methods. One of the methods which is becoming more and more utilized because of its non-destructive nature is the X-ray diffraction analysis (21, 49, 66, 73, 75). The principal advantages which this method offers are: (1) Observations of stress variations can be made during the cycling process. The findings are recorded and documentation is permanent and quantitative. (2) The information originates from depths near the surface (outer 0.002" or 50μm) areas which is the precise location of primary fatigue damages where the fatigue crack initiation subsequently occurs and which is approximate depth of microhardness measurements. (3) Information which is obtained is both microscopic and macroscopic in nature, namely magnitude of residual stress is obtained from peak line position and microstrain and particle size are obtained from the broadening of the lines (21, 49, 73).

The equipment used in this study consisted of the Rigaku "Strain Flex" analyzer and General Electric X-Ray Diffraction Goniometer at the Northrop Corporation facility in Hawthorne, California.

The stress measurements are made through X-ray diffraction in the following manner: The Figure 32 shows the materials in unstressed state, in tension and in compression respectively.

The sets of regularly spaced vertical lines and the near-horizontal lines represent the atomic lattice and its spacing of two sets of equivalent crystalographic planes. When the material is not subjected to any stresses, the lattice spacing is the same, namely d_o for both sets of planes. Under tensile stress, the metal elongates in the direction of the tensile force and contracts in the direction perpendicular to it. These changes in dimensions are reflected in the atomic spacing. The atomic planes near normal to the tensile stress have larger spacing than in the unstressed condition; the planes parallel to the tensile force have a narrower spacing than in the unstressed state. These changes in the atomic spacing cause changes in the angle at which X-rays are diffracted. An increase in atomic spacing results in a decrease in the angle 2θ and a decrease in the atomic spacing results in an increase in the angle 2θ at which the X-rays are diffracted.

These changes in atomic spacing represent the lattice strain and can be related to stress through the following expression (75):

$$\text{Residual Stress} = K(2\theta_{\psi=0} - 2\theta_{\psi=30}) \tag{7}$$

$$\text{Residual Stress} = K \Delta 2\theta$$

where:

K = constant, dependent on elastic constants of material, wavelength of irradiation diffraction peak chosen and angle of X-rays incidence.

K = 36,000 psi/$2\theta^o$ for the case in point, Ni-200

$2\theta_{\psi=0^o}$ = diffraction peak position for planes parallel to the surface

$2\theta_{\psi=30^o}$ = diffraction peak position for planes at the 30^o angle to the surface

$\Delta 2\theta$ = diffraction angle difference

(hkl) = (420) reflection plane of Nickel

Therefore, the method of determining stresses is to find the diffraction peak positions when the sample is irradiated with X-rays at two angles of incidence, (ψ angles). Because conventional diffractometers have one X-ray source and one detector, scans of diffracted intensity versus the diffraction angle are obtained in a step-wise way. First, the incidence angle is set to $\psi=0^{o}$, data recorded and then angle changed to $\psi=30^{o}$ and data recorded as shown on Figure 33.

Figures 15 and 16 show the actual layout of equipment during this testing.

During the testing copper Kα radiation was utilized and filtered with Nickel Foil. Load utilized was 28 KV-9 mA, while the slits were 0.35 mm^{2}. The optics of the goniometer is designed on a parallel beam technique. This method minimizes specimen misalignment effects. Three specimens were tested by this method.

Macrostress Measurements

Instead of calculating the actual macrostresses, it is just as convenient to plot the stress as a function of 2θ displacement. Figure 34 shows the typical 2θ displacement plots for the increasing number of cycles. In each specimen, the stress dropped off immediately and then rises to a fairly constant value within 10 - 20 cycles. The graphical curve approximate a stress strain curve with a yielding occurring shortly into the test. The Figure 34 is also plotted to show the macrostress. A total macrostressing appears to plateau around 15,000

psi (103 N/mm^2). From this data, it appears that, after the yielding or possible grain homogenizing occurs, which takes place shortly after the initial loading, the structure absorbs macrostress until a constant plateau (saturation) occurs. During this time, additional straining is occurring on a micro-level. It is estimated that the accuracy of the method is approximately ± 3000 psi.

Microstrain (Line Broadening Phenomenon)

Microstrain from plastic deformation produces distortion of the crystal lattice and fragmentation of crystals. Microstrains are introduced as small displacements in the atoms of the lattice array in comparison to lattice distortions due to macro-stressing. The microstrain phenomenon is recorded as a diffraction line broadening phenomenon. It is measured by determining the one-half height-width of back reflection place, in this case the (420) plane shown through its Miller indices. Normally, one would expect an increasing microstrain level as a function of the increasing macrostrain. Microstrain runs hand in hand with strain hardening phenomena. The diffraction traces obtained for the macrostress calculations were used to measure microstrain. Figure 35 shows the typical graphical plot of microstrain β versus number of load cycles. However, it appears that some recovery must be taking place between the time to take an X-ray diffraction reading at one number of cycles to the next. The microstrain level drops off and assumes a cyclic nature seen in Figure 35.

Optical Microscopic Studies

Optical micrographs taken in the neck areas of the specimens would

suggest that the deformation occurred by planar slip. An example of slip lines development in Nickel 200 alloy tested at room temperature is shown in Figure 36 a through k. For example, appearance of first slip lines is noted immediately after the commencement of cyclic stressing, i.e., after 1/2 cycles as shown on Figure 36b. As the cycling progresses, the slip lines become more evident in most grains. The slip steps developed both in numbers and severity as the cycles increased. The early cycles contribute a larger number of slip traces than the latter one. A number of six grains was chosen at random and slip trace development followed as the function of number of cycles as shown on Figure 37 and Table VI.

During testing it became evident that there is a difference in appearance between surface appearance of specimens in the annealed and workhardened state. The annealed specimens had slip lines more uniformly distributed throughout the grain and, in several, these did not cross the grain boundaries. The work hardened ones had slip lines less uniformly distributed and were more concentrated adjacent to the grain boundaries, and these slip lines frequently crossed grain boundaries.

The first evidence of crack initiation appears to coincide with attainment of saturation hardness. This was particularly true in the case of maximum deflection (S = 1).

Crack initiation in Nickel 200 subjected to fully reversed bending at room temperature is caused by onset and localization of plastic deformation by slip phenomena. With the formation of slip bands, sharp ridges and troughs develop, thus leading to crystallographic notching of the metal surface. Fatigue cracks initiated within the slip bands as evidence on Figure 36. The initiation of the detectable cracks

coincided with the attainment of saturation hardness at deflection setting S = 1. The locations of cracks which initiated first were almost invariably placed in the zones of maximum strain. It was noted that at highest deflection levels, namely S = 1 and S = 2, cracking was rather segmented along short lengths of slip traces.

The examination of the cracked specimen showed the the crack grew mostly intergranularly as shown in Figure 38 although transgranular growth was noted as well. If the constellation of the grain boundaries would allow it, the crack would sometimes turn from the grain boundary into the slip-bands within a grain and end there as shown on Figure 39.

Electron Microscopic Studies

The structural changes on the surface of the testing specimens were examined by Scanning Electron Microscopy. The microscope utilized was a ISI Super Minisam Model capable of magnifications from 10x up to 100,000x.

The technique which was utilized was based on replication of the surface at selected periods of testing, thus ensuring that the loading arrangement will not be disturbed and that changes at the surface can be observed and interpreted in regular time intervals. The first step in this process involved softening a replicating tape (basically a cellulose acetate film) by applying a replicating solution (cellulose acetate dissolved in acetone) to the tape, and the tape was subsequently pressed on the testing specimen surface. A firm finger pressure was exerted on the tape for a period of 3 minutes until the tape dried, thus reproducing a negative of the morphology of the surface. Following that, the tape was trimmed and placed on a metal slide with the

impression side up. The slide was positioned in a vacuum evaporator and chrome shadowed at 45^{o} angle. Subsequently, gold was deposited normally to the surface of the replica in thickness of approximately 200 Angstroms. During the deposition process, the specimen was constantly rotated in order to ensure a uniform coating thickness. Upon the completion of the deposition process, the slide was removed from the evaporator and directly examined in the Scanning Electron Microscope (SEM) at 1000x and 2000x magnifications. One sample after final test was also examined directly by the Scanning Electron Microscopy. Typical electron micrographs at 4, 8, 16 and 32 cycle tests are shown in Figure 40a through 1.

The Scanning Electron Microscope (SEM) appears to be ideally suited for this type of research investigation because of its large depth of field, its high resolution and the ease with which the magnification may be continuously varied.

The micrographs shown in Figures 40a and 40b were obtained from the replica of the sample subjected to 4 cycles. These show distinct formation of arrays of slip band traces on the surface. It can be noted that most of the area is free of the presence of slip bands. The micrographs shown in Figures 40c and 40d indicate continuation of the phenomena described earlier and more pronounced slip band formation. The slip traces shown here have already a more complex structure than described in previous micrographs.

The next micrographs shown indicate more aggravated deformation processes. The surface deformation is now not only more severe, but also more widespread. The area shown in Figures 40e and 40f shows contours of the metal surface similar to the slipband extrusions and

intrusions described by Wood (75, 76).

In some areas, extrusion of the metal is so pronounced that slip traces are merging together.

The next micrographs, Figures 40g and 40h, show broadening of the slip lines and initiation of intergranular cracks. The surface topography is that of a highly deformed and distorted material.

In the final replicated micrographs of this specimen shown in Figures 40i and 40j it is possible to see secondary cracks which appear to form at the grain boundaries.

The micrographs of the real specimen itself are shown on Figures 40k and 401. They reveal disturbances at the grain boundaries.

The Scanning Electron Micrographs of the fractured specimen showed distinct striation markings generally associated with fatigue crack propagation as evidenced in Figure 41a through 41c. The striations occurred between the ridges. The spacing between striations (which is dependent on the stress level) is found to increase as the distance from the crack initiation site is increased.

Some elongated dimples (due to shear loading) and also equiaxed dimples (due to tension loading) were noted adjacent to the edge of the fracture surface.

Optical Microscopy vs. Electron Microscopy

In this study both optical and electron microscopy were utilized for different purposes. Optical microscopy was utilized for identification of slip bands on the surface and observation of grain boundaries and pits on the surface. The electron microscope was utilized for analysis of the morphology of the surface features once deformation

took place and characteristic patterns developed. The electron microscope was helpful in determining sites of crack origination.

The optical microscopes have three serious limitations: (1) a very limited depth of field makes it very hard to view objects with rough surfaces (which is what occurs after several cycles); (2) the useful magnification of about 2000 diameters restricts the observations to features larger than 0.2 microns; and (3) the magnification cannot be changed continuously. The Scanning Electron Microscope utilized in this study complements it very well. It has an excellent depth of field and greatly improved resolution as well as magnification (3, 24, 33, 52, 65). At the same magnification as the optical microscope the Scanning Electron Microscope has 500 times greater depth of field (3). Surface deformations can be easily discerned from cracks. The morphology of the fatigue surface yielded distinct clues as to when did the fatigue cracking commence as shown in Figure 40. The appearance of the striation of the failed surface as shown on Figure 41 is useful in study of the nature of the crack growth. The Scanning Electron Microscope views of fractured metal surfaces are essentially unique for each different metal or alloy and for the conditions which caused the failure. Thus, the instrument is often used in diagnostic work associated with post morten analyses of failures. Later date Scanning Electron Microscopes have attached X-ray analyzers which are capable of providing instantaneous elemental analyses of the surfaces being viewed.

CHAPTER VI

DISCUSSION

The results of the tests have demonstrated that in the low cycle fatigue fully reversed bending regime of testing fully annealed Mickel 200, the material exhibited a predictable hardening behavior. The pattern of hardening was strongly influenced by the deflection levels to which the specimen was subjected during the cyclic loading. The higher the deflection level, the more rapid pace of the hardening phenomena, as this was illustrated in Figures 25 through 27.

The summary of the experimental test data is shown in Table VI. The data were plotted and analyzed in the form of hardness variation H_v being a function of the number of cycles N for different deflection settings of S = 1 through S = 5.

Also, analyses were made of effects of influence of increase in test load and it was determined that as the size of the indentation decreases a change in hardness will result. The discrepancy in readings goes up as the test load becomes smaller.

The test results were fitted in the forms of linear and exponential approximation and expressions for both cases were obtained as shown in Tables VII and VIII. The exponential fit more accurately reflected the results, as expected.

The expression for exponential approximation model of hardening:

$$H = H_o + B_x \cdot N^{A_x}$$

where,

H = final hardness

H_o = initial hardness in annealed condition (Table III)

B_x = coefficient of hardening for exponential approximation (Table VII)

N = number of cycles

A_x = power law hardening exponent (Table VII).

For example, in case of the deflection setting S = 2 and indenter test load W = 300 grams, we have:

$H_o = 103$

$B_x = 5.35$ (from Table VII)

$A_x = 0.5$ (from Table VII)

Hence, the hardening equation would read

$$H = 103 + 5.35\ N^{0.5}$$

The RMS percentage error in this case is shown from Table VII to be 3.62% for S = 2. The RMS percentage error of test data for the case of test load of W = 300 varies between $3.03 \leq \text{RMS \% EX} \leq 4.99$ indicating a rather satisfactory representation of data.

In the case of linear representation of data, the hardening equation is given as

$$H = B_L + A_L \cdot N$$

where,

H = final hardness

B_L = constant linear case (Table VIII)

A_L = coefficient of hardening for linear approximation (Table VIII)

N = number of cycles

For example, in the same case of deflection setting S = 2 and indenter test load W = 300 from the Table VIII

$A_L = 0.4$

$B_L = 135.50$

giving the hardening equation the format

$$H = 135.58 + 0.40\ N$$

The RMS percentage error associated with this case is given in Table VIII to be 4.37%.

The RMS percentage error in the case of linear representation of test data for W = 300 varies between $4.08 \leq$ RMS % EL ≤ 6.65 also providing satisfactory representation of data.

As it is apparent, either curve provides a satisfactory fit. The exponential approximation, however, may be the preferred one because of the higher accuracy of fit and the tendency of data to plateau at the higher number of cycles.

Also plotted and analyzed were individual hardness data as a function of the test load as well as the exponential and linear approximation of the data (45 total) and error analyses curves were provided for each of these cases. A sample case was included in this dissertation namely for deflection setting S = 1, and after Number of Cycle, N = 16

as shown in Figure 30 and Table V.

The expression for the exponential fit approximation model was developed as well in the form:

$$H = Q_x \cdot W^{P_x}$$

where

H = hardness

P_x = power law hardening exponent (Table IX)

Q_x = coefficient of hardening (Table IX)

W = weight of indentor

For example in case of deflection setting S = 3 and after N = 4 cycles.

$P_x = -0.08$

$Q_x = 211.13$

and the equation would thus read

$$H = 211.13 \cdot W^{-.08}$$

The RMS percentage error in this case is shown in the Table IX to be 1.15%, a rather good fit.

The RMS percentage error of test data for this case, namely at N = 4 cycles, varies between $0.89 \leq$ RMS % EX ≤ 3.44 which represents a satisfactory representation of data.

In the case of linear representation of data, the equation of fit is given as

$$H = Q_L + P_L \cdot W$$

where

P_L = rate of hardening coefficient (Table X)

Q_L = constant (Table X)

W = weight of indentor

For example, in the same case, namely deflection setting of S = 3 and after N = 4 cycles,

P = -0.08

Q = 160.49

and the equation would read

H = 160.49 -0.08 W

The RMS percentage error in this case is shown in the Table X to be 4.21%. The RMS percentage error of test data, namely at N = 4 cycles, varies between $4.13 \leq$ RMS % EL ≤ 5.94 which, while acceptable, is inferior to the exponential approximation.

It would appear from the diagrams that the hardening of the substrata in the early stages of cycling occurs at a faster rate than in the latter part of the cycling.

While either the exponential or linear approximation of data provides a satisfactory fit, the former of the two conforms better with the physical events of the process yielding therefore better results.

The X-ray diffraction study of the structural changes during low cycle fatigue of nickel has shown that both macrostress measurements and analysis of the diffraction line width provides valuable information as to the progress of fatigue damage. The material was shown to be hardened during cyclic loading with respect to macrostress level. On a macrostress level during 10-20 cycles of loading, a softening does appear but controlled cycling shows increased strain hardening until a constant value is reached. This cyclic softening appears to be over

the whole range of microstrain measurements. The phenomena is probably not a relaxation phenomenon since there is no decrease in macrostress measurements. Comparisons of such measurements performed by Nagao and Weiss (49) on SAE 1020 steel (B.C.C. structure) with these measurements on Ni (F.C.C. structure) appear to be quite different. They found cyclic softening in general to be occurring on both macro and micro levels.

On correlating the slip line appearances with hardness changes, it was discovered that the above were detectable almost immediately upon commencement of cycling. The larger the deflection setting, the more pronounced and more numerous the slip lines observable in the optical microscope, and more intense the rate of hardening.

Observations of the appearances of slip lines in a number of randomly selected grains as shown on Figure 37 and Table VI indicated first a progressive intensification of these lines and subsequently while the number of lines stayed more or less constant, the slip effect within these grains grew. Eventually, crack initiation commenced.

While Fila and Price (18) reported discovery of the crack initiation phenomena over a wide range of surface hardnesses, contrary to the general belief that cracking does not commence until saturation hardness is reached, the observations of this study appeared to indicate cracking occurring around saturation hardness. The difference may be attributed to the regime of testing, namely Fila and Price worked in high cycle fatigue while this author's work was done in low cycle fatigue encountering, perhaps, altogether different microstructural processes.

CHAPTER VII

RECOMMENDATIONS FOR FUTURE WORK

While the conducted program generated answers to some important questions it also pointed out to areas requiring further work. The following problems encountered in low cycle fatigue would be of timely interest:

1. An extension of this work on other Nickel based alloys (i.e., Monel, Inconel, Hasteloy, Incoly).
2. An investigation of effectiveness of different surface treatments on retarding surface changes induced by fatigue.
3. A comprehensive X-ray diffraction study of fatigue induced changes within different surface strata and at different strain levels.
4. A more detailed study of surface morphology by utilizing Nomarsky interference contrast microscopy.
5. An investigation of influence of different frequency rates on phenomena of surface changes leading to crack initiation.

The developed equipment is also uniquely suited for study of fatigue crack propagation under constant deflection. Hardness profile in front of the crack tip, plastic zone investigation could be accurately assessed "in situ".

Another interesting observation of the slip encountered is that since Nickel is an F.C.C. metal of high stacking fault energy (7) it

would seem appropriate to encounter wavy slip process (34). However, all micrographs seemed to indicate planar slip.

Attempts were made to establish existence of a "Miner" (46) type cumulative surface damage diagrams but the results were less than conclusive. This writer feels that this may yet prove to be a promising area for future research.

Another interesting observation made through optical microscopy is that the slip lines found in annealed specimens were frequently more uniformly distributed within the grains as opposed to slip lines found in work hardened specimens where the slip lines were generally more numerous and more densely situated around grain boundaries.

CHAPTER VIII

SUMMARY AND CONCLUSIONS

The current chapter reviews and summarizes the most important research results and the interpretation of theses results. The major conclusions are also reviewed.

A Review of the Main Parts of the Research

The research included two main parts. These were:

1. The design and development of a machine for controlled completely reversed bending. The machine is capable of periodic interruptions of the testing for the purpose of monitoring of surface changes via microhardness measurements, optical and electron microscopy and X-ray diffraction stress analysis.
2. Development of a test program during which data were obtained through microhardness measurements, an essentially non-destructive and fully reproducible method of monitoring surface zone changes induced by cyclic loading. These data were obtained for several combinations of deflection levels and indentor weights. The program also included a study of slip line formation and changes in surface morphology via optical and electron microscopy as well as changes in residual stress levels at the maximum deflection setting.

Many other interesting investigations will probably occur to those interested in the surface deterioration phenomena caused by fatigue. All the investigations suggested above could be repeated again for specimens fatigued in a high vacuum, or at elevated temperatures, or at cryogenic temperatures and would thereby find use in a wide variety of design situations. Also, the role of specific adverse environments is a task worthy of examination.

It is hoped that the information generated in this study may provide guidelines for future investigators in this interesting area of research. Hopefully, the future will yield a better comprehension of the phenomena involved, and ultimately, lead to better use of existing materials and development of improved ones.

Summary of Results

1. In Nickel 200 alloy the fatigue cycling produces an initially rapid pace of hardening which subsequently slows down and approaches saturation prior to 64 cycles. An exceptionally hard surface layer does not develop throughout the testing.

2. The increase in hardening can be best approximated by the equation:

$$H = B_x \cdot N^{A_x}$$

where coefficients A_x and B_x can be found in Table VII. A_x has the approximate value of 0.5.

3. The variation of measured hardness values with different indenter loads throughout first 64 cycles can be best represented with the equation:

$$H = Q_x \cdot W^{P_x}$$

where coefficients P_x and Q_x can be found in Table IX. P_x has an approximate value of -0.09 for all materials examined.

4. Optical and electron microscopy observations as well as X-ray diffraction data obtained for the highest strain amplitude series of tests ($N_f \approx 1000$ cycles) indicate that first cracks were observed to appear within 16 cycles, i.e., approximately coinciding with the saturation of hardening.

5. Approximately the same hardness values were obtained both in grains with few slip marks and those with a multitude of them.

Research Conclusions

The most important conclusion reached is that microhardness may be used to predict fatigue effects on the material. In combination with other techniques (microscopy, X-ray diffraction), microhardness studies can provide information on the basic mechanisms of changes in the surface layers.

The equipment developed during this research should be a useful research tool. For example, without any modifications, it could be used to investigate other materials, surface treatments, influence of rest periods, fatigue crack propagation and so forth.

With a few modifications, it could also be made suitable for testing some other variables, e.g., other environmental conditions, other specimen geometries, effect of test frequencies, etc.

A SELECTED BIBLIOGRAPHY

(1) Alden, T. H., and W. A. Backofen. "The Formation of Fatigue Cracks in Aluminum Single Crystals." Acta Met., Vol. 9, (1961), 352-366.

(2) Batchelder, G. M. "The Nonlinear Disparity in Coverting Knoop to Rockwell C Hardness." (Undated report, Engineering Experiment Station, University of New Hampshire, Durham, N. C.)

(3) Becker, Harry C. "Scanning Electron Microscopy." Lubrication, Texaco, Inc., Vol. 61 (July-September, 1975), 37-56.

(4) Beland, R. A. "Metallographic Techniques Used With Pure Nickel." Metals and Materials, Vol. 2 (1968), 54-57.

(5) Besman, A. I. "Microhardness of Ferrite Close to Fatigue Fractures in Low Carbon Steel." Nauchnoisled. Inst. Teknol. Machinostroenniya. 1972, 99-116.

(6) Braunovic, M., and C. W. Haworth. "Grain-Boundary Hardening and Elastic Recovery of Micro-Indentations." Journal of Material Science, Vol. 7 (1972), 763-770.

(7) Carter, C. B., and S. M. Holmes. "The Stacking-Fault Energy of Nickel." Philosophical Magazine, Vol. 35 (1977), 1161-1172.

(8) Coffin, L. F., and J. F. Tavernelli. "The Cyclic Straining and Fatigue of Metals." AIMI Trans., Vol. 215 (1959), 794-817.

(9) Corsetti, L. V., and D. J. Duquette. "The Effect of Mean Stress and Environment on the Corrosion Fatigue Behavior of 7075-T6 Aluminum." Met. Trans., Vol. 5 (1974), 1087-1093.

(10) Cottrel, A. H., and D. Hull. "Extrusion and Intrusion by Cylic Slip in Copper." Proceedings of the Royal Society, Series A, Vol. 242 (1957), 211-213.

(11) Curran, Donald R., Seaman Lynn, and Donald A. Shockey. "Dynamic Failure in Solids." Physics Today, January, 1977, 46-55.

(12) Davies, R. B., J. Y. Mann, and D. S. Kemsley. "Hardness Changes During Fatigue Tests on Copper." (Paper presented at International Conference on Fatigue of Metals.) I. Mech. Eng., 1956, 551-556.

(13) Duquet, D. J., and M. Gell. "The Effect of Environment on the Mechanism of State I Fatigue Failure." Met. Trans., Vol. 2 (1971), 1325-1331.

(14) Endo, T., and JoDean Morrow, "Cyclic Stress-Strain and Fatigue Behavior of Representative Aircraft Metals." Journal of Materials, Vol. 4, No. 1 (March, 1969), 159-175.

(15) Feltner, C. E., and P. Beardmore. "Strengthening Mechanisms in Fatigue." (Publication preprint, Ford Motor Co., Michigan, presented at a symposium on "The Achievement of High Fatigue Resistance in Metals and Alloys" at the ASTM Conference, New Jersey, June 22-27, 1969.)

(16) Feltner, C. E., and C. Laird. "The Role of Slip Character in Steady State Cyclic Stress Strain Behavior." Transactions of the Metallurgical Society of AIME, Vol. 245 (June, 1969), 1372-1373.

(17) Feltner, C. E., and R. W. Landgraf. "Selecting Materials to Resist Low Cycle Fatigue." Design Engineering Division of ASME paper 69-DE-59, as ASMA publication, 1969, 1-12.

(18) Fila, J. A., and C. E. Price. "Surface Zone Hardening During Fatigue of Nickel." (Unpublished report, School of Mechanical and Aerospace Engineering, Oklahoma State University, 1978.)

(19) Fila, J. A. "A Study of the Effects of Strain Amplitude and Environment on the Mechanism of Fatigue Crack Initiation in Nickel." (Unpub. M.S. thesis, Oklahoma State University, May, 1978.)

(20) Forsyth, P. J. E. "Extrusion of Materials from Slip-Bands." Nature, 1953, 171-173.

(21) General Electric Corporation. "Introduction to X-Ray Analysis." Analytical Measurement Business Section, GE AMBS, GEA 8856, 15M (8-69).

(22) Grosskreutz, J. C. "The Effect of Surface Films on Fatigue Crack Initiation." Kansas City, Missouri: Midwest Research Institute, 201-232.

(23) Hartmut, I. "Laws Governing Changes in Microhardness During the Static and Fatigue Loading of Light Alloys." Problemy Prochnosti, Vol. 11 (Nov., 1974), 19-23.

(24) Hertzberg, R. Deformation and Fracture Mechanics of Engineering Materials. New York: John Wiley and Sons, 1976.

(25) Howard-White, F. B. Nickel: An Historical Review, Physical Properties of Nickel. Washington, D.C.: U.S. Government Printing Office, 304-307.

(26) Huntington Alloys Heating and Pickling Handbook. 4th Ed. Huntington Alloys, The International Nickel Company, Inc., 1968.

(27) Jacoby, Gerhard. "Fractographic Methods in Fatigue Research." Experimental Mechanics, March, 1965, 65-82.

(28) Kehl, G. L. The Principles of Metallographic Laboratory Practice. New York: McGraw-Hill Book Co., Inc., 1949.

(29) Kramarenko, O. Yu, and O. R. Kulikovskaya. "Evaluation of Torsional Fatigue Damage From Changes in the Fatigue Properties of Microhardness." Zavodskaya Laboratoriya, Vol. 38, No. 9 (September, 1972), 1126-1129.

(30) Kramarenko, O. Yu, and O. R. Kulikovskaya. "Use of Microhardness Method in Estimating Fatigue Damage." Zavodskaya Laboratoriya, Vol. 38, No. 1 (January, 1972), 80-85.

(31) Kramer, I. R. "A Mechanism of Fatigue Failure." Met. Trans., Vol. 5 (August, 1974), 1735-1742.

(32) Kramer, I. R., and A. Kumar. "The Influence of the Environment and the Surface Layer on Crack Propagation and Cyclic Behavior." Corrosion Fatigue, NACE-2, 1972, 146-163.

(33) Kromp, W., Brigette Weiss, and R. Strickler. "Communications, Direct Observation of Surface Fatigue Damage in the SEM." Met. Trans., Vol. 4 (April, 1973), 1167-1169.

(34) Kuska, M. "Technical Proposal to Study the Effect of Stacking Fault on Microstructural Alterations of Metals During Steady-State High-Temperature Creep." Northrop Corporation, Norair Div., Hawthorne, California, NB 66-368, December, 1966.

(35) Laird, C., J. M. Finney, A. Schwartzman, and R. de la Veaux. "History Dependence in the Cyclic-Stress-Strain Response of Wavy Slip Materials." Journal of Testing and Evaluation, Vol. 3, No. 6 (November, 1975), 435-441.

(36) Laird, C., and D. J. Duquette. "Mechanisms of Fatigue Crack Initiation." Corrosion Fatigue, NACE-2, 1972, 88-115.

(37) Laird, C., and G. C. Smith. "Initial Stages of Damage in High Stress Fatigue in Some Pure Metals." Philosophical Magazine, Vol. 8 (1963), 1945-1963.

(38) Landgraf, R. W., J. D. Morrow, and T. Endo. "Determination of the Cyclic Stress-Strain Curve." Journal of Materials, Vol. 4 (1969), 176-188.

(39) Leis, B. N. "Fatigue Life Prediction of Complex Structures." Transactions of the ASME, Vol. 100 (Jan., 1978), 2-9.

(40) Lukas, P., and M. Klesnil. "Fatigue Damage and Resultant Dislocation Substructures." Corrosion Fatigue, NACE-2, 1972, 118-132.

(41) Lysaght, V. E. Indentation Hardness Testing. Wilson Instrument Division, American Chain and Cable Co., Inc., New York, N.Y. 10017, 1949-1968.

(42) Lysaght, V. E., and A. deBellis, Microhardness Testing. Acco-Wilson Instrument Division, American Chain and Cable Co., February, 1971.

(43) McKinnon, E. A., and B. I. Sandor. "Fatigue of Nickel-Plated Copper." Journal of Testing and Evaluation, Vol. 2, No. 4 (July, 1974), 243-248.

(44) Masuda, H., and D. J. Duquette. "The Effect of Surface Dissolution on Fatigue Crack Nucleation in Polycrystalline Copper." Met. Trans. A, Vol. 6A (January, 1975), 87-94.

(45) Merrick, H. F. "The Low Cycle Fatigue of Three Wrought Nickel-Base Alloys." Met. Trans., Vol. 5 (April, 1974), 891-897.

(46) Miner, M. A. "Cumulative Damage in Fatigue." Journal of Applied Mechanics, September, 1945, A-159 to A-164.

(47) Miska, K. H. "Metal Fatigue: Causes and Prevention." Materials Engineering, June, 1978, 31-33.

(48) Munz, D. "Work Hardening, Slip Band Formation and Crack Initiation During Fatigue of Titanium." Engineering Fracture Mechanics, Vol. 5, No. 2 (March, 1973), 353-364.

(49) Nagao, M., and V. Weiss. "X-Ray Diffraction Study of Low Cycle Fatigue Damage in Plain Carbon Steel." Transactions of the ASME, April, 1977, 110-113.

(50) Nakano, Y., and B. I. Sandor. "High Cycle Fatigue Crack Propagation Rates in Copper." Journal of Testing and Evaluation, Vo. 2, No. 3 (May, 1974), 196-201.

(51) Nakano, Y., and B. I. Sandor. "Fatigue Behavior of Copper With Intermediate Surface Layer Removal." Journal of Testing and Evaluation, Vol. 2, No. 3 (May, 1974), 16-22.

(52) Plumbridge, W. J., and D. A. Ryder. "The Metallography of Fatigue." Metallurgical Reviews, 1969, 119-142.

(53) Pratt, J. E. "Dislocation Substructure in Strain-Cycled Copper." Journal of Materials, Vol. 1, No. 1 (March, 1969), 77-89.

(54) Purcell, A. H., and J. Weertman. "Crack Tip Area in Fatigued Copper Single Crystals." Met. Trans., Vol. 5 (August, 1974), 1805-1809.

(55) Purcell, A. H. "Dislocations and Fatigue Cracking." Industrial Research, April, 1977, 81-84.

(56) Quesnel, D. J., and M. Meshii. "Local Strain Behavior Prior to Fatigue Crack Nucleation." Journal of Testing and Evaluation, Vol. 4, No. 5 (September, 1976), 319-326.

(57) Rastogi, V. "A Machine for Low-Cycle High Temperature Fatigue Testing." Journal of Materials, Vol. 1, No. 4 (December, 1976), 791-807.

(58) Robinson, J. N., and A. H. Shabaik. "The Determination of the Relationship Between Strain and Microhardness by Means of Visioplasticity." Met. Trans., Vol. 4 (September, 1973), 2091-2095.

(59) Romanov, A. N., and A. M. Shcherbak. "Resistance of Nickel Alloy to Deformation and Fracture in Cyclic 'Loading.'" Vestnik Mashinostroeniya, Vol. 55, o. 2, 62-66.

(60) Rybin, V. V., V. A. Likhachev, and A. N. Vergazov. "The Intersection of Grain Boundaries by Slip Bands as a Mechanism of Tough Inter-Crystalline Failure." Fiz. Metal. Metalloved., Vol. 36, No. 5 (1973), 1071-1078.

(61) Smith, H., and P. Shahinian. "Environmental Effects on Fatigue Growth Rates in Silver." Journal of the Institute of Metals, Vol. 99 (1971), 243-247.

(62) Smith, H., and P. Shahinian. "Effect of Oxygen and Water Vapor on the Fatigue Life of Nickel at 300°C." ASTM-STP 462, 1970, 217-223.

(63) Smith, S. P., and C. E. Price. "Surface Zone Hardness Changes in Fatigue of Shot Peened Nickel." (Unpublished report, School of Mechanical and Aerospace Engineering, Oklahoma State University, 1978.)

(64) Snowden, K. U. "The Effect of Atmosphere on the Fatigue of Lead." Acta Met., Vol. 12 (1964), 295-303.

(65) Stadnick, S. J. "Fatigue Crack Initiation as a Function of Temperature and Strain Rate." (Unpub. Ph.D. dissertation, University of Illinois, Urbana, 1974.)

(66) Swaroop, B., and K. Tangri. "X-Ray Studies on Residual Lattice Strains in Deformed Nickel." Trans. of Met. Soc. of AIME, Vol. 245 (January, 1969), 61-65.

(67) Tavernelli, J. F., and L. F. Coffin, Jr. "A Compilation and Interpreation of Cyclic Strain Fatigue Tests on Metals." (Paper presented for the 40th Annual Convention of the Society, The American Society of Mechanical Engineers, October, 1958.)

(68) Tetelman, A. S., and A. J. McEvily. Fracture of Structural Materials. New York: John Wiley and Sons, 1967.

(69) Thompson, N. "Experiments Relating to the Basic Mechanism of Fatigue." Proceedings of the International Conference on Fatigue of Metals, 1956, 527-535.

(70) Thompson, N., H. N. Wadsworth, and N. Louat. "The Origin of Fatigue Fractures in Copper." Philosophical Magazine, Vol. 1 (1956), 113-126.

(71) Tillack, D. J. "Advances in Nickel Alloys for Aerospace Applications." SAMPE Quarterly, Vol. 9, No. 1 (October, 1977), 1-5.

(72) Wadsworth, N. J., and J. Hutchings. "The Effect of Atmospheric Corrosion on Metal Fatigue." Philosophy Magazine, Vol. 3 (1958), 1154-1166.

(73) Wan, C. M., and J. G. Byrne. "Correlation of X-Ray and Electron Microscopic Studies of Fatigue." Int. Journal of Fracture, Vol. II (1975), 251-255.

(74) Watts, D. F. "A Mechanism for Production of Intrusions and Extrusions During Fatigue." Philosophical Magazine, Vol. 14 (1966), 87-95.

(75) Weinman, E. W., and J. E. Hunter. "GMR, Fastress, An Automatic X-Ray Stress Analyzer." (General Motors Corporation undated report.)

(76) Wood, W. A., S. Cousland, and K. R. Sargent. "Systematic Microstructural Changes Peculiar to Fatigue Deformation." ACTA Met., Vol. 11 (July, 1963), 643-653.

(77) Wood, W. A., and W. H. Reinmann. "Some Direct Observations of Cumulative Fatigue Damage in Metals." Office of Naval Research, Air Force Materials Laboratory, Contract No. NONR 266 (91), Technical Report No. 11, Columbia University, October, 1964.

(78) Young, J. M., and A. P. Greenhough. "The Effect of Annealing on Fatigue Damage in Gold." Journal Inst. Met., Vol. 89 (1960-61), 241-246.

(79) Young, C. T., and S. K. Rhee. "Evaluation of Correction Methods for Determining Load in Independent Knoop Microhardness." Journal of Testing and Evaluation, Vol. 6, No. 3 (May, 1978), 221-230.

APPENDIX A

TABLES

TABLE I

CHEMICAL ANALYSIS BY WEIGHT PERCENTAGE OF HUNTINGTON ALLOY NICKEL 200

Chemical	Strip Heat No. N2147A	Bar Heat No. 11E6A
Nickel (plus cobalt)	99.590	99.630
Copper	0.010	0.010
Iron	0.040	0.020
Manganese	0.260	0.240
Carbon	0.040	0.060
Silicon	0.030	0.020
Sulfur	0.005	0.003

TABLE II

RELATIONSHIPS BETWEEN DEFLECTION SETTING, DEFLECTION AT THE NECK, INITIAL STRAIN AT THE NECK AND FORCES REQUIRED TO PRODUCE THE RELATIONSHPS

Item	Setting 5	4	3	2	1
Force (lb)	0.5465	0.9375	1.0625	1.1250	1.1875
Deflection at Neck (in.)	0.0025	0.0079	0.0123	0.0168	0.0211
Strain (μ in./in.)	1300	5375	8480	12,500	16,400

TABLE III

SUMMARY OF MICROHARDNESS DATA FROM THE NICKEL 200 SPECIMENS SUBJECTED TO FULLY REVERSED BENDING AT FIVE DEFLECTION LEVELS

NS = 5 Sets of Curves					NO = 5 Curves Per Set					NP = 9 Points Per Curve			
		No. of Cycles =			.0	.5	1.0	2.0	4.0	8.0	16.0	32.0	64.0
K	*	S	W	*	H1	H2	H3	H4	H5	H6	H7	H8	H9
1	*	1.0	15.0	*	142.0	153.0	159.0	164.0	180.0	192.0	205.0	202.0	211.0
2	*	1.0	50.0	*	126.0	140.0	152.0	156.0	163.0	178.0	188.0	191.0	194.0
3	*	1.0	200.0	*	111.0	123.0	128.0	133.0	137.0	148.0	153.0	156.0	159.0
4	*	1.0	300.0	*	101.0	116.0	121.0	125.0	131.0	144.0	151.0	158.0	159.0
5	*	1.0	500.0	*	97.0	111.0	116.0	124.0	129.0	136.0	145.0	151.0	155.0
6	*	2.0	15.0	*	133.0	143.0	151.0	160.0	167.0	179.0	183.0	196.0	201.0
7	*	2.0	50.0	*	126.0	136.0	141.0	149.0	153.0	158.0	182.0	171.0	171.0
8	*	2.0	200.0	*	113.0	121.0	127.0	133.0	137.0	142.0	148.0	156.0	155.0
9	*	2.0	300.0	*	103.0	114.0	118.0	125.0	129.0	135.0	141.0	147.0	151.0
10	*	2.0	500.0	*	99.0	107.0	113.0	124.0	126.0	131.0	136.0	145.0	144.0
11	*	3.0	15.0	*	130.0	140.0	150.0	160.0	167.0	170.0	178.0	184.0	200.0
12	*	3.0	50.0	*	123.0	132.0	143.0	151.0	155.0	158.0	160.0	172.0	180.0
13	*	3.0	200.0	*	112.0	118.0	127.0	132.0	138.0	140.0	146.0	150.0	151.0
14	*	3.0	300.0	*	96.0	104.0	112.0	118.0	130.0	133.0	138.0	151.0	151.0
15	*	3.0	500.0	*	98.0	105.0	112.0	121.0	126.0	128.0	135.0	147.0	149.0
16	*	4.0	15.0	*	128.0	142.0	147.0	155.0	159.0	164.0	172.0	185.0	208.0
17	*	4.0	50.0	*	125.0	130.0	134.0	137.0	141.0	145.0	151.0	152.0	156.0
18	*	4.0	200.0	*	112.0	117.0	120.0	123.0	126.0	129.0	135.0	137.0	142.0
19	*	4.0	300.0	*	98.0	106.0	110.0	112.0	120.0	124.0	132.0	140.0	146.0
20	*	4.0	500.0	*	95.0	102.0	108.0	110.0	112.0	119.0	126.0	135.0	140.0
21	*	5.0	15.0	*	126.0	133.0	139.0	142.0	145.0	156.0	170.0	174.0	190.0
22	*	5.0	50.0	*	124.0	127.0	126.0	129.0	129.0	133.0	136.0	141.0	149.0
23	*	5.0	200.0	*	112.0	114.0	116.0	119.0	120.0	122.0	123.0	125.0	129.0
24	*	5.0	300.0	*	99.0	105.0	106.0	107.0	108.0	111.0	115.0	118.0	125.0
25	*	5.0	500.0	*	97.0	100.0	103.0	105.0	107.0	109.0	110.0	112.0	119.0

TABLE IV

RMS ERRORS FOR EXPONENTIAL AND LINEAR FIT OF MICROHARDNESS VERSUS NUMBER OF CYCLES (S = 1, W = 200)

K	Cycles	H	HA	HE	Error (%)
Exponential Approximation Curve Fitting Table Case No. 3*					
1	-9.0	111.0	111.5	0.5	0.4
2	-1.0	123.0	117.6	-5.4	-4.4
3	0.0	123.0	120.3	-7.7	-5.0
4	1.0	133.0	123.9	-9.1	-6.8
5	2.0	137.0	129.0	-8.0	-5.8
6	3.0	148.0	136.2	-11.8	-8.0
7	4.0	153.0	146.1	-6.9	-4.5
8	5.0	156.0	160.0	4.0	2.6
9	6.0	159.0	179.4	20.4	12.8
Linear Approximation Curve Fitting Table Case No. 3†					
1	-9.0	111.0	130.4	18.4	17.5
2	-1.0	123.0	130.7	7.7	6.3
3	0.0	128.0	131.0	3.0	2.4
4	1.0	133.0	131.6	-1.4	-1.1
5	2.0	137.0	132.8	-4.2	-3.1
6	3.0	148.0	135.1	-12.9	-8.7
7	4.0	153.0	139.7	-13.3	-8.7
8	5.0	156.0	149.0	-7.0	-4.5
9	6.0	159.0	167.6	8.6	5.4

*S = 1.0, Load = 200.0, A = 0.48, B = 9.3, RMSERR = 9.7 = 6.6%.

†S = 1.0, Load = 200.0, A = 0.58, B = 130.4, RMSERR = 10.2 = 7.9%.

TABLE V

RMS ERRORS FOR EXPONENTIAL AND LINEAR FIT OF MICROHARDNESS VERSUS INDENTOR WEIGHT (S = 1, N = 16)

K	Weight	H	HA	HE	Error (%)
Exponential Approximation Curve Fitting Table Case No. 7*					
1	15.00	205.0	207.3	2.3	1.1
2	50.0	188.0	182.6	-5.4	-2.9
3	200.0	153.0	157.7	4.7	3.1
4	300.0	151.0	151.1	0.1	0.1
5	500.0	145.0	143.2	-1.8	-1.3
Linear Approximation Curve Fitting Table Case No. 7†					
1	15.0	205.0	191.9	-13.1	-6.4
2	50.0	188.0	187.7	-0.3	-0.2
3	200.0	153.0	169.9	16.9	11.1
4	300.0	151.0	158.1	7.1	4.7
5	500.0	145.0	134.4	-10.6	-7.3

*S = 1.0, Cyc = 16.0, P = -0.11, Q = 276.0, RMSERR = 3.5 = 2.0%.

†S = 1.0, Cyc = 16.0, P = -0.12, Q = 193.6, RMSERR = 11.2 = 6.9%.

TABLE VI

DEVELOPMENT OF SLIP BANDS WITH PROGRESS OF CYCLING

Cell \ N	1/2		1		2		4		8		16		32		64		128	
	N	T	N	T	N	T	N	T	N	T	N	T	N	T	N	T	N	T
1	7	7	6	13	12	25	15	40	10	50	20	70	20	90	20	110	20	130
2	11	11	13	24	18	42	20	62	20	83	20	92	20	112	10	122	10	132
3	12	12	24	36	5	41	9	50	5	55	10	65	20	85	10	95	10	105
4	13	13	15	28	27	55	16	71	11	82	12	94	7	101	9	110	5	115
5	11	11	12	23	21	44	18	62	9	71	12	83	6	89	9	97	10	107
6	15	15	15	30	17	57	12	69	9	78	20	98	17	115	12	127	10	137
Avg	11	11	14	26	17	44	15	59	11	70	16	84	15	99	12	118	11	121

Note: N = New, T = Total, Avg = Average.

TABLE VII

EXPONENTIAL APPROXIMATION FOR COEFFICIENTS A_x AND B_x, AND RMS ERROR

		AX (S,W)							BX (S,W)				
Load	S	1.00	2.00	3.00	4.00	5.00	Load	S	1.00	2.00	3.00	4.00	5.00
Exponential Fit Equation: H = HO + BX*N**AX													
15	*	.58	.52	.48	.50	.49	15	*	9.52	11.69	9.26	10.49	10.39
50	*	.57	.49	.50	.49	.51	50	*	9.48	8.60	7.68	8.69	8.11
200	*	.54	.51	.50	.56	.55	200	*	9.87	9.30	7.32	8.38	7.65
300	*	.53	.50	.49	.54	.52	300	*	10.04	5.35	5.00	6.80	6.53
500	*	.60	.57	.48	.43	.46	500	*	6.69	2.39	2.90	4.48	3.70
		RMSERX (S,W)							RMS%EX(S,W)				
Load	S	1.00	2.00	3.00	4.00	5.00	Load	S	1.00	2.00	3.00	4.00	5.00
Exponential Fit Equation: H = HO + BX*N**AX													
15	*	16.81	15.96	9.74	11.59	11.09	15	*	8.42	8.90	6.59	8.02	8.01
50	*	14.00	9.16	8.68	8.52	10.35	50	*	7.55	5.72	5.94	6.20	7.69
200	*	12.45	10.46	9.38	12.45	10.05	200	*	7.06	6.50	6.55	8.91	7.37
300	*	8.00	5.41	4.07	6.61	5.65	300	*	4.92	3.62	3.03	4.99	4.50
500	*	7.85	0.82	2.16	1.58	2.28	500	*	4.57	0.63	1.74	1.47	2.09

TABLE VIII

LINEAR APPROXIMATION FOR COEFFCIENTS A_L AND B_L, AND RMS ERROR

		AL (S,W)							BL (S,W)				
Load	S	1.00	2.00	3.00	4.00	5.00	Load	S	1.00	2.00	3.00	4.00	5.00
Linear Fit Equation: H = BL + AL*N													
15	*	0.90	0.84	0.58	0.73	0.71	15	*	165.92	153.45	130.44	123.66	119.23
50	*	0.90	0.55	0.54	0.59	0.56	50	*	155.43	144.04	129.28	120.81	117.01
200	*	0.86	0.69	0.47	0.72	0.67	200	*	152.12	142.92	128.21	115.67	115.05
300	*	1.03	0.40	0.39	0.65	0.61	300	*	147.58	135.58	121.24	111.66	107.64
500	*	0.90	0.37	0.22	0.34	0.27	500	*	140.04	127.49	116.93	105.69	103.03
		RMSERL (S,W)							RMS%EL (S,W)				
Load	S	1.00	2.00	3.00	4.00	5.00	Load	S	1.00	2.00	3.00	4.00	5.00
Linear Fit Equation: H = BL + AL*N													
15	*	15.32	15.06	10.10	12.09	11.30	15	*	8.90	9.97	7.91	9.88	9.85
50	*	12.88	9.42	8.97	9.06	10.01	50	*	8.24	6.64	6.94	7.67	8.72
200	*	11.37	9.90	8.91	11.55	9.63	200	*	7.76	7.26	7.09	10.01	8.42
300	*	8.73	6.00	5.00	7.61	6.85	300	*	6.20	4.37	4.08	6.65	6.21
500	*	8.58	2.04	2.68	2.91	2.99	500	*	5.76	1.55	2.30	2.78	2.93

TABLE IX

EXPONENTIAL APPROXIMATION FOR COEFFICIENTS P_x AND Q_x, AND RMS ERROR

		PX (S,W)						QX (S,W)				
Cyc	S	1.00	2.00	3.00	4.00	5.00	Cyc S	1.00	2.00	3.00	4.00	5.00
Exponential Fit Equation: H = QX*W**PX												
0	*	-0.11	-0.09	-0.10	-0.09	-0.10	0 *	192.37	198.75	211.87	212.58	238.66
1	*	-0.10	-0.11	-0.09	-0.10	-0.09	1 *	257.68	275.97	261.71	275.31	171.83
1	*	-0.08	-0.08	-0.08	-0.08	-0.09	1 *	182.88	192.09	198.93	209.95	226.24
2	*	-0.08	-0.09	-0.09	-0.09	-0.09	2 *	227.36	244.42	252.12	168.93	182.14
4	*	-0.09	-0.09	-0.08	-0.08	-0.08	4 *	196.77	208.19	211.13	215.11	219.82
16	*	-0.10	-0.10	-0.09	-0.09	-0.09	16 *	202.93	206.57	208.67	215.40	224.26
32	*	-0.10	-0.08	-0.08	-0.09	-0.09	32 *	257.93	162.00	170.38	175.92	180.89
64	*	-0.09	-0.10	-0.12	-0.12	-0.13	64 *	183.25	202.56	227.57	235.78	260.35
		RMSERX (S,W)						RMS%EX (S,W)				
Cyc	S	1.00	2.00	3.00	4.00	5.00	Cyc *	1.00	2.00	3.00	4.00	5.00
Exponential Fit Equation: H = QX*W**PX												
0	*	1.82	1.36	3.58	3.32	2.23	0 *	1.66	1.02	2.36	2.25	1.57
1	*	2.93	3.48	4.55	4.00	2.99	1 *	1.65	2.03	2.62	2.39	2.56
1	*	2.76	2.31	1.82	1.29	1.20	1 *	2.16	1.77	1.36	0.95	0.80
2	*	1.43	2.42	3.12	4.38	3.80	2 *	0.89	1.48	1.76	4.10	3.29
4	*	4.39	4.16	1.69	1.59	1.29	4 *	3.44	3.20	1.15	1.03	0.89
8	*	2.41	3.51	4.83	2.56	1.97	8 *	1.58	2.31	4.22	2.19	1.68
16	*	2.01	1.21	0.70	1.43	5.79	16 *	1.72	1.00	0.48	0.94	3.73
32		10.05	4.49	3.01	2.08	2.64	32 *	6.01	3.93	2.54	1.83	2.29
64	*	2.62	2.68	3.97	3.24	4.85	64 *	2.27	2.15	2.78	2.18	3.08

TABLE X

LINEAR APPROXIMATION FOR COEFFICIENTS P_L AND Q_L, AND RMS ERROR

		P_L (S,W)						Q_L (S,W)				
Cyc	S	1.00	2.00	3.00	4.00	5.00	Cyc	1.00	2.00	3.00	4.00	5.00
Linear Fit Equation: $H = Q_L + P_L*W$												
0	*	-0.09	-0.08	-0.09	-0.08	-0.10	0 *	133.81	146.04	154.47	158.39	169.28
1	*	-0.11	-0.12	-0.10	-0.11	-0.07	1 *	183.37	193.64	193.56	199.03	129.79
1	*	-0.07	-0.08	-0.07	-0.08	-0.09	1 *	139.82	146.17	153.55	159.35	167.72
2	*	-0.09	-0.09	-0.10	-0.07	-0.07	2 *	172.13	182.55	185.20	126.51	135.63
4	*	-0.08	-0.08	-0.08	-0.08	-0.08	4 *	146.25	154.19	160.49	163.46	168.44
8	*	-0.07	-0.10	-0.07	-0.08	-0.08	8 *	175.96	186.70	127.16	136.25	140.12
16	*	-0.09	-0.09	-0.08	-0.08	-0.08	16 *	145.58	150.07	153.75	160.66	166.56
32	*	-0.10	-0.07	-0.07	-0.07	-0.07	32 *	179.68	125.49	130.40	132.74	135.77
64	*	-0.07	-0.08	-0.10	-0.11	-0.12	64 *	137.09	144.25	152.46	156.75	167.76
		RMSERL (S,W)						RMS%EL (S,W)				
Cyc	S	1.00	2.00	3.00	4.00	5.00	Cyc	1.00	2.00	3.00	4.00	5.00
Linear Fit Equation: $H = Q_L + P_L*W$												
0	*	6.65	6.00	6.24	7.06	9.64	0 *	5.78	4.70	4.89	5.32	6.69
1	*	8.74	11.16	9.96	11.67	3.93	1 *	5.69	6.92	6.14	6.93	3.64
1	*	3.61	4.59	6.09	6.46	8.32	1 *	3.00	3.61	4.51	4.56	5.41
2	*	7.81	9.69	10.78	5.53	5.79	2 *	4.86	5.73	6.16	5.56	5.29
4	*	5.87	7.46	5.93	5.95	7.23	4 *	5.04	5.94	4.21	4.13	4.67
8	*	7.45	11.37	3.95	5.21	6.03	8 *	4.73	6.98	3.99	4.48	4.97
16	*	7.45	6.58	7.60	8.14	12.31	16 *	5.83	4.79	5.41	5.45	7.76
32	*	18.28	3.75	3.43	5.13	5.44	32 *	10.63	3.76	3.14	4.35	4.61
64	*	6.31	8.47	11.79	11.76	15.04	64 *	5.18	6.46	8.31	8.16	9.81

APPENDIX B

FIGURES

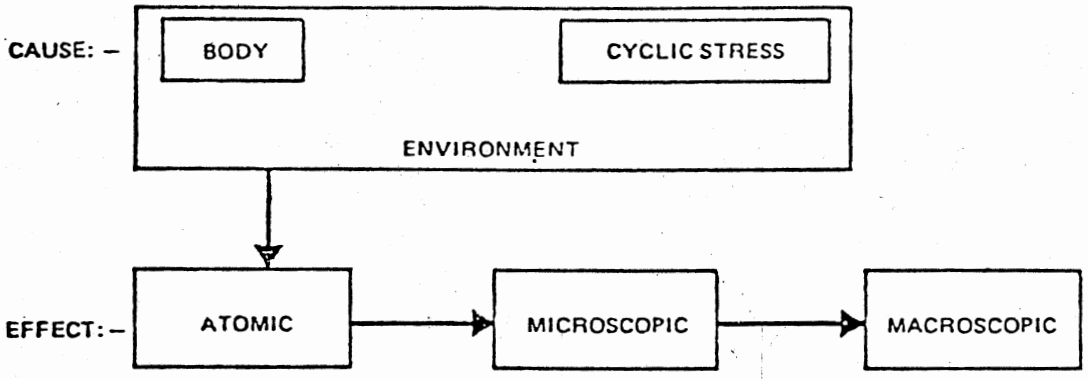

1. DISLOCATION MOVEMENTS
2. DISLOCATION MULTIPLICATIONS
3. DEFECT INTERACTIONS
4. CROSS SLIP

1. SLIP FORMATION
2. SLIP SATURATION
3. STRUCTURE DETERIORATION
4. CRACK NUCLEATION AND PROPAGATION

1. PLASTIC STRAIN AND ENERGY CHANGES
2. CRACK PROPAGATION
   - 2.1 STABLE STAGE
   - 2.2 UNSTABLE STAGES
   - 2.3 CRITICAL LENGTH
   - 2.4 FINAL FRACTURE

Figure 1. Fatigue Causes and Effects

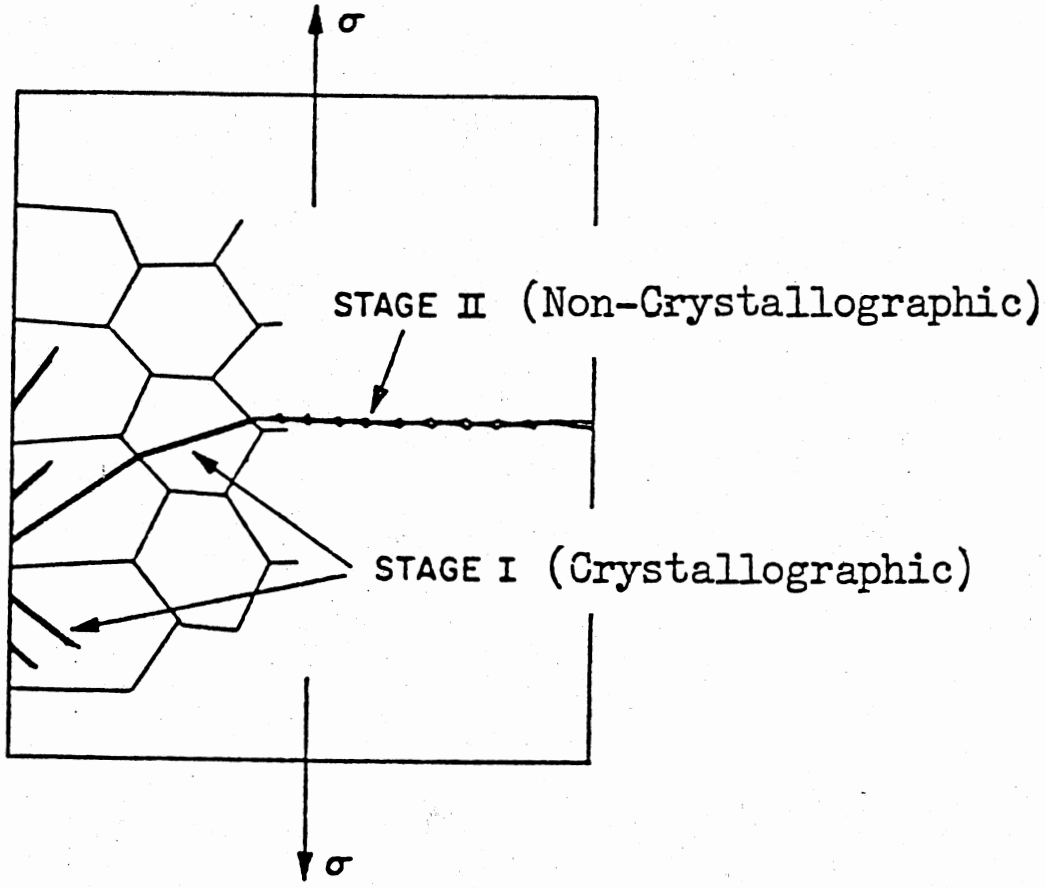

Figure 2. Different Stages of Crack Growth (After Forsyth (16))

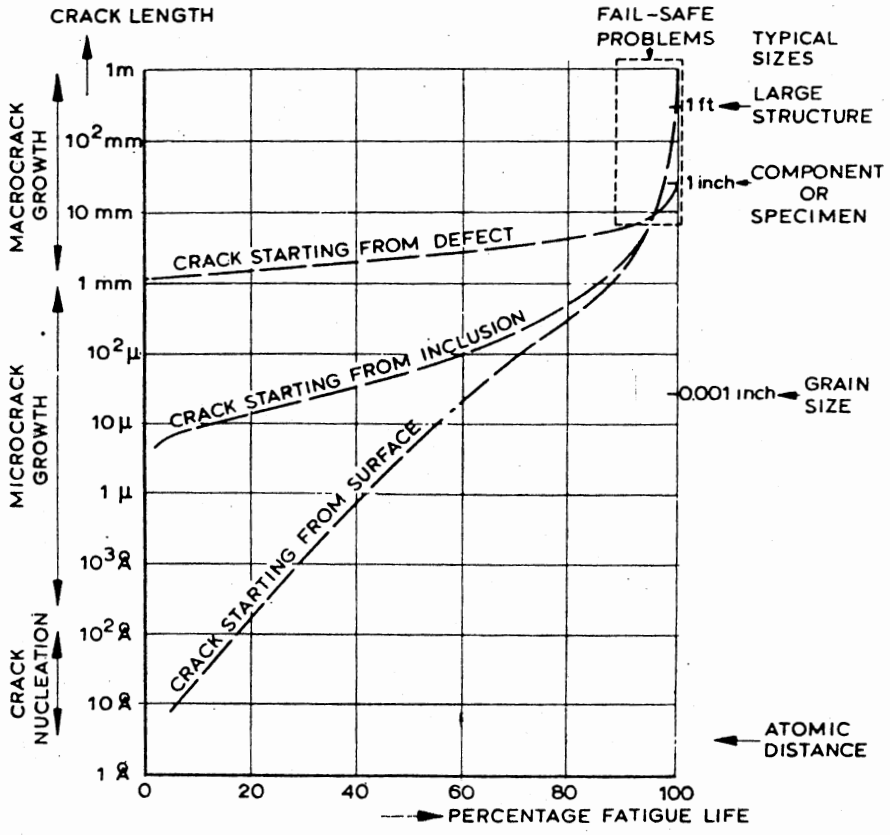

Figure 3. Schematic Diagram of Crack Growth Curves, Indicating Range of Values for Crack Length (After Feltner and Beardmore (15))

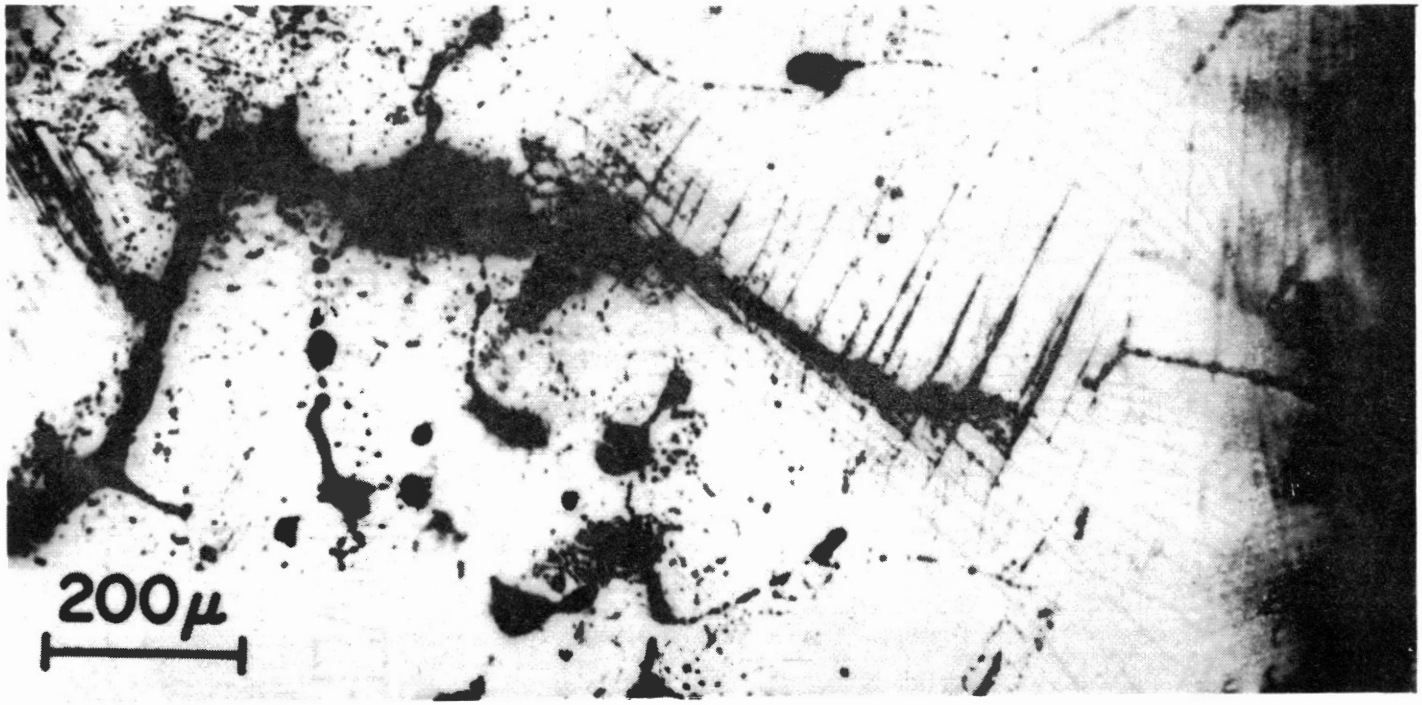

Figure 4. Fatigue Crack Initiated at a Gas Pore in a Nickel Alloy
(After Feltner and Beardmore (15))

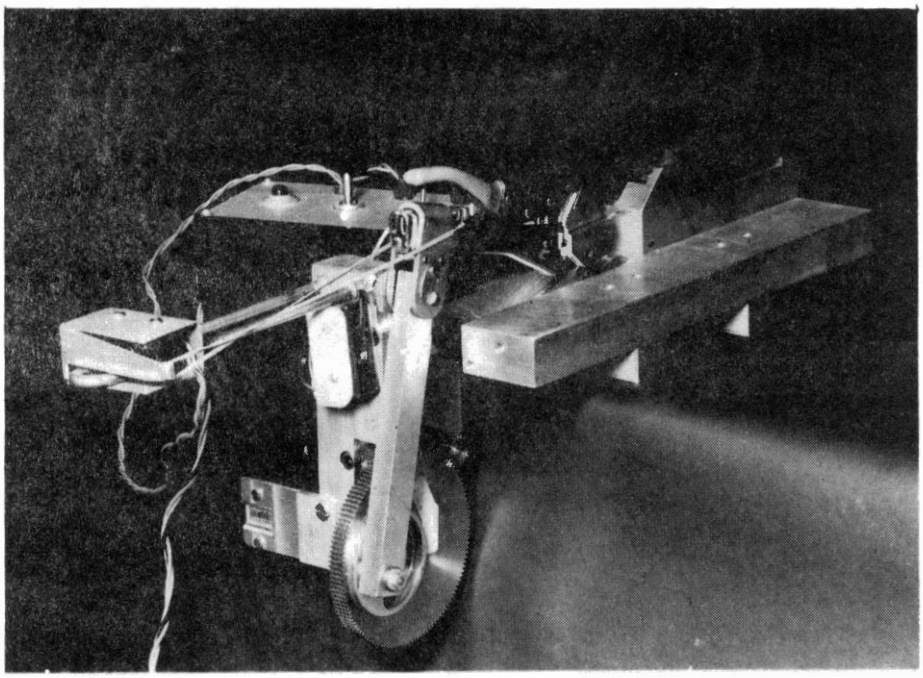

Figure 5. Machine for Testing Specimens in Fully Reversed Bending

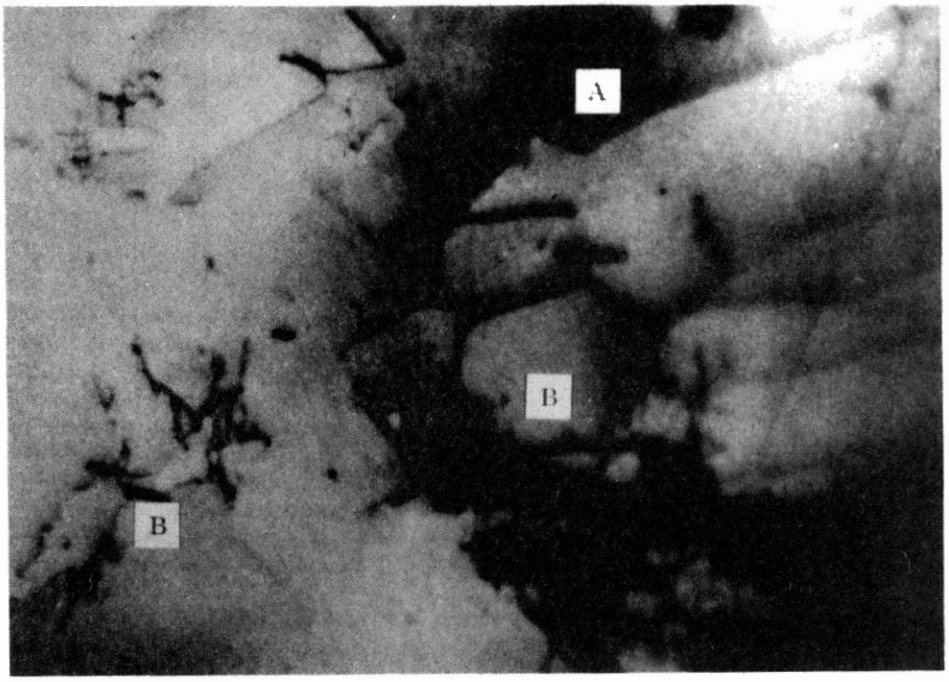

Figure 6. Substructure Arrangements in Pure Nickel. Note Stacking Fault at A and Tangles at B's (Courtesy of Robert Herfert)

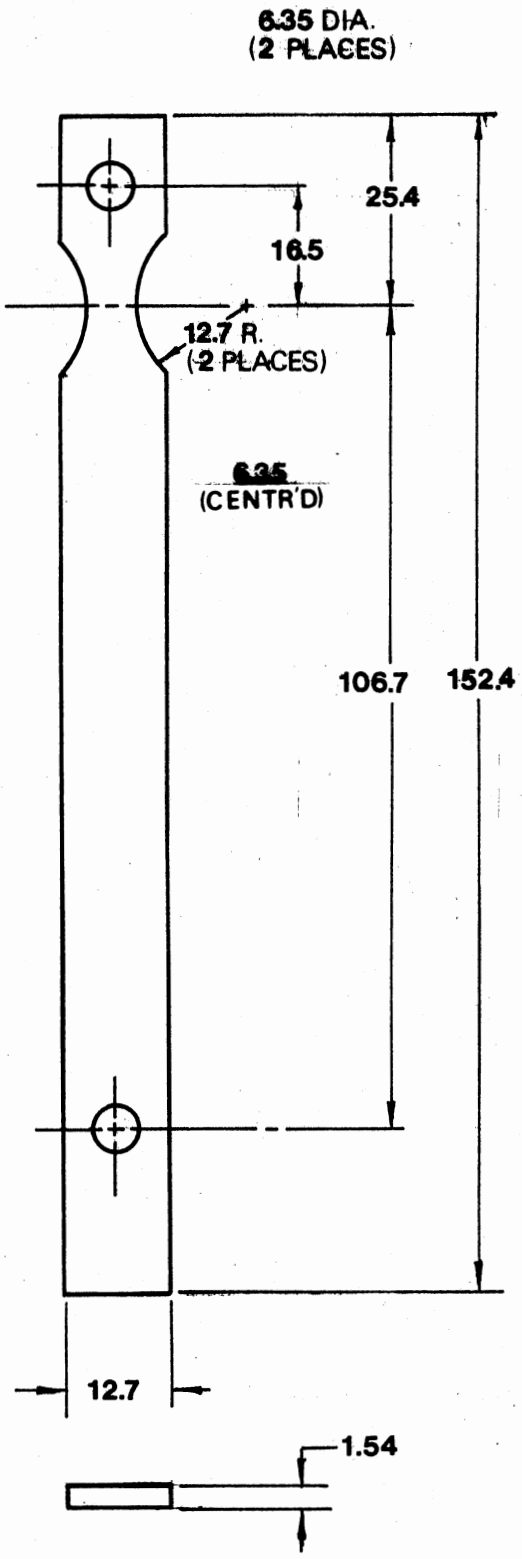

Figure 7. Configuration Utilized in Preliminary Studies (All Dimensions in mm)

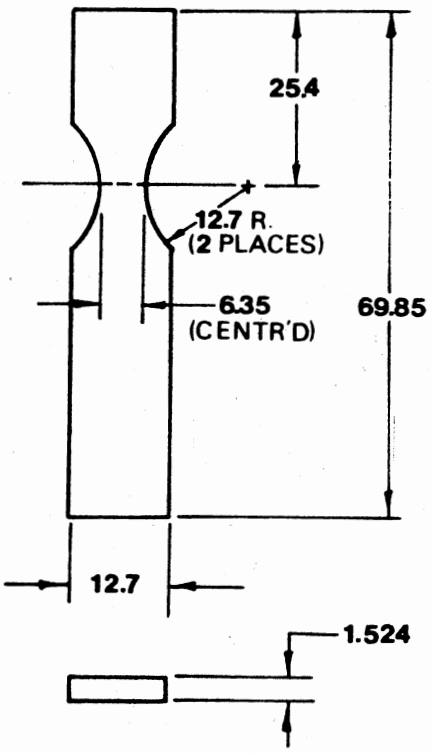

Figure 8. Sample Geometry of the Finalized Test Specimen Used in This Study (All Dimensions in mm)

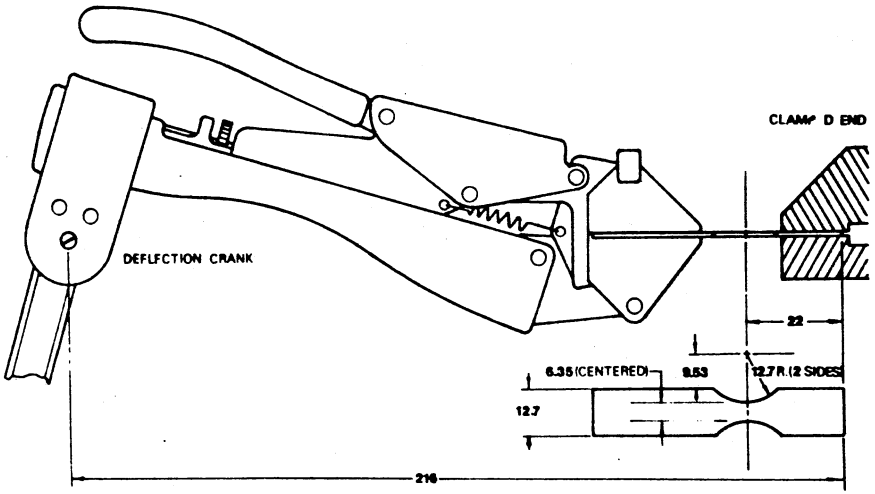

Figure 9. Sample Geometry of Finalized Test Specimen With Schematic of Its Mounting in Bending Machine (All Dimensions in mm)

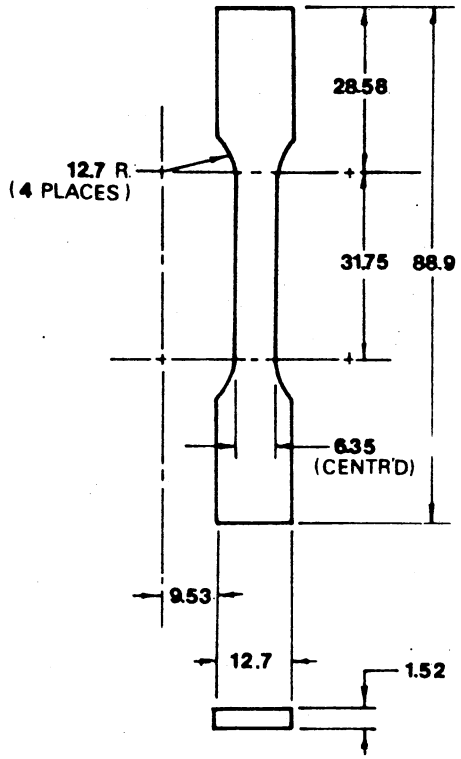

Figure 10. Details of the Nickel 200 Specimen Used in Testing of Monotonic Properties (All Dimensions in mm)

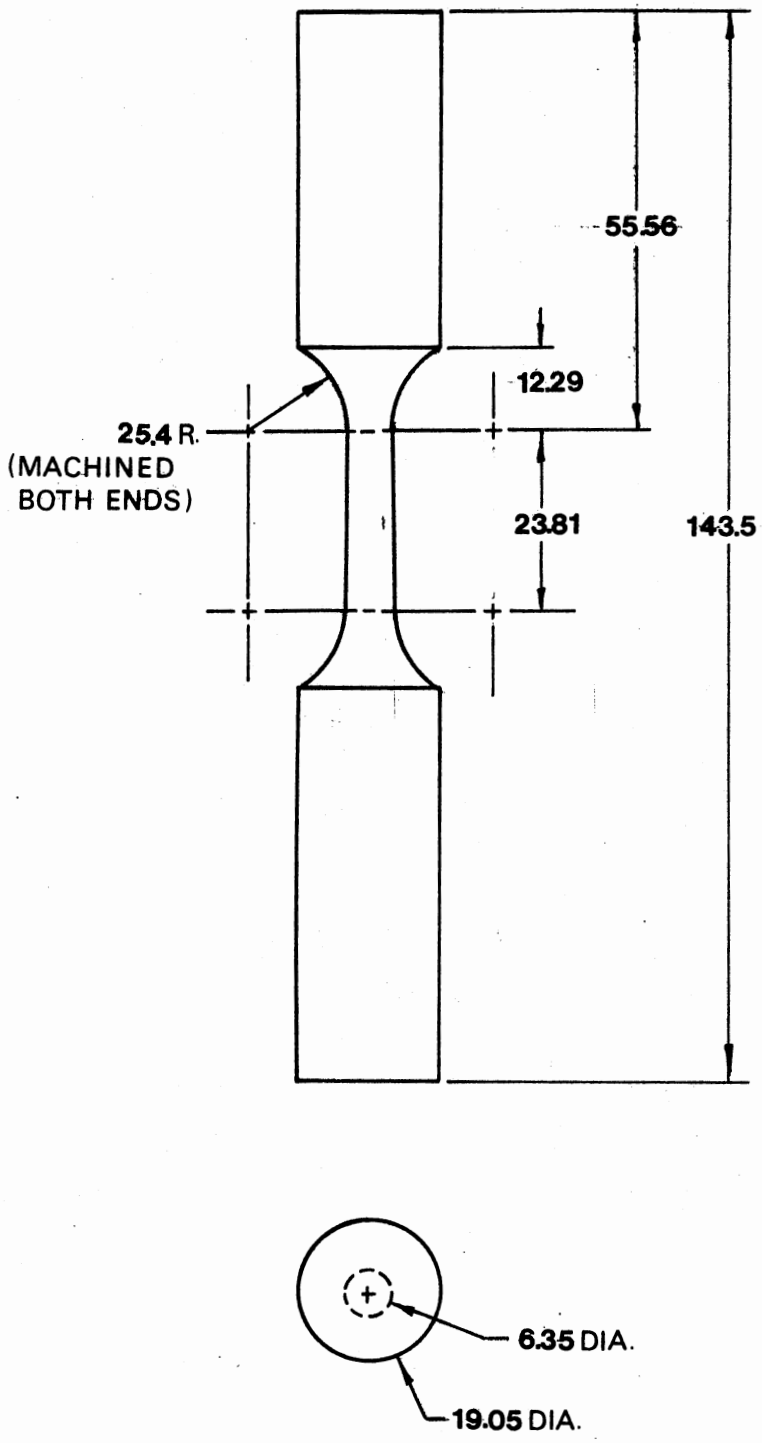

Figure 11. Details of the Nickel 200 Specimen Used to Determine Cyclic Properties (All Dimensions in mm)

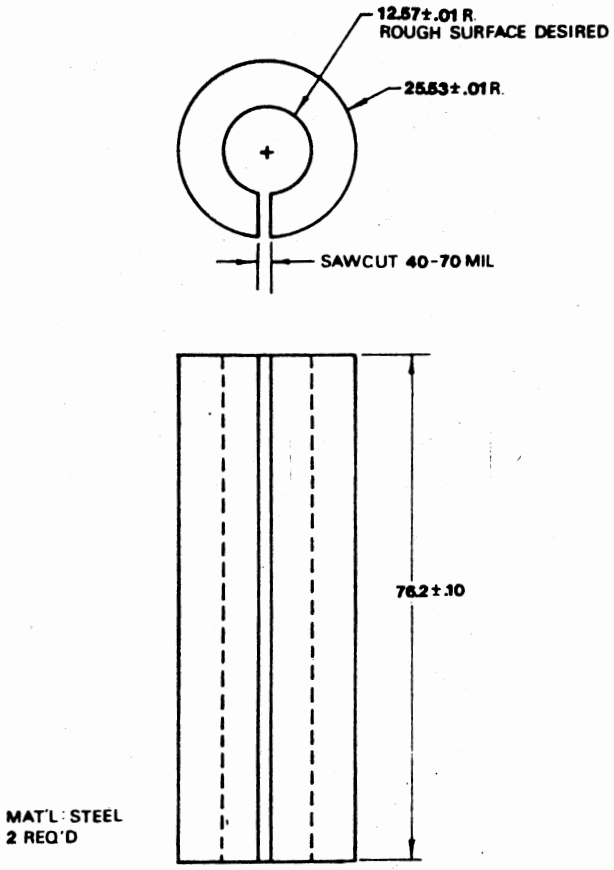

Figure 12. Details of the Holding Grip for the Cyclic Test Specimens (All Dimensions in mm)

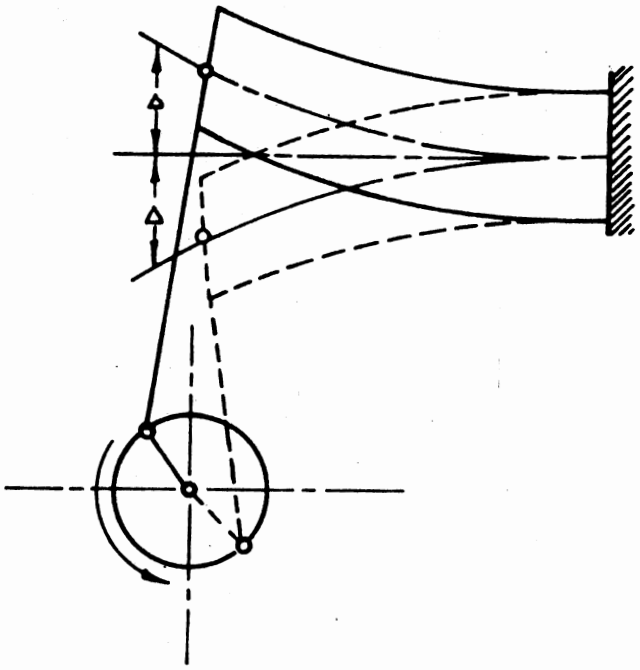

Figure 13. Schematic Representation of the Operation of Bending Machine for Testing of the Nickel 200 Specimen in Fully Reverted Bending

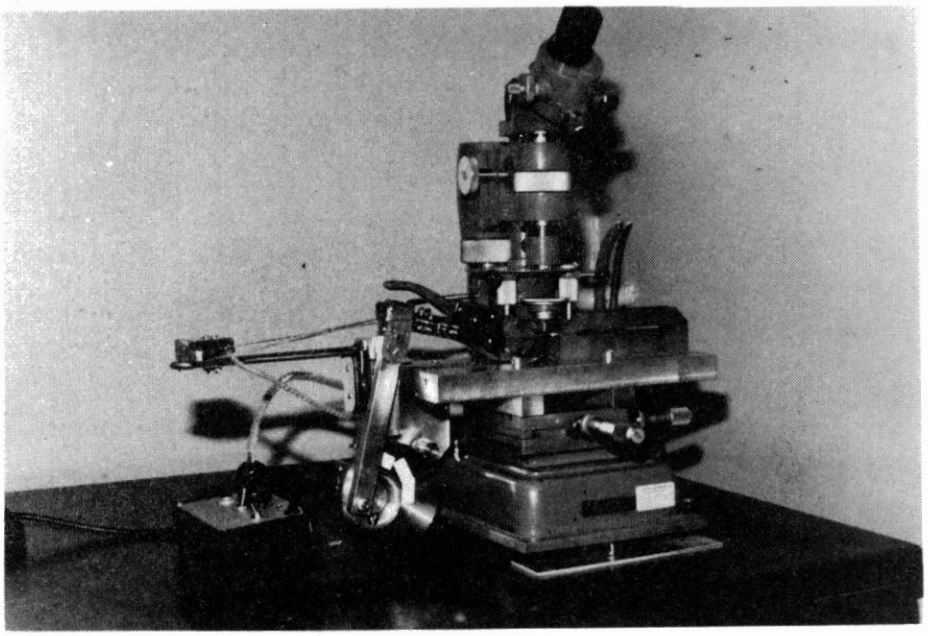

Figure 14. Machine for Testing Specimens in Fully Reversed Bending Mounted on the Stage of the Leitz Microhardness Tester in the Position of an Indentation Being Made

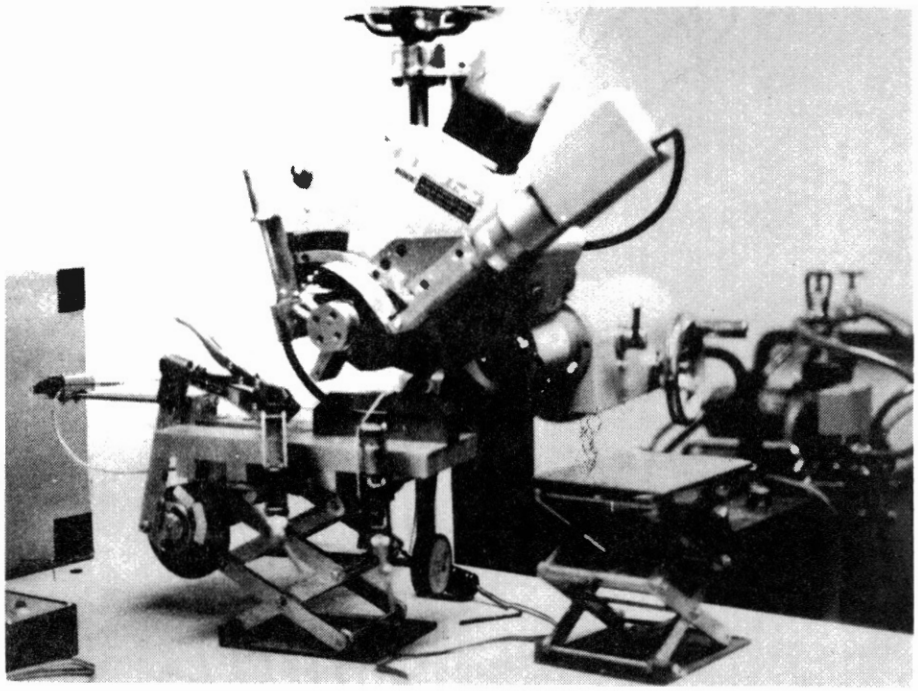

Figure 15. Bending Machine Situated Under the General Electric X-Ray Diffraction Goniometer

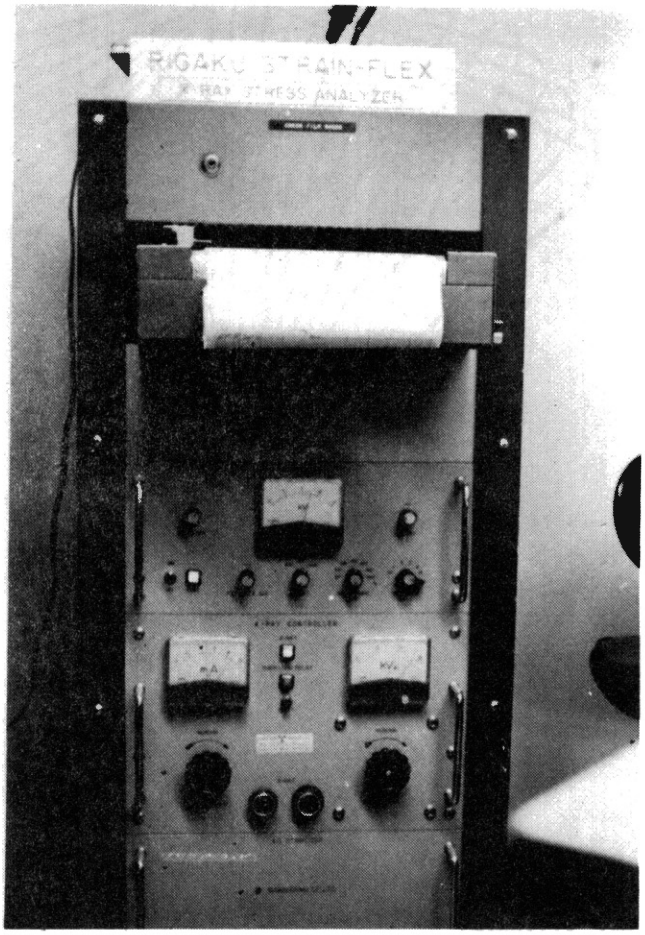

Figure 16. Rigaku Strain-Flex X-Ray Diffraction Stress Analyzer

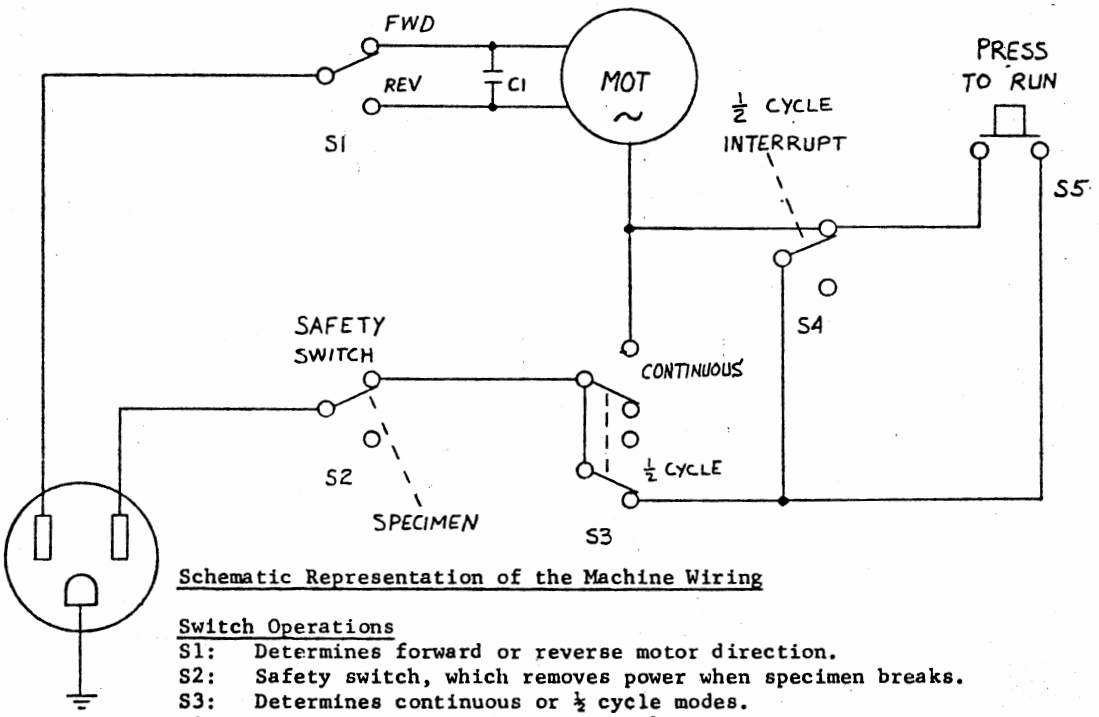

Schematic Representation of the Machine Wiring

Switch Operations

S1: Determines forward or reverse motor direction.
S2: Safety switch, which removes power when specimen breaks.
S3: Determines continuous or ½ cycle modes.
S4: Micro-switch which allows only ½ cycle motor movement.
S5: Used when continuous operation is desired during ½ cycle mode.

Figure 17. Wiring and Switching Schematic of the Bending Machine

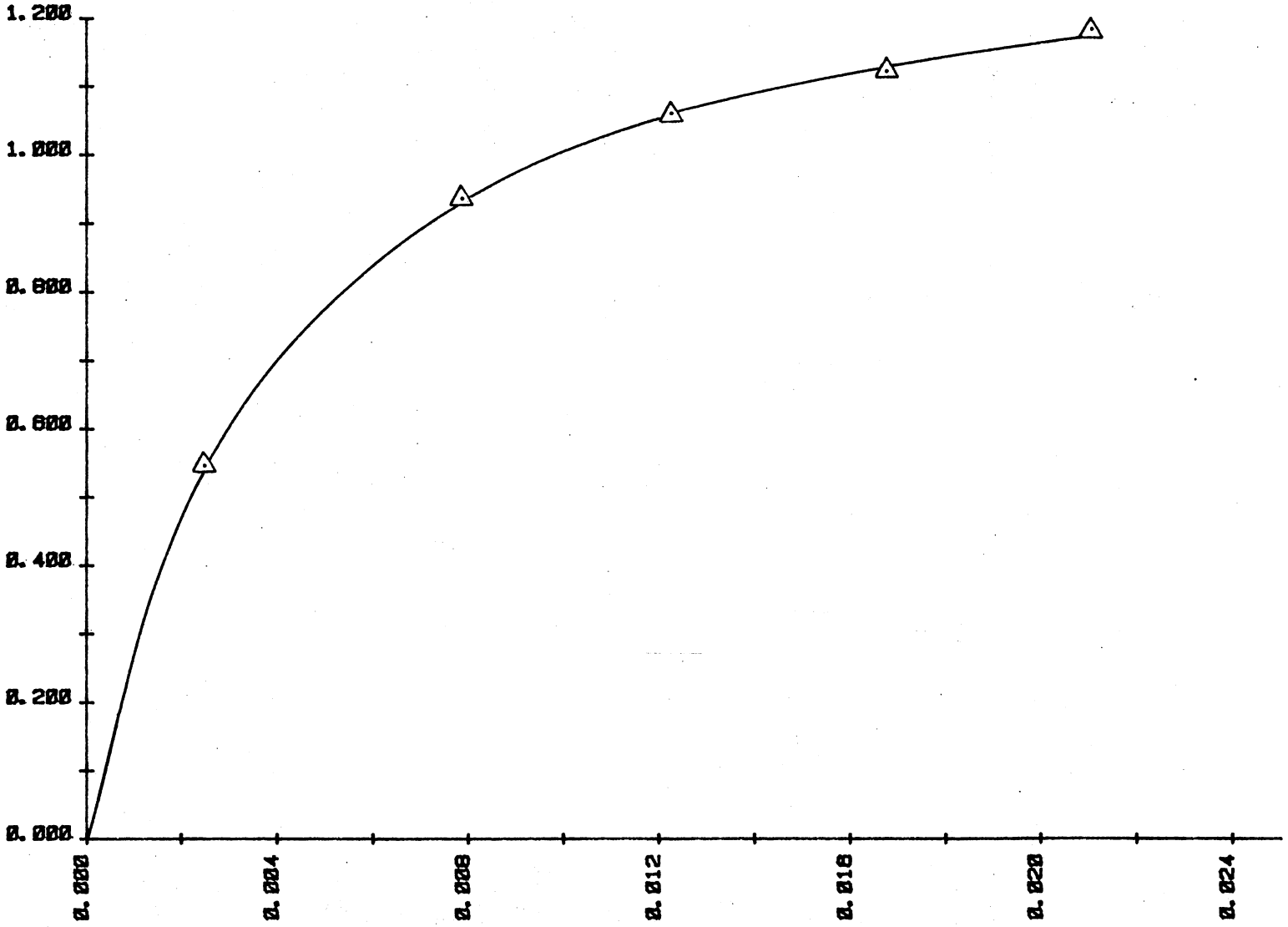

Figure 18. Graph of Force at the End of Clamp Versus Deflection at the Neck of Specimen

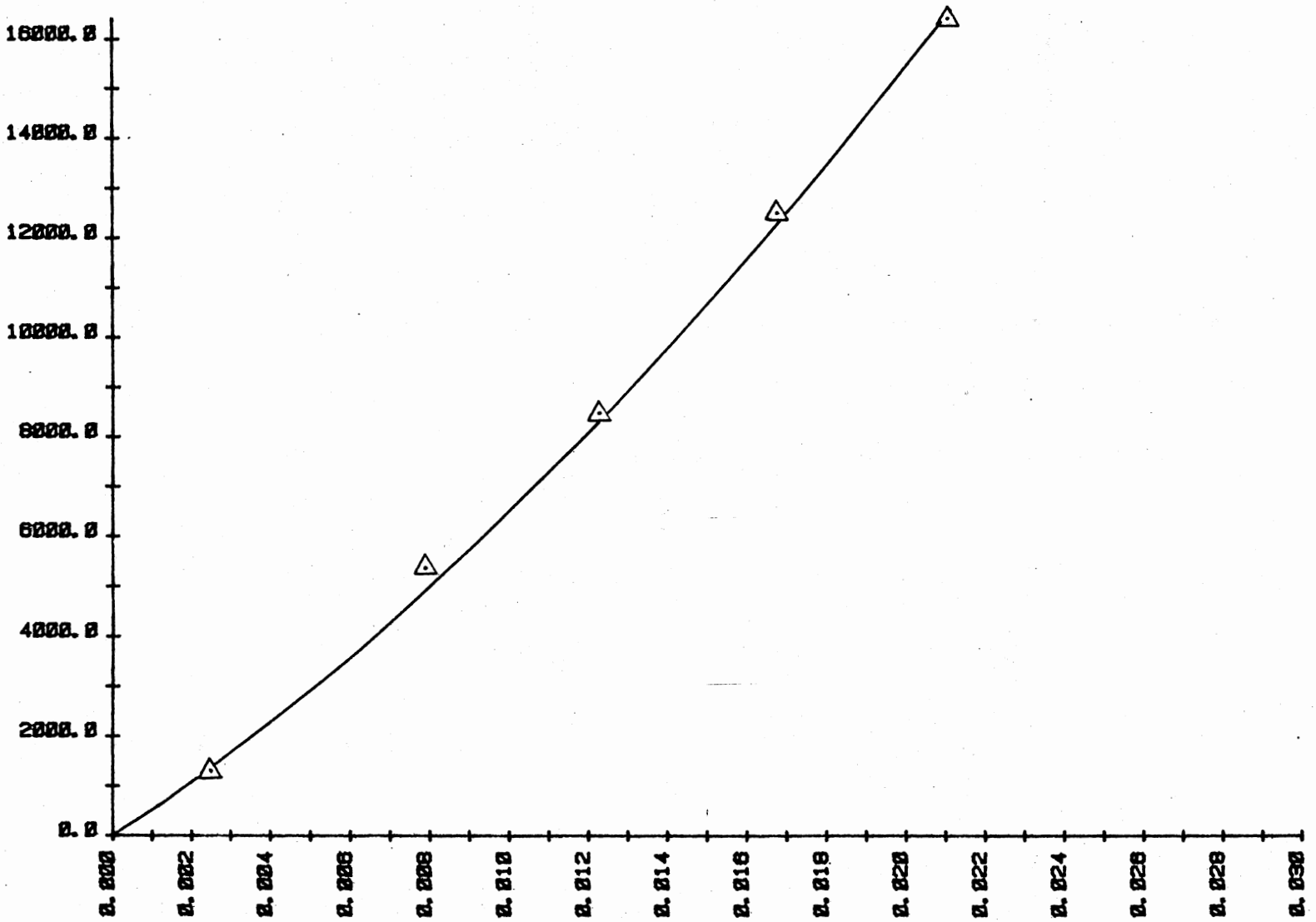

Figure 19. Graph of the Strain Versus Deflection at the Neck of the Specimen

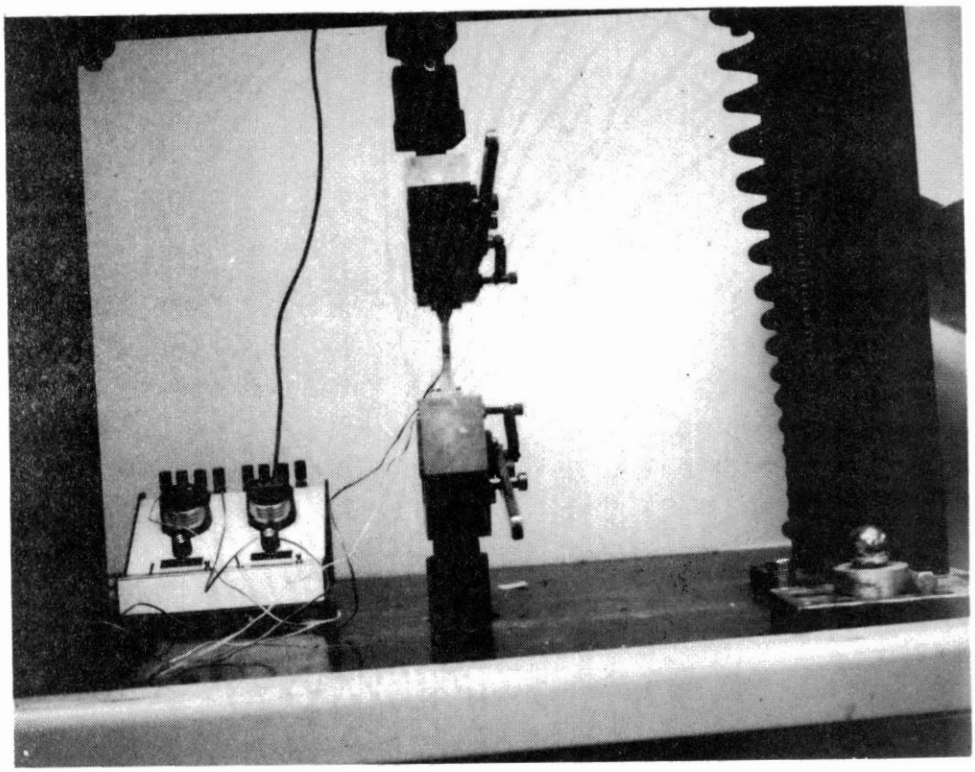

Figure 20. Nickel 200 Monotonic Specimen Installed in Instron Testing Machine

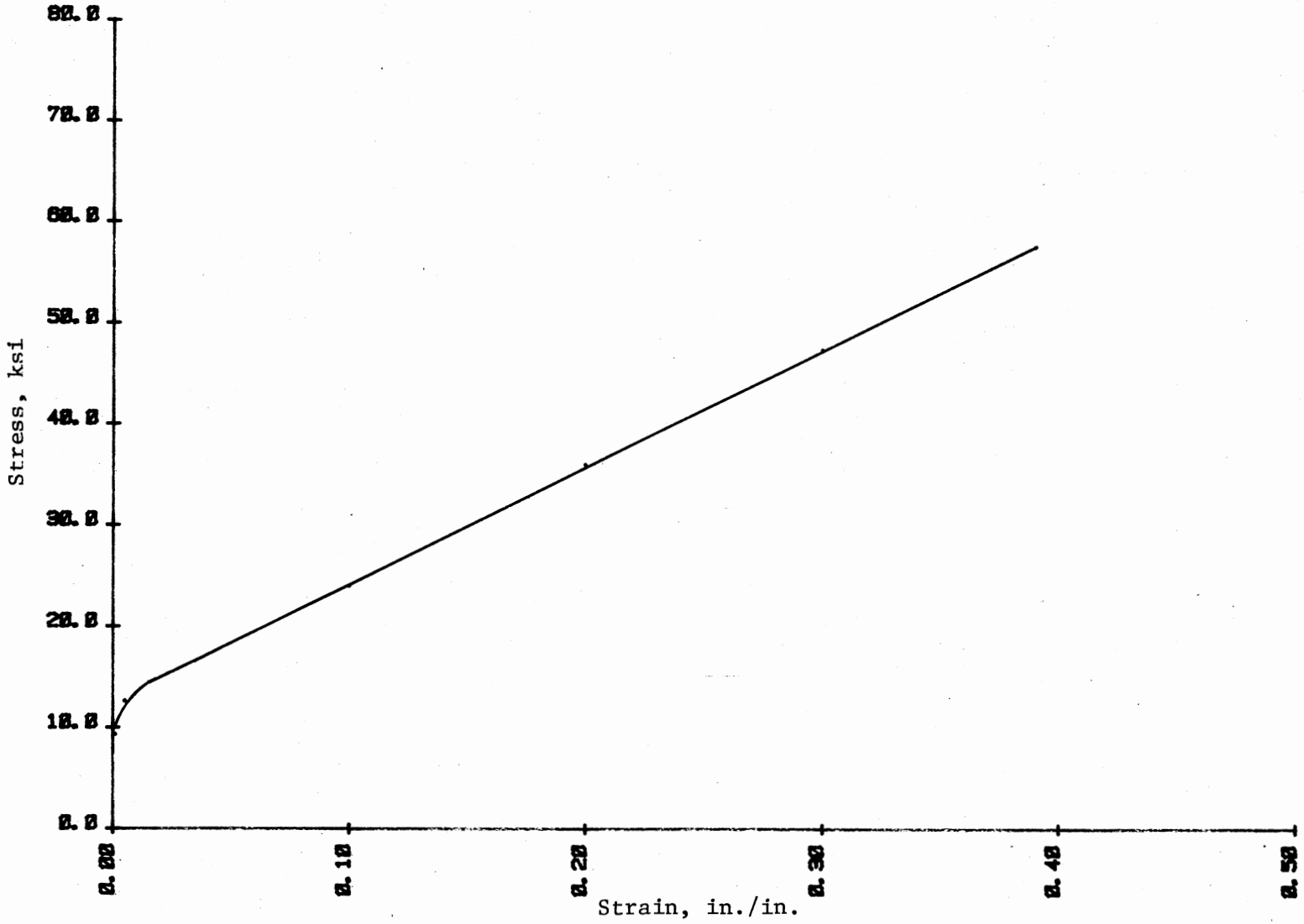

Figure 21. Monotonic Stress Versus Strain Graph for the Nickel 200 Material in Fully Annealed Condition

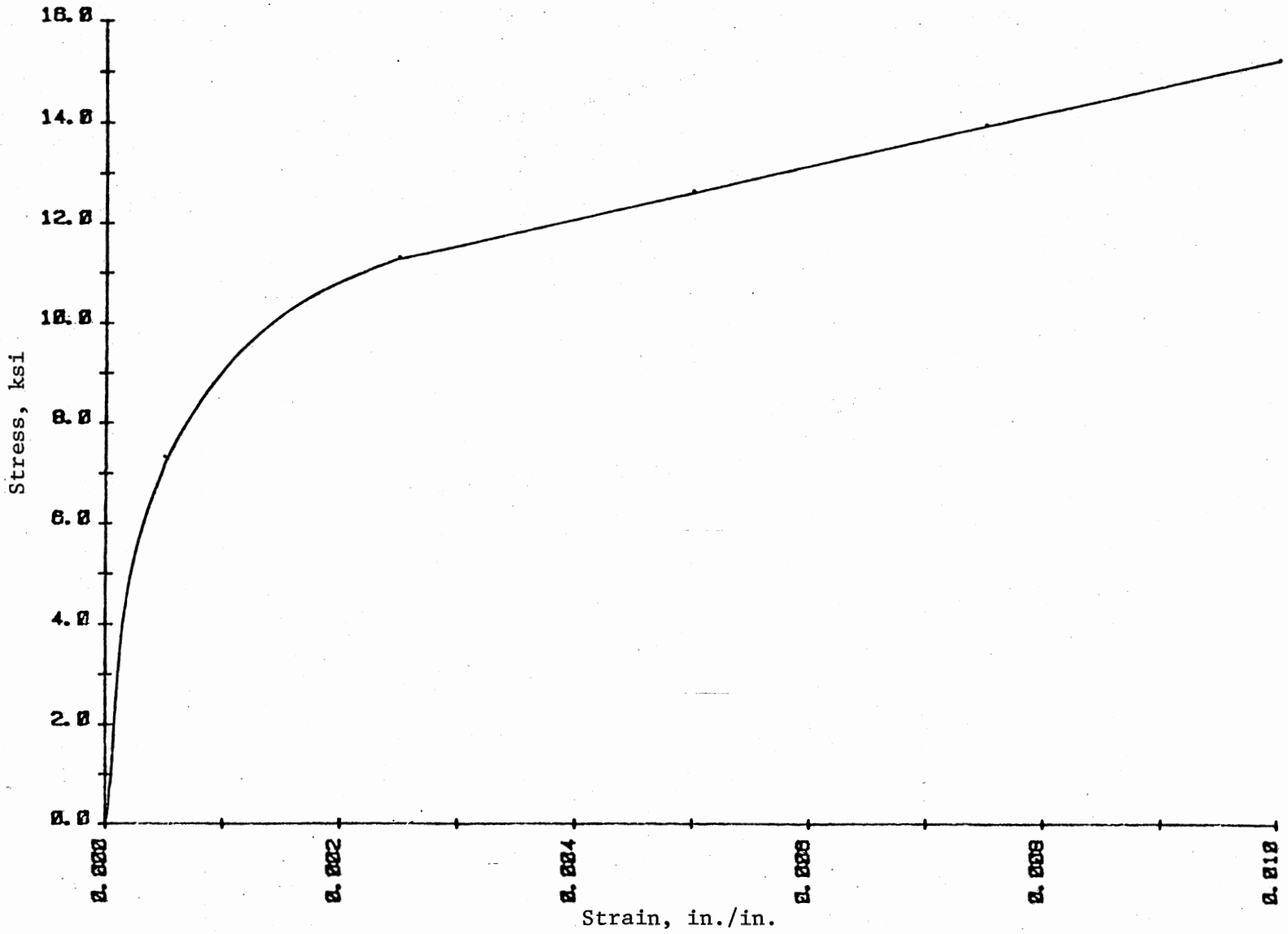

Figure 22. Monotonic Stress Versus Strain Graph for the Nickel 200 Material in Fully Annealed Condition

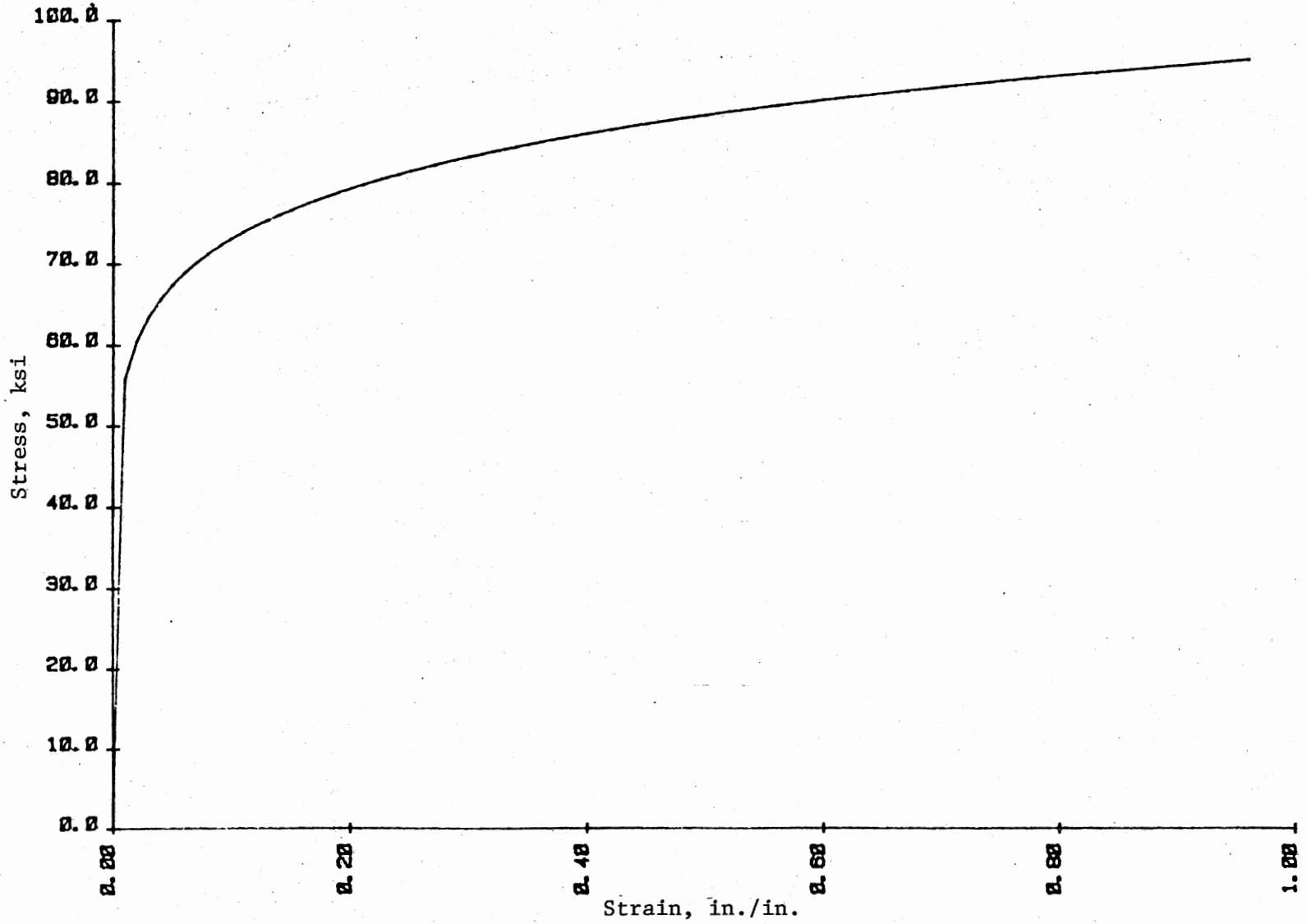

Figure 23. Cyclic Stress Versus Strain Graph for the Nickel 200 Material in Annealed Condition

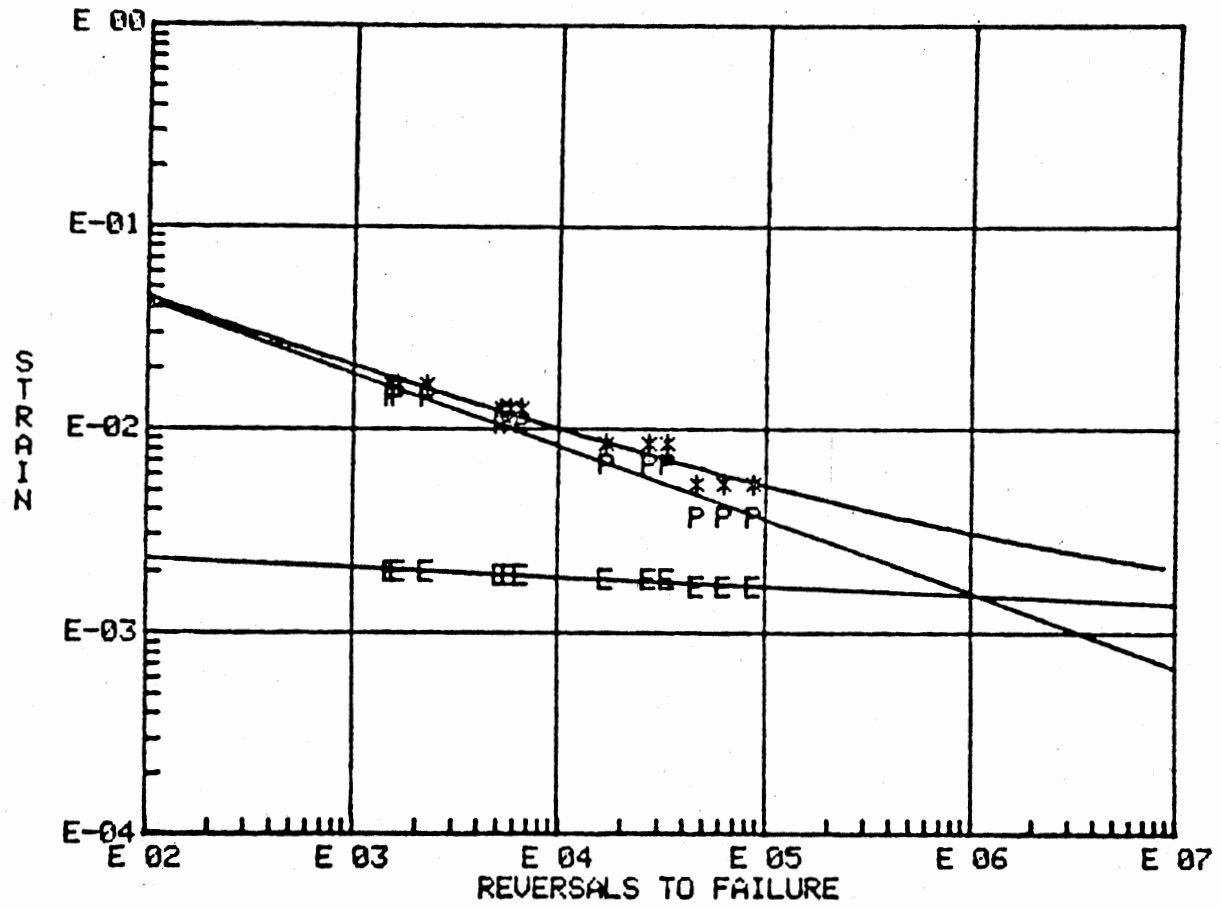

E = Elastic Strain, P = Plastic Strain, * = Total Strain

Figure 24. Manson-Coffin Strain Life Curve

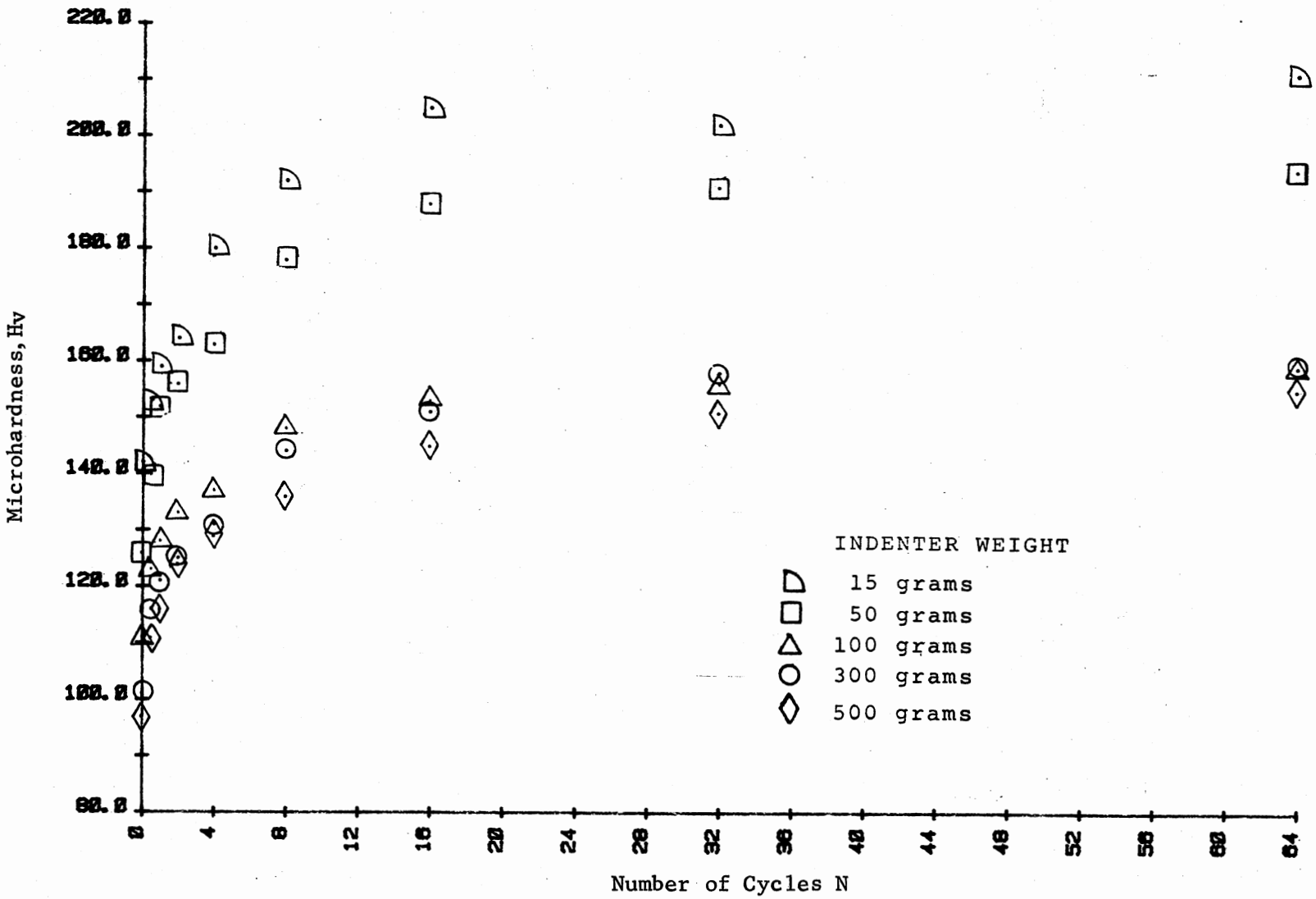

Figure 25. Microhardness H_V Versus Number of Cycles N Curve (Deflection Setting No. 1, 5 Indenter Weights)

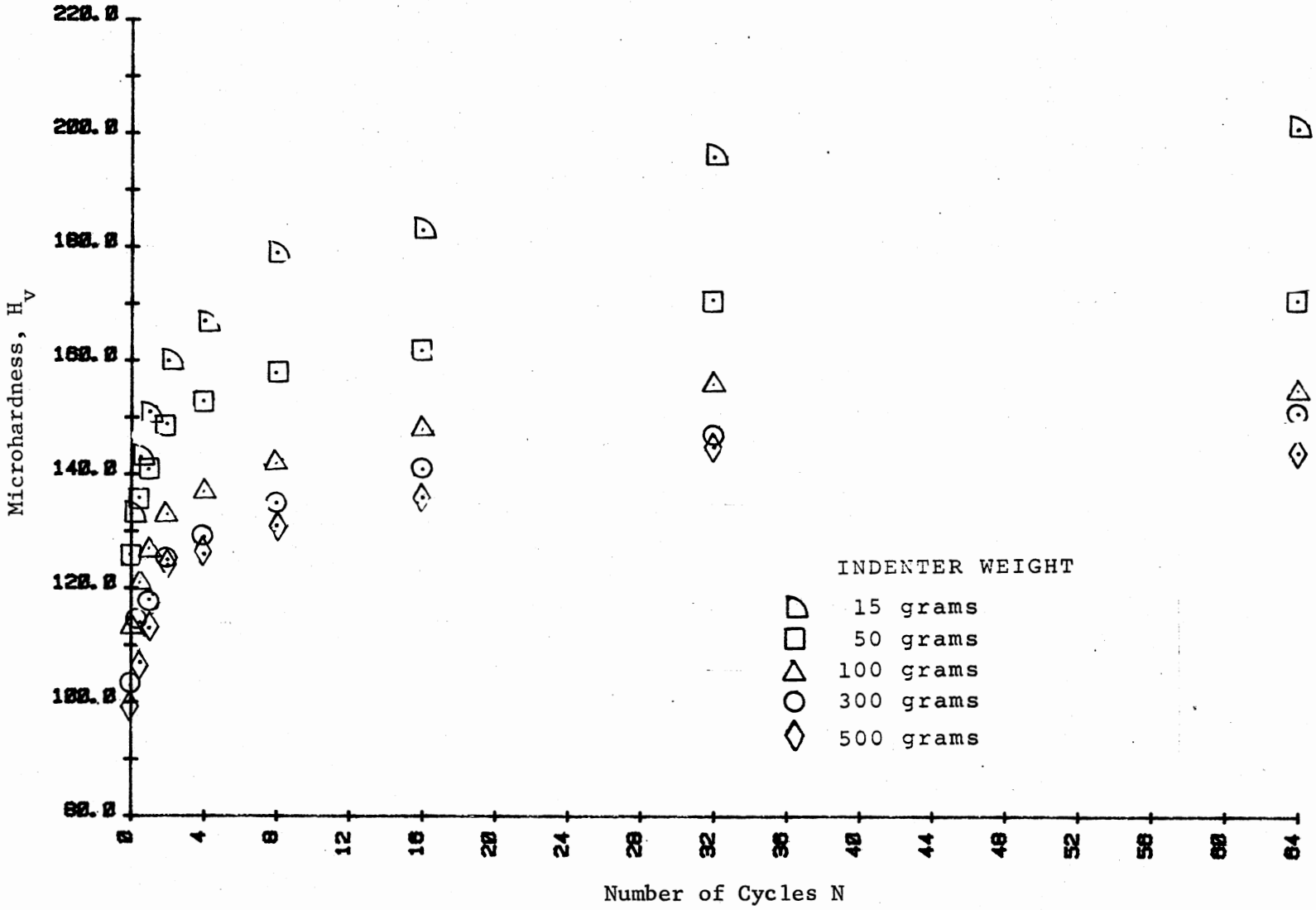

Figure 25. (Continued)

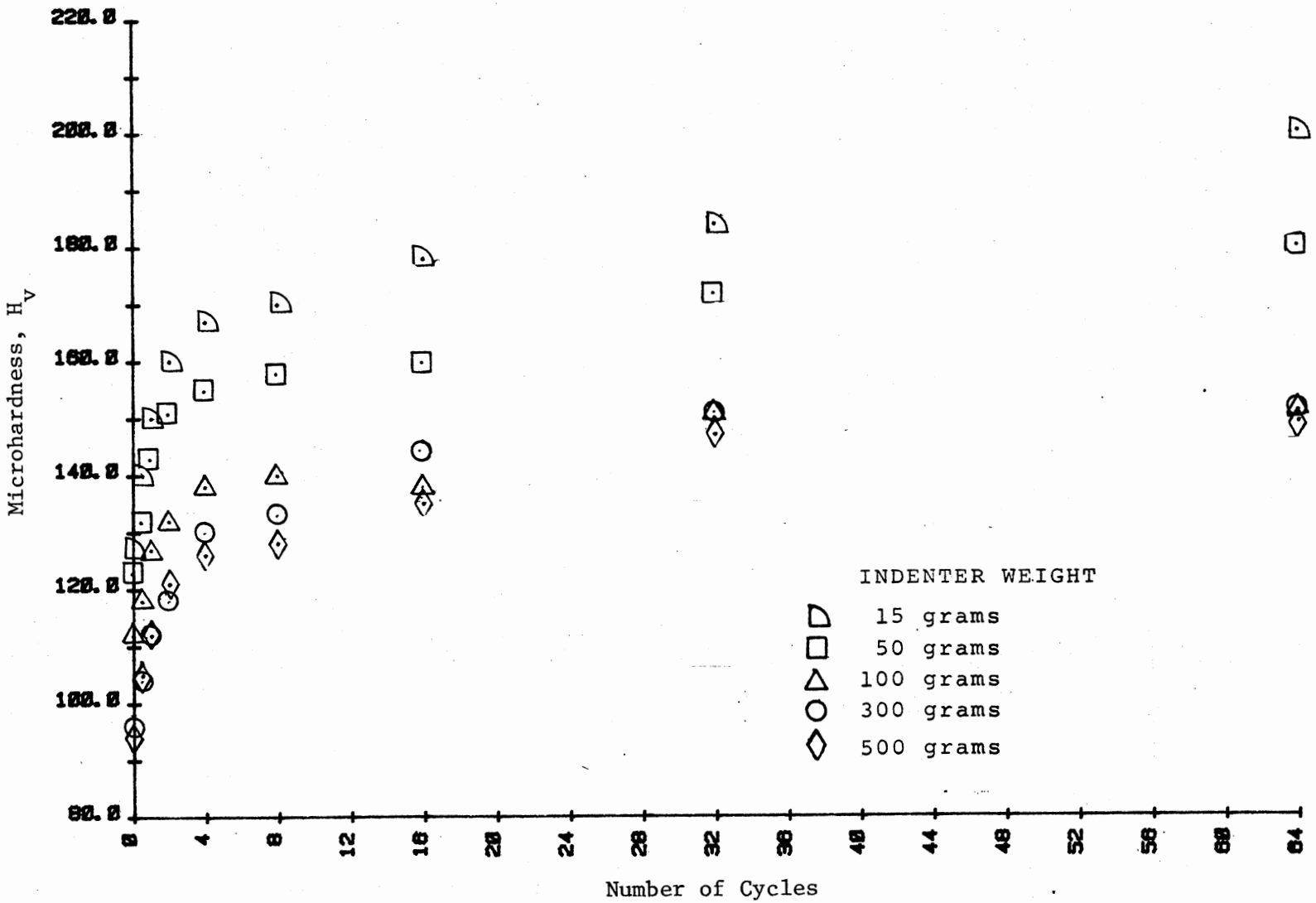

Figure 25. (Continued)

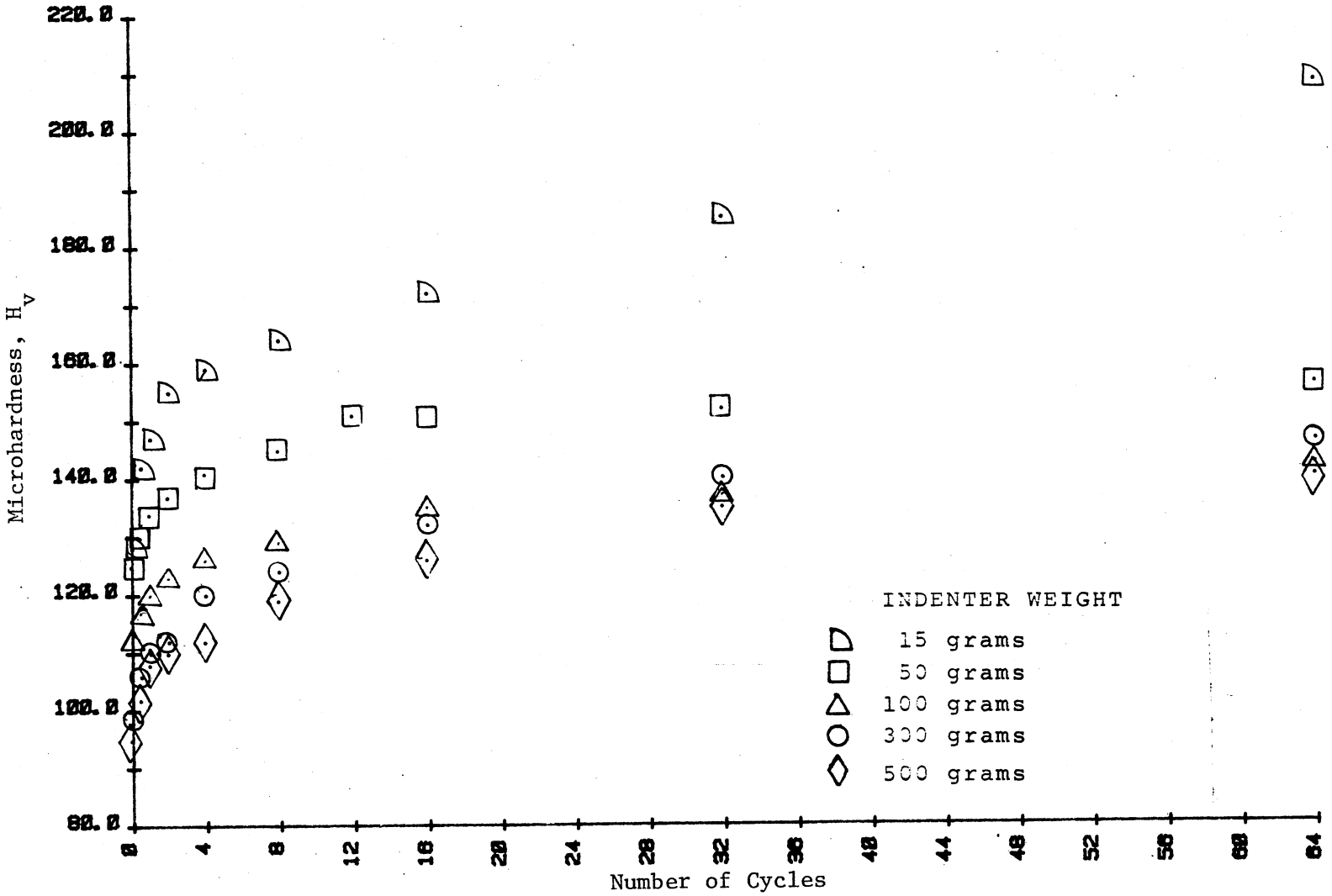

Figure 25. (Continued)

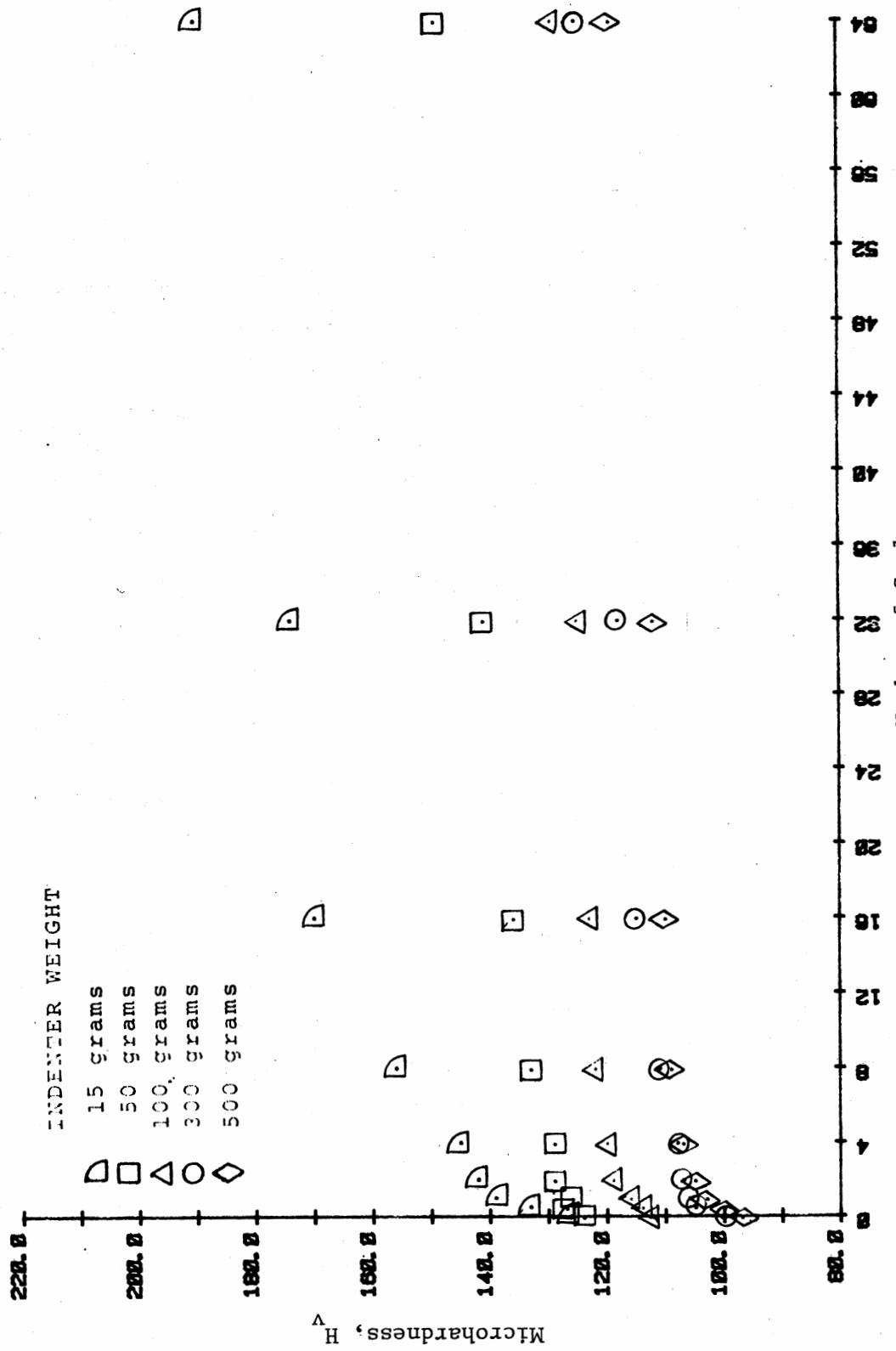

Figure 25. (Continued)

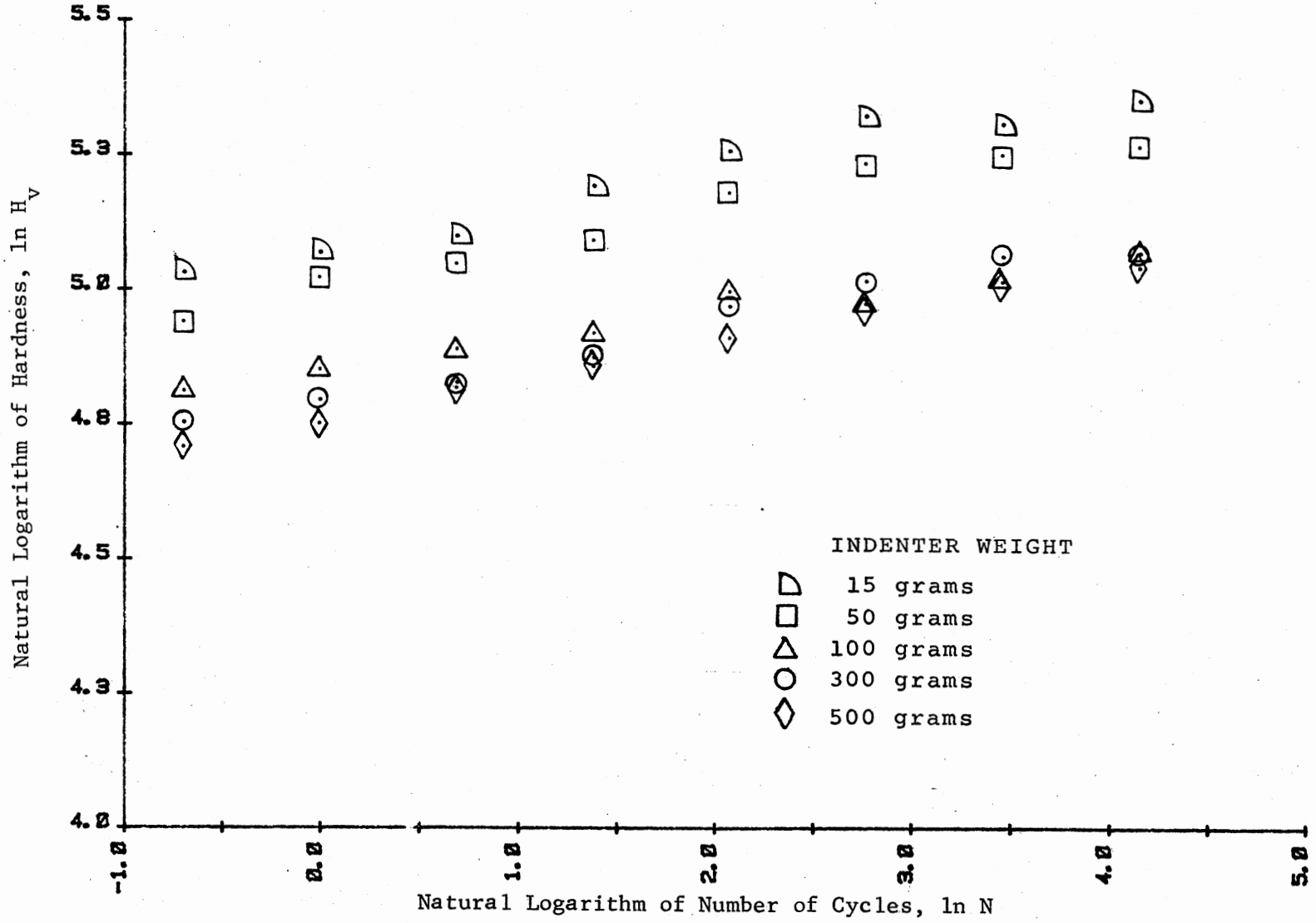

Figure 26. Graph of Natural Logarithm of Hardness Versus Natural Logarithm of Number of Cycles (Deflection Setting No. 1)

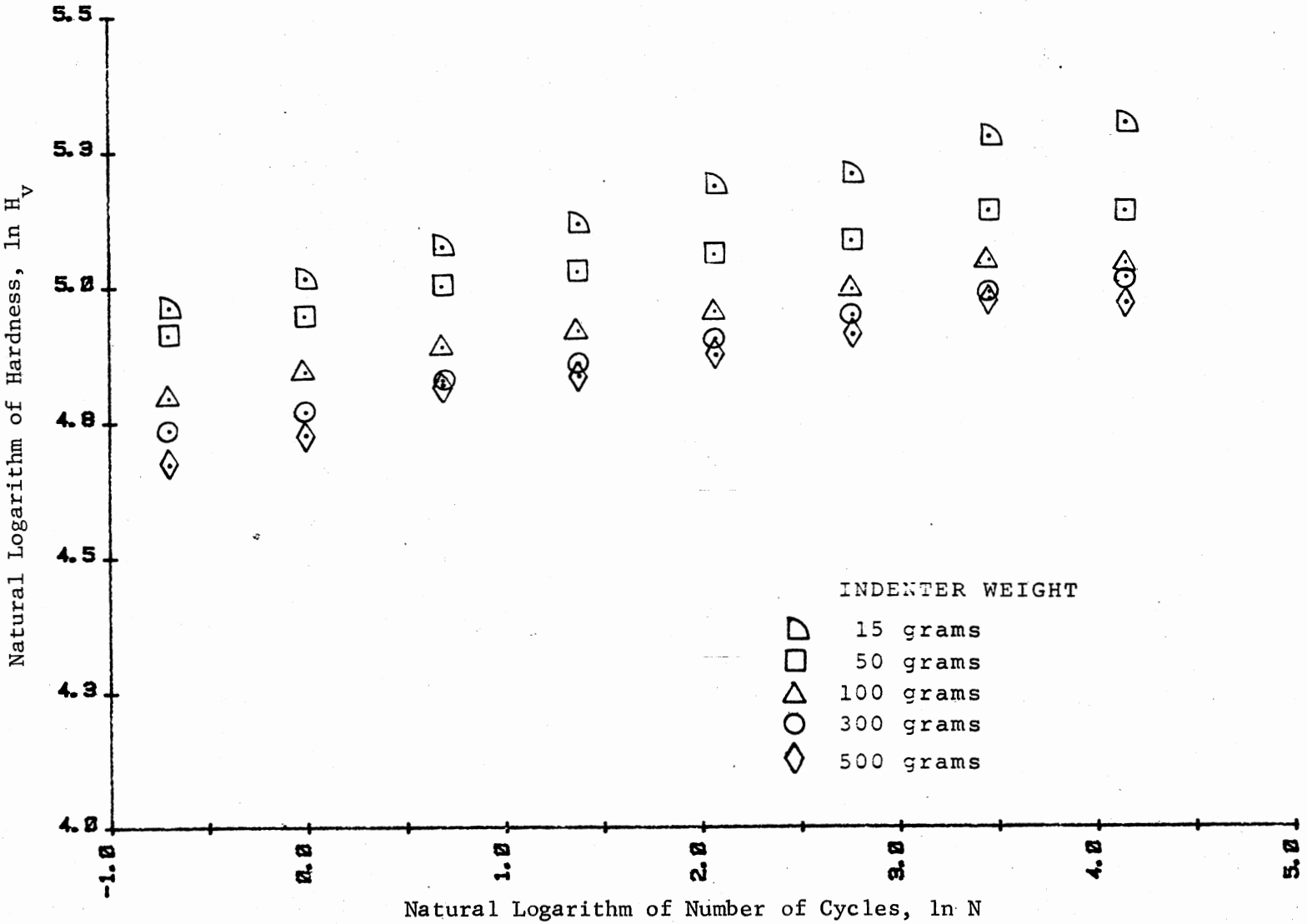

Figure 26. (Continued)

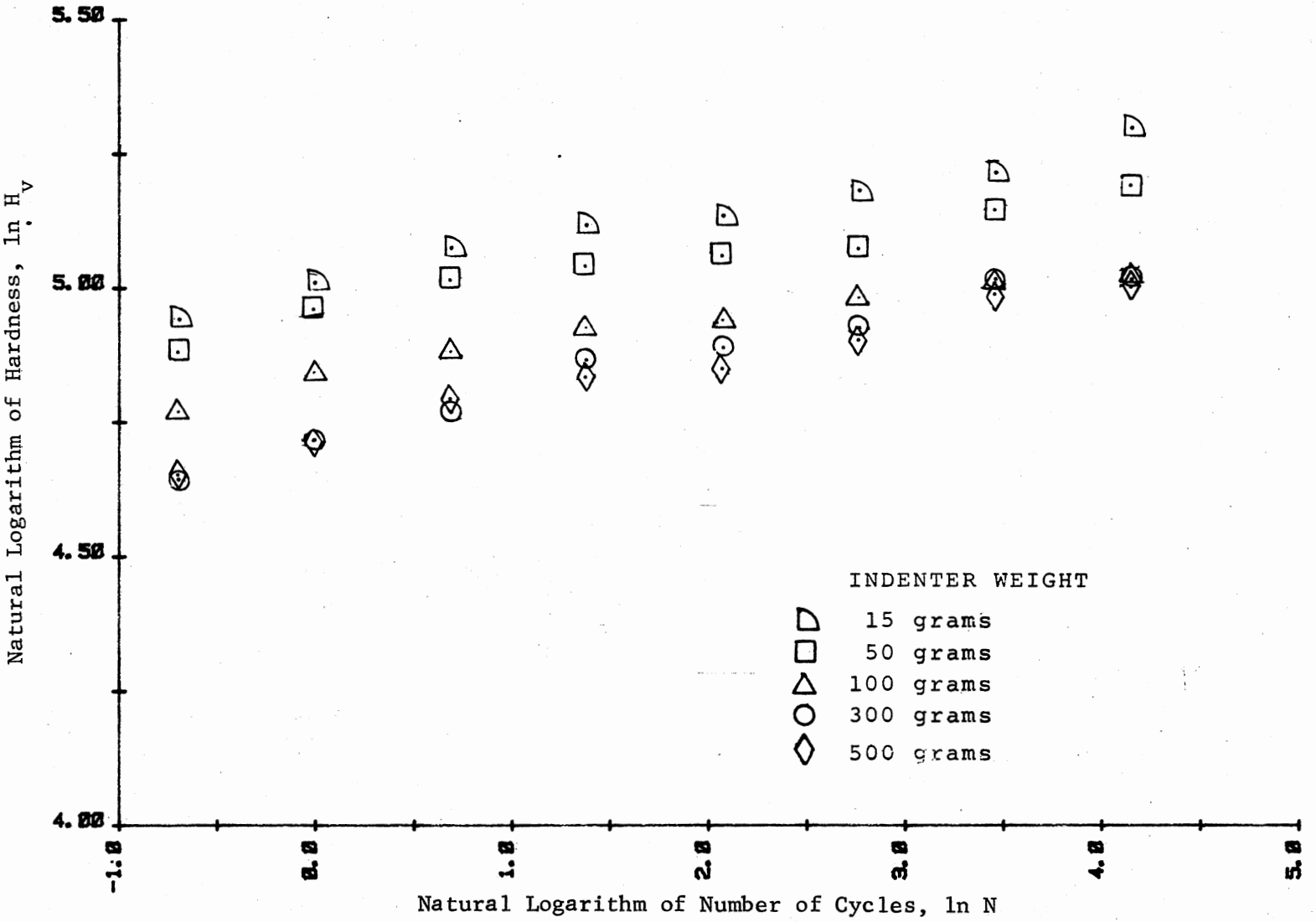

Figure 26. (Continued)

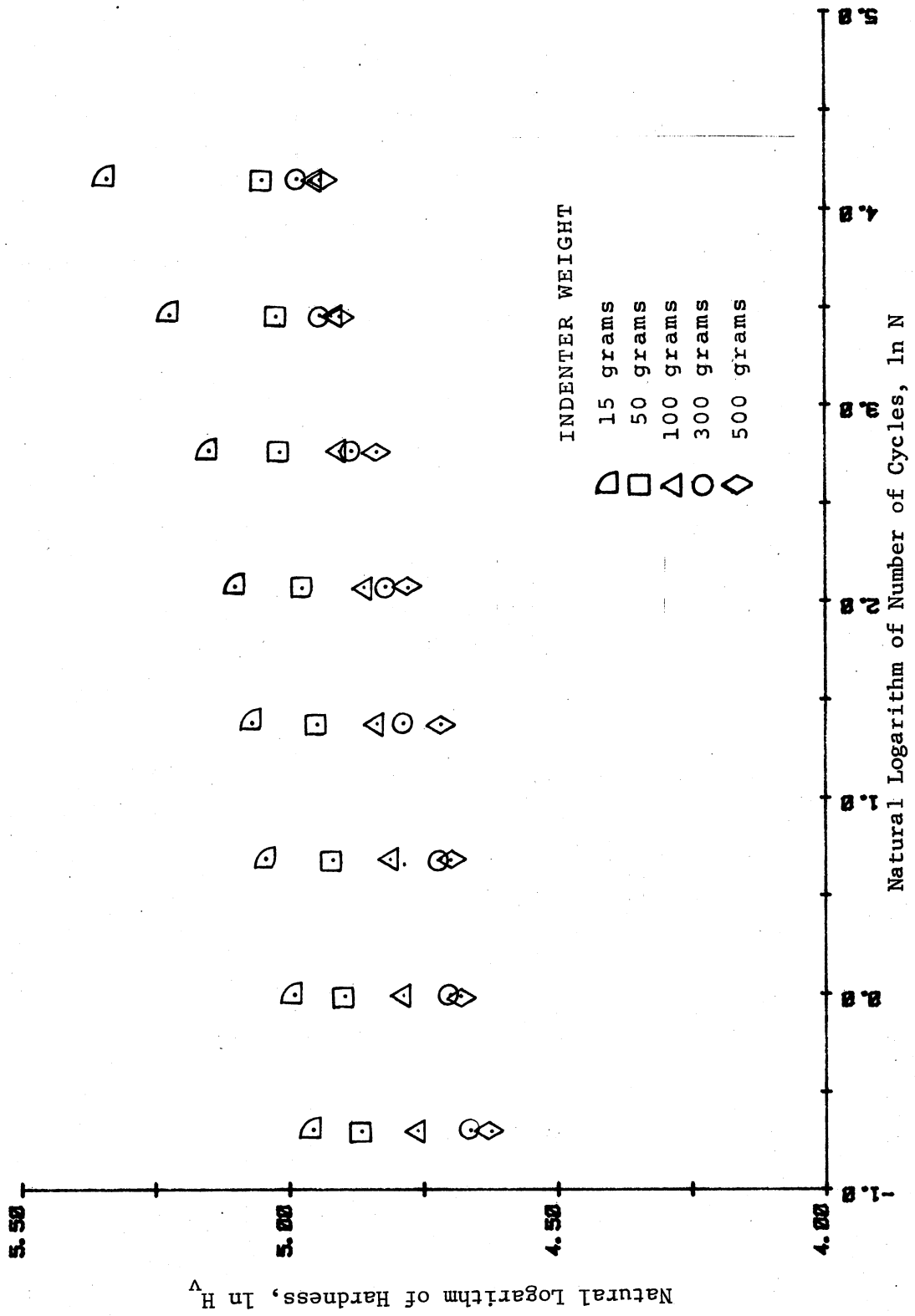

Figure 26. (Continued)

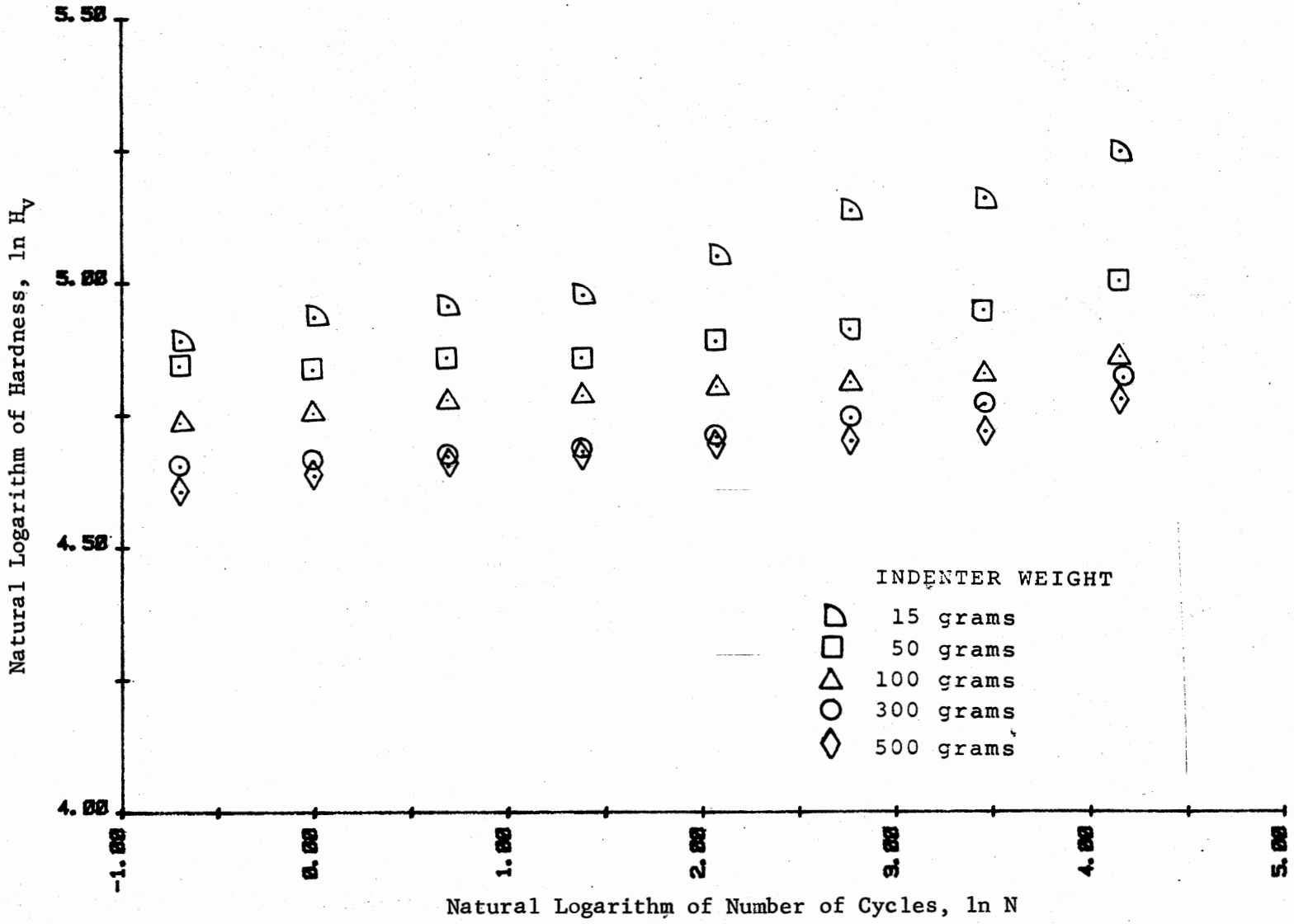

Figure 26. (Continued)

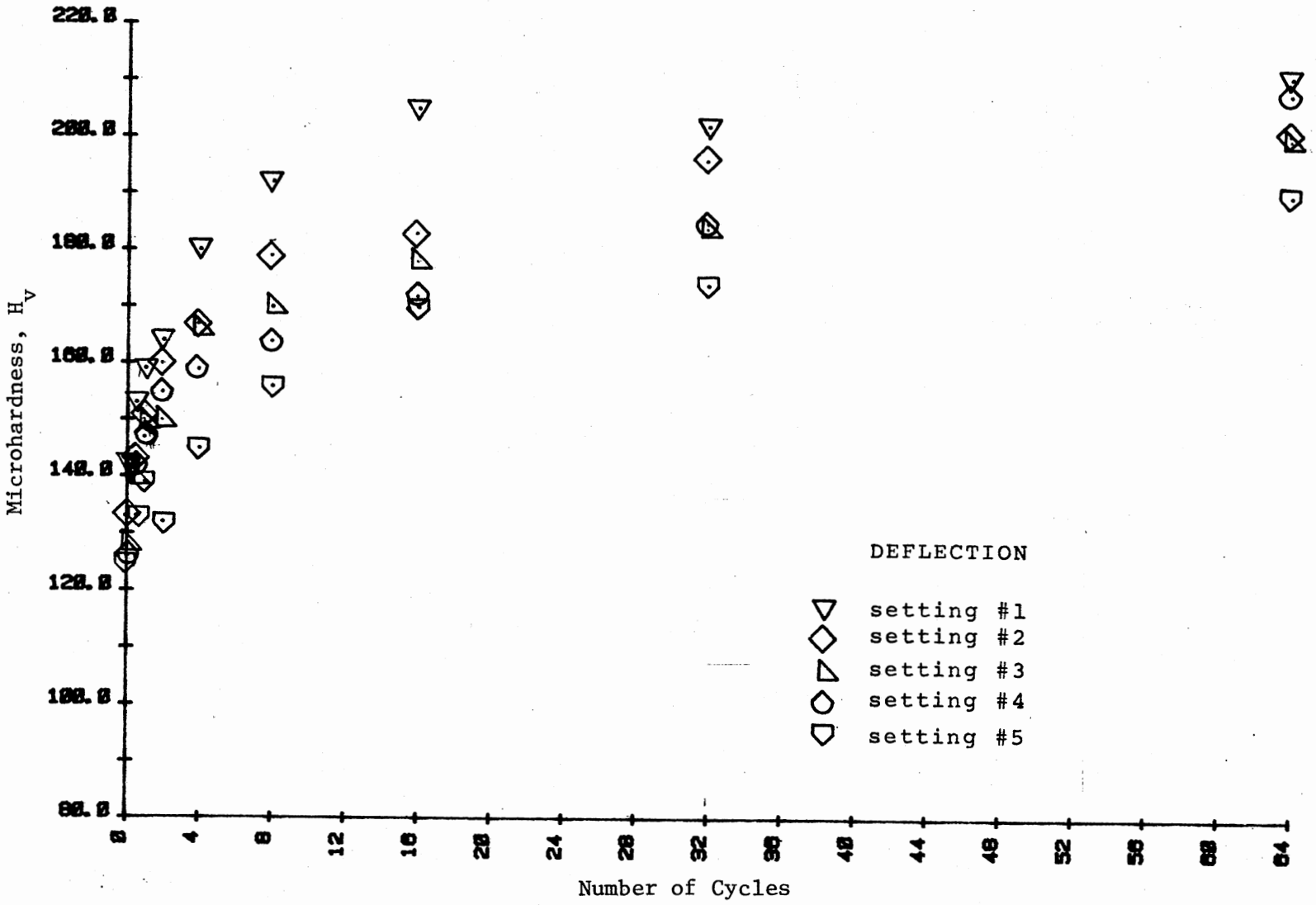

Figure 27. Microhardness H_V Versus Number of Cycles N Curve (15 Grams Indenter Weight, 5 Deflection Settings)

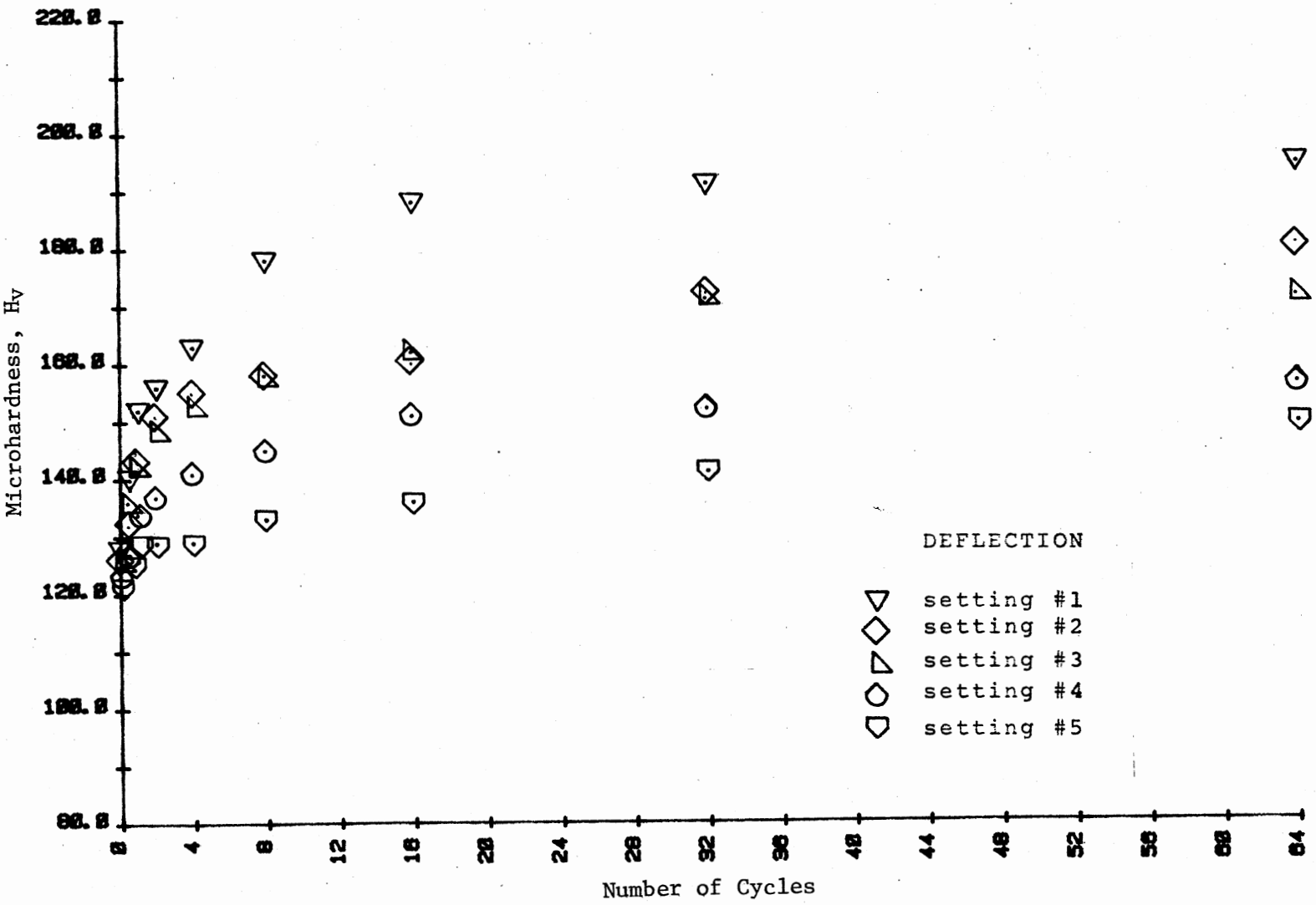

Figure 27. (Continued)

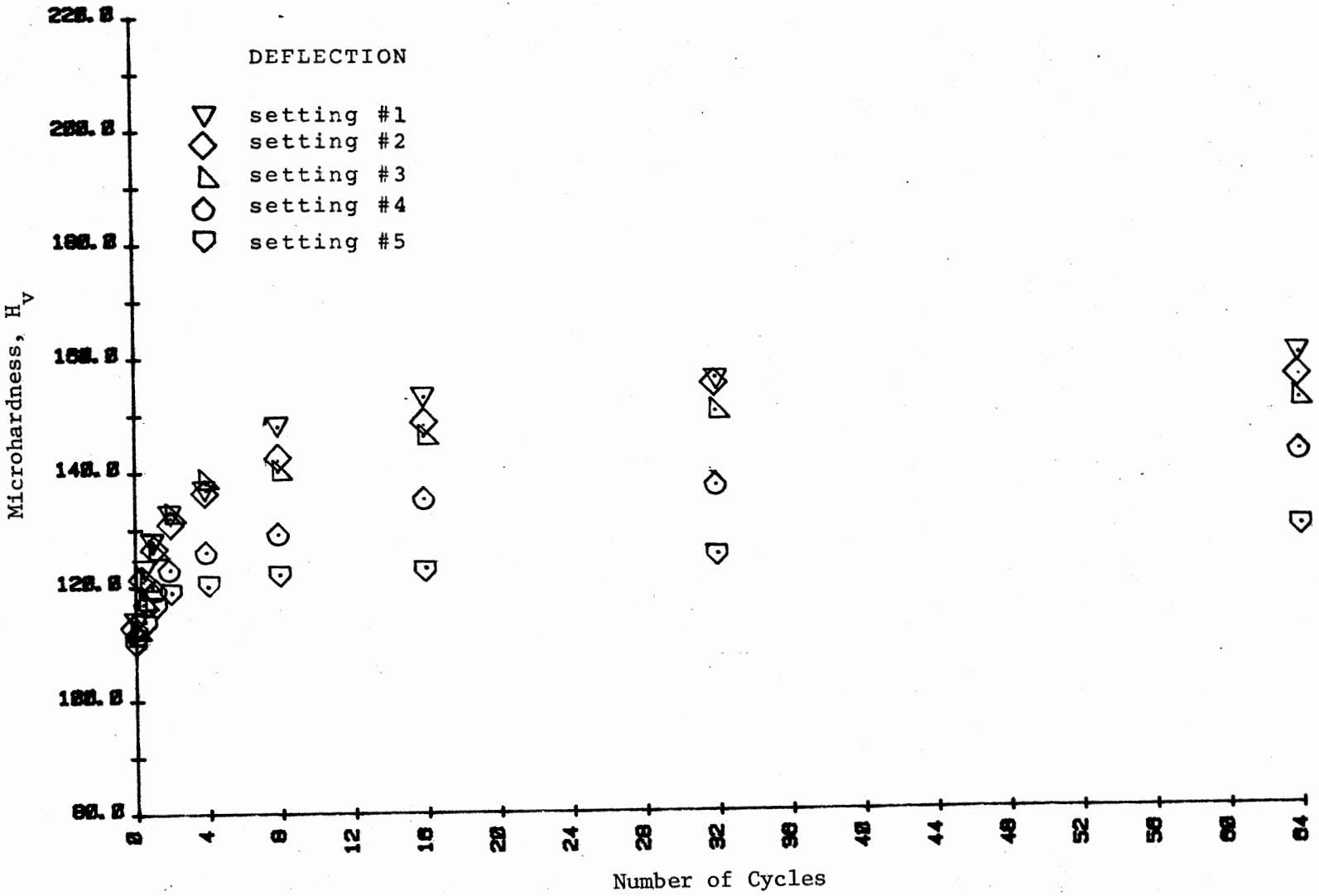

Figure 27. (Continued)

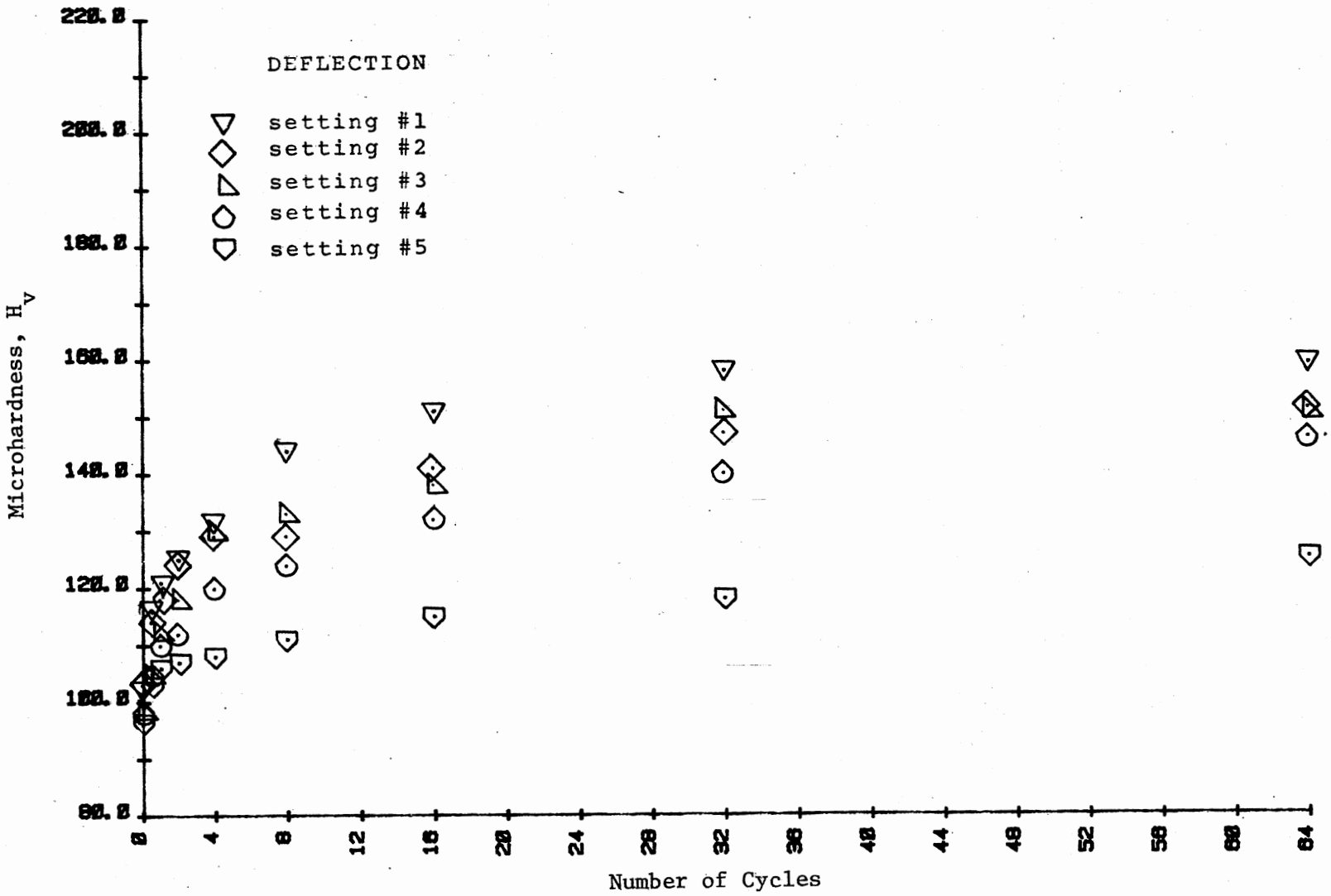

Figure 27. (Continued)

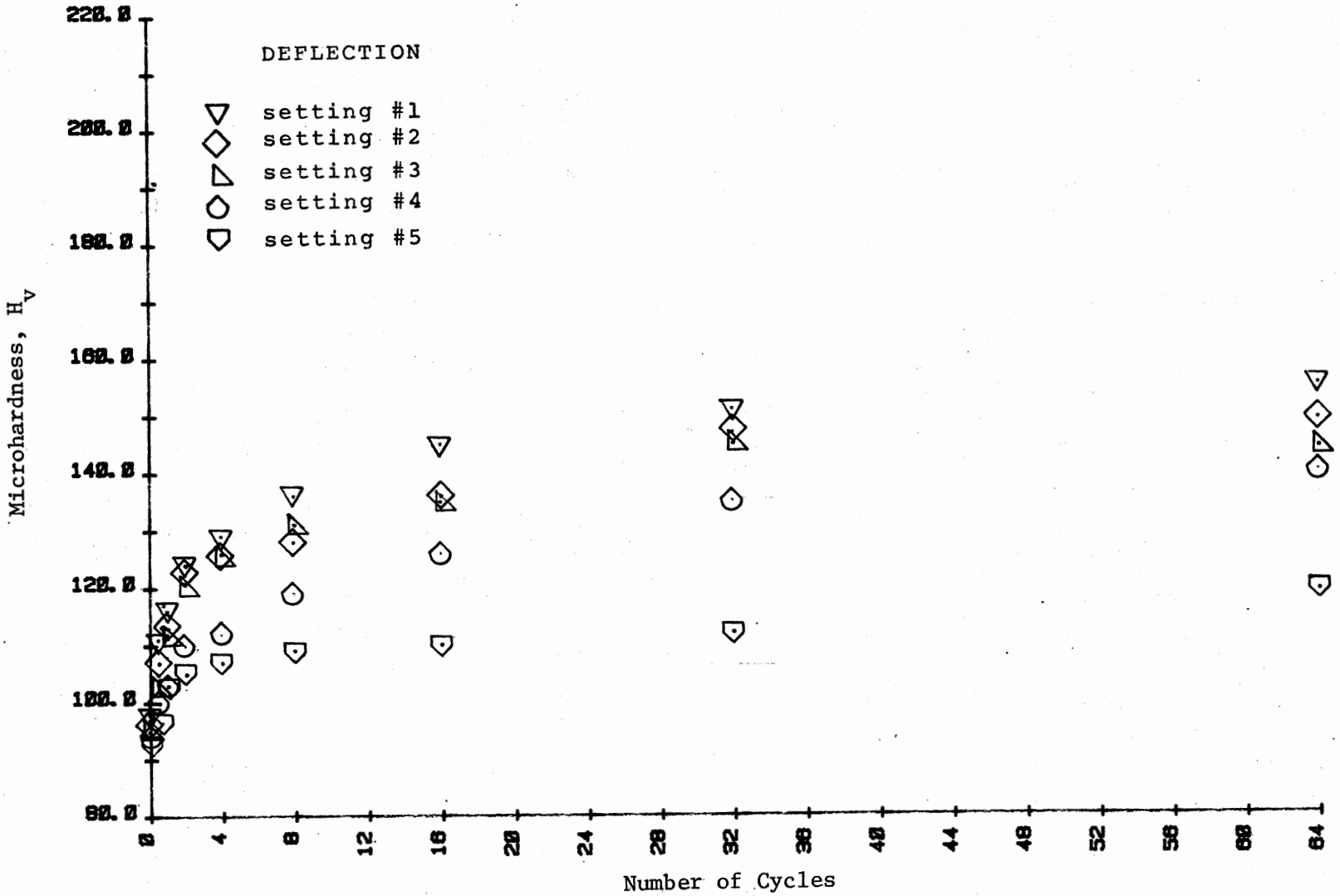

Figure 27. (Continued)

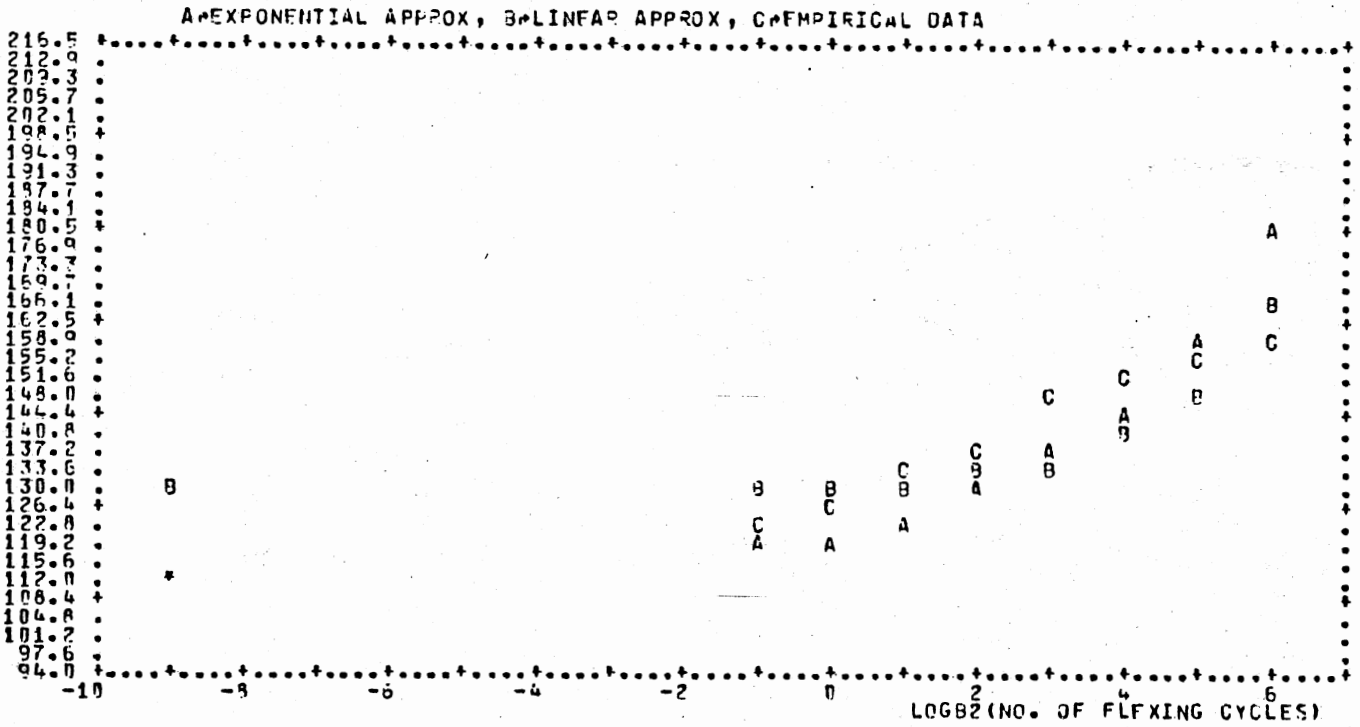

Figure 28. Graph Showing Microhardness Variation Versus Number of Cycles (Indenter Weight W = 200, Deflection Setting S = 1)

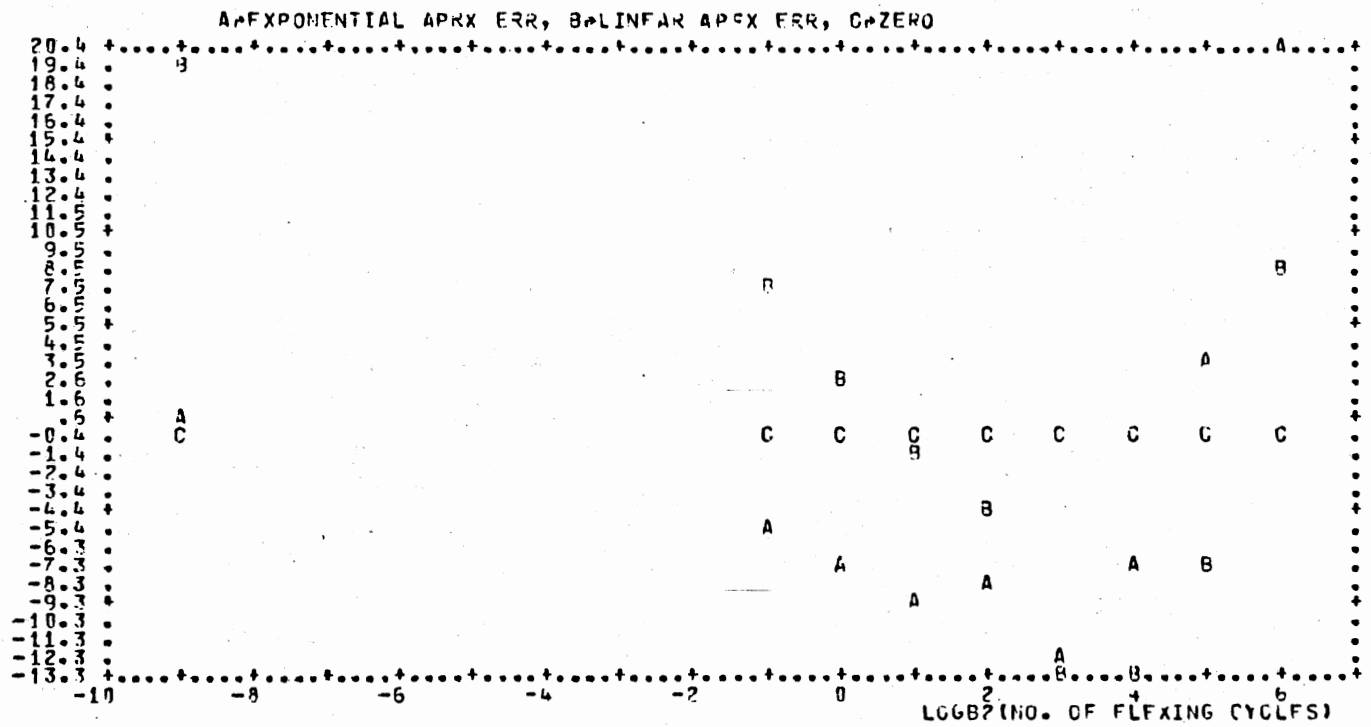

Figure 29. Graph Showing Exponential and Linear Approximation Errors (see Figure 28)

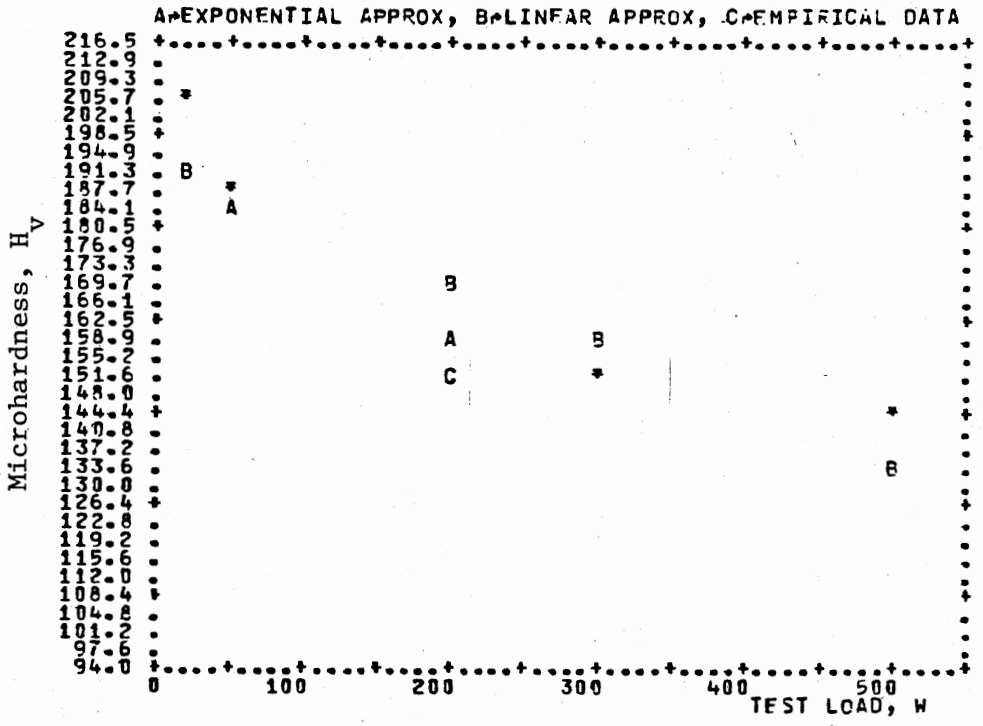

Figure 30. Graph Showing Microhardness H_V Versus Indenter Weight at the Deflection Setting S = 1 and After N = 16 Cycles

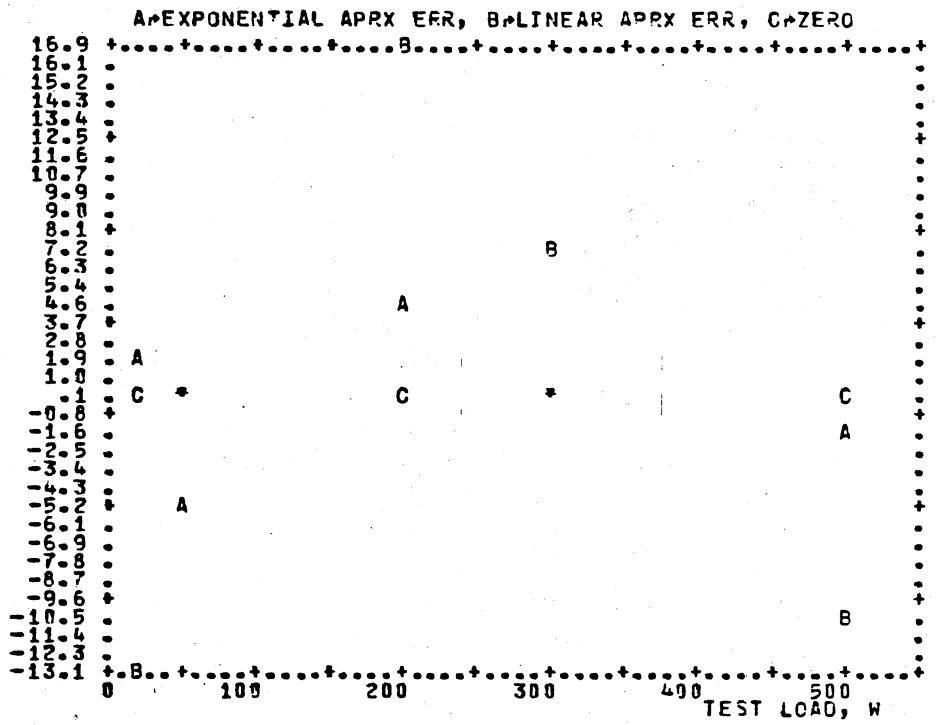

Figure 31. Graph Showing Exponential and Linear Approximation Errors (see Figure 30) for Deflection Setting S = 1 and After Number of Cycles N = 16

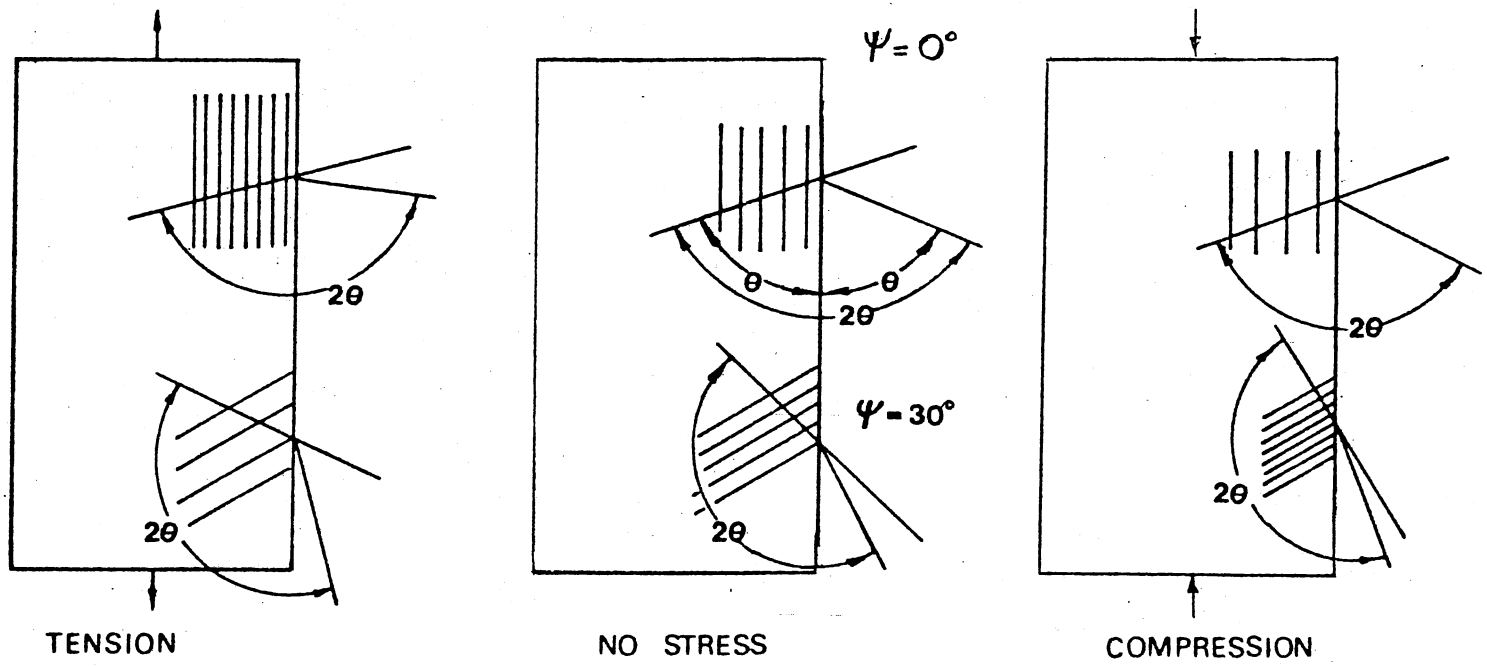

Figure 32. Schematic Diagram Showing Effect of Stress in Interplanar Spacing (d) and X-Ray Diffraction Angle (2θ) for Crystallographic Planes Parallel to and at the Angle of 30° to the Surface

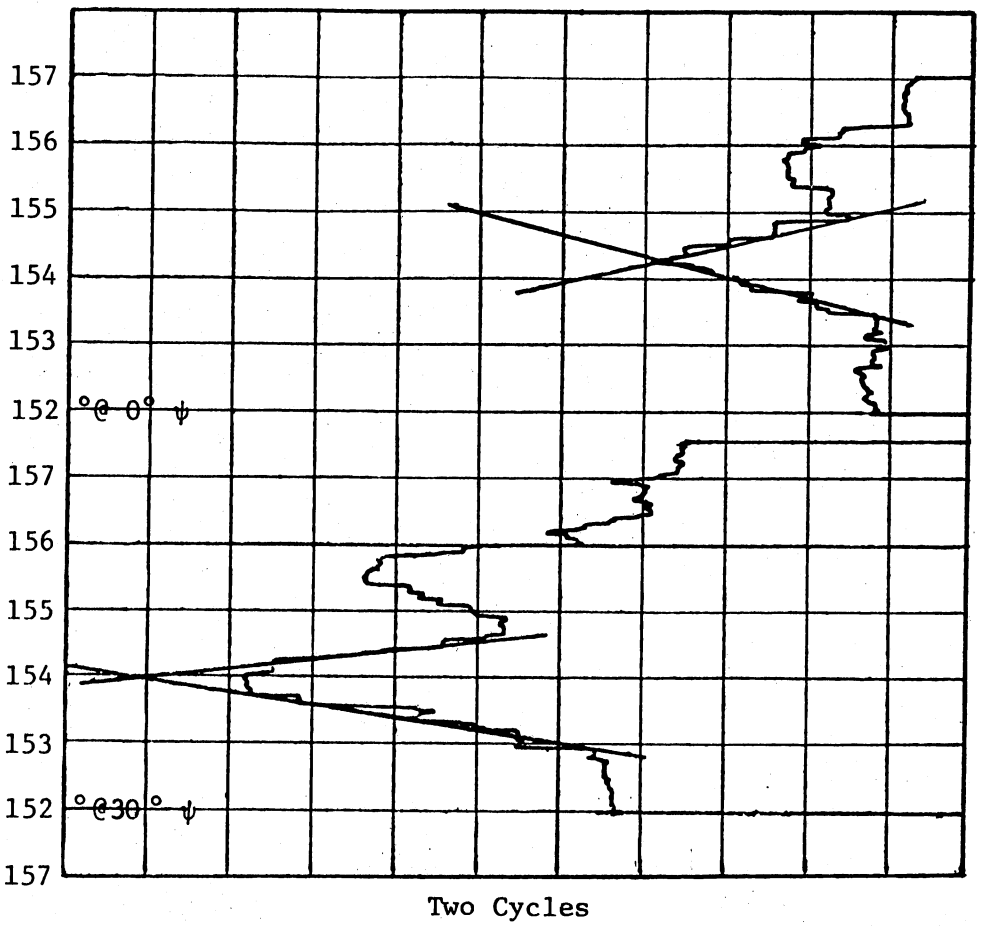

Figure 33. Determination of the Change of Diffraction Angle by Triangular Method

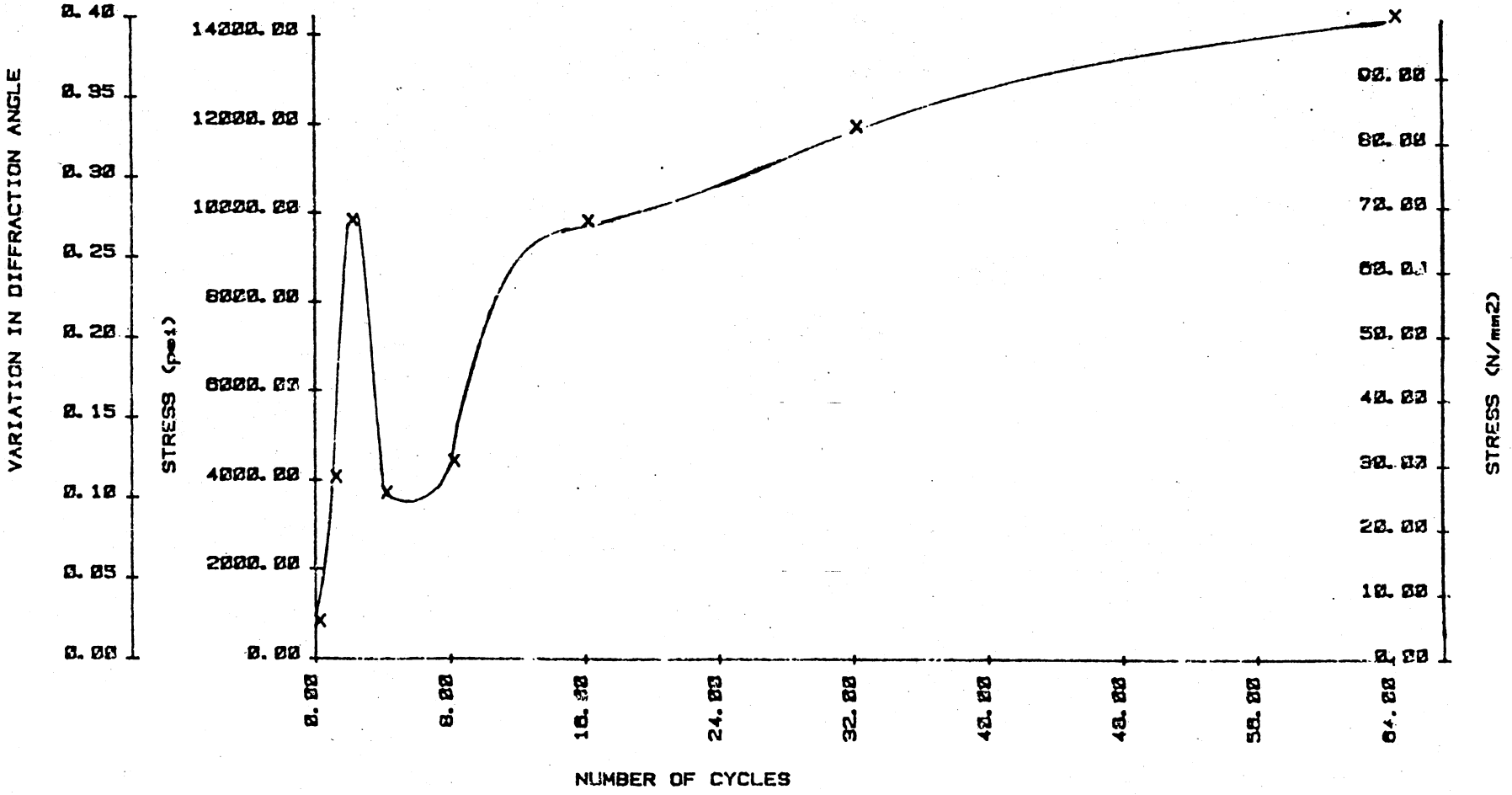

Figure 34. Graphs of Change of the Diffraction Angle (2θ) and Macrostress Versus the Number of Flexing Cycles (N)

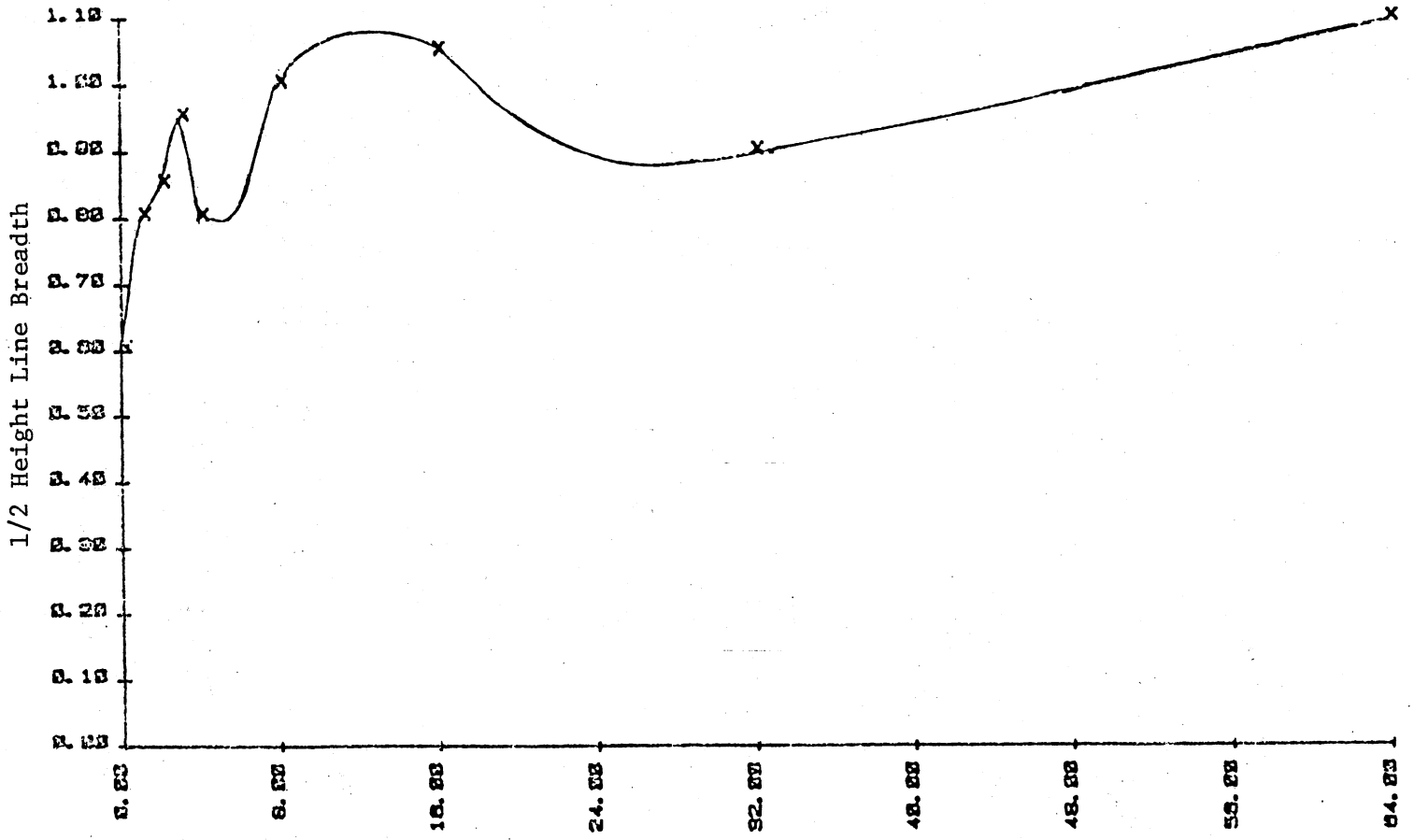

Figure 35. Graph of Changes in Half Value Breadth (Line Broadening), (β) or Microstrain During the Fatigue Process

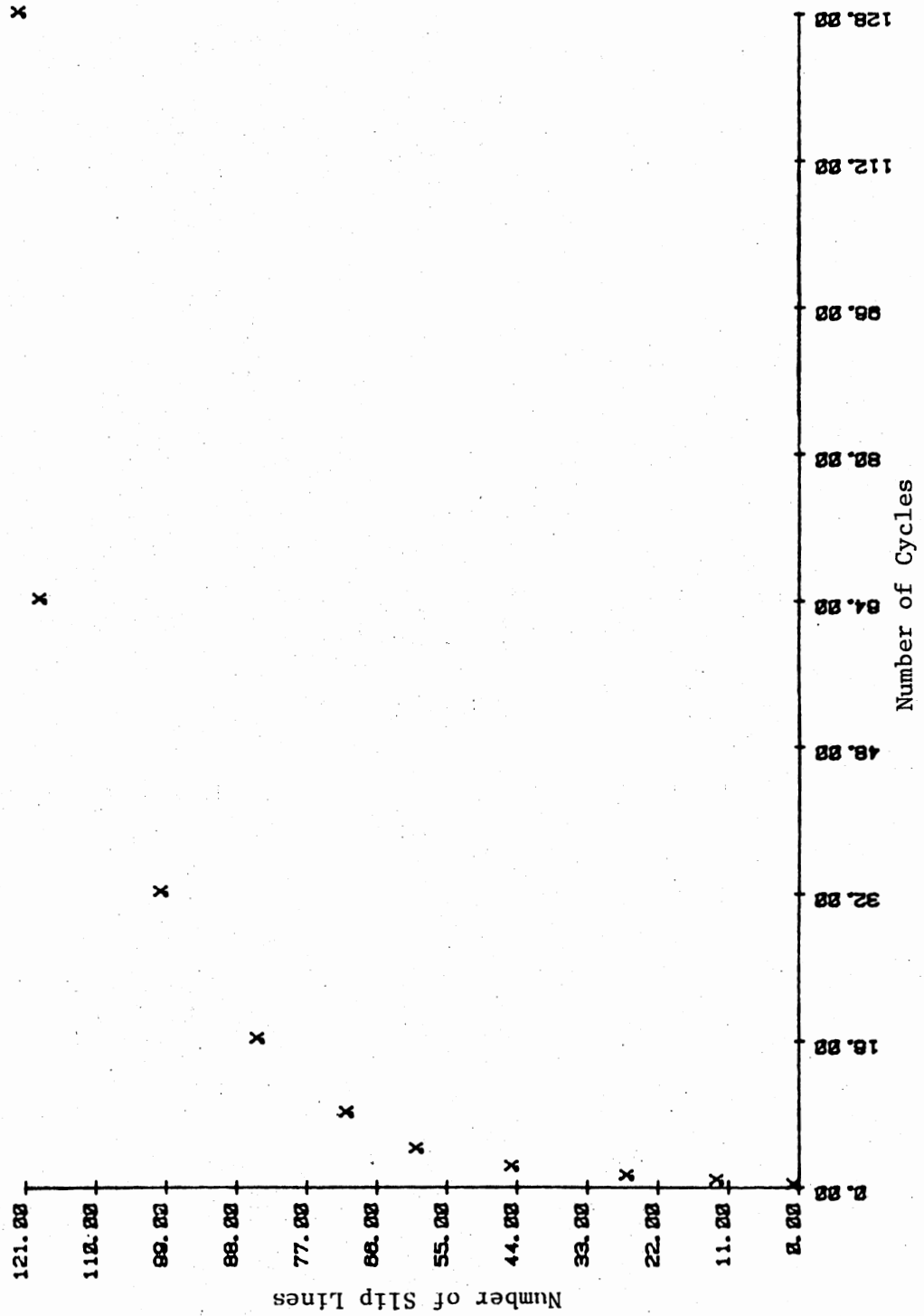

Figure 36. Graph of Number of Slip Bands n Versus Number of Flexing Cycles N

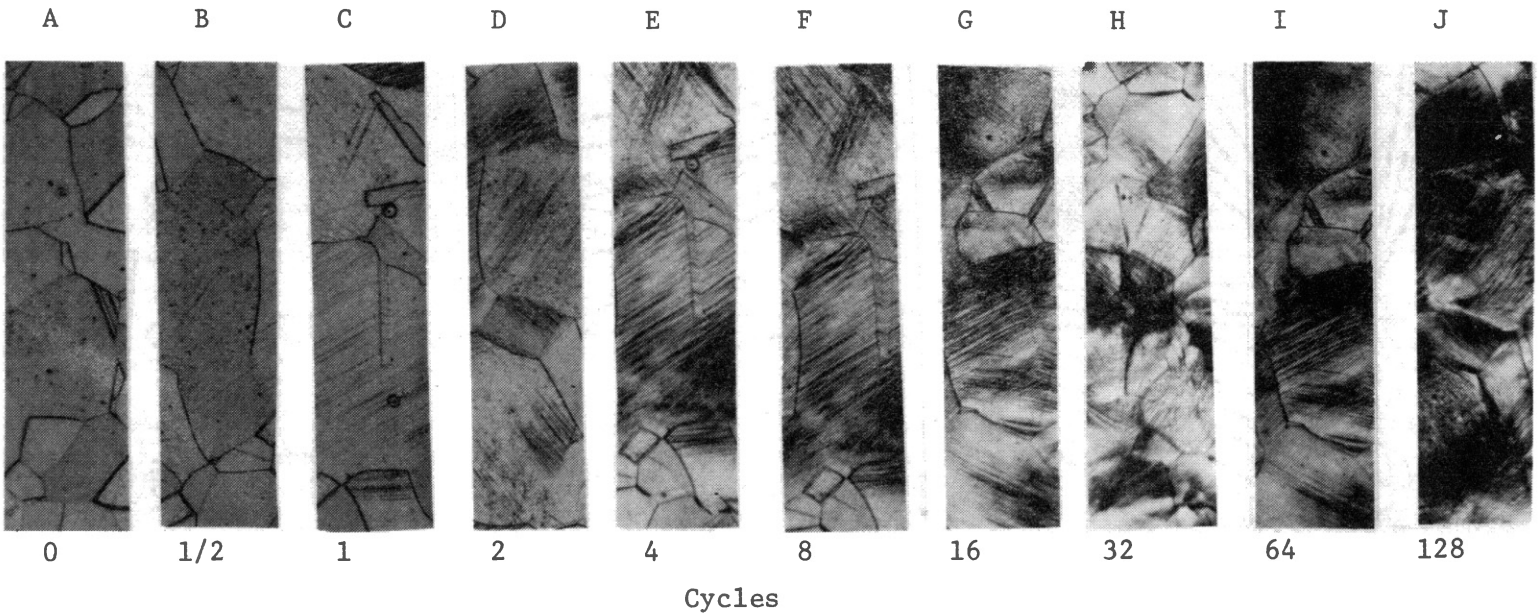

Figure 37. Development of Slip Bands Leading to Fatigue Crack Initiation in Nickel 200

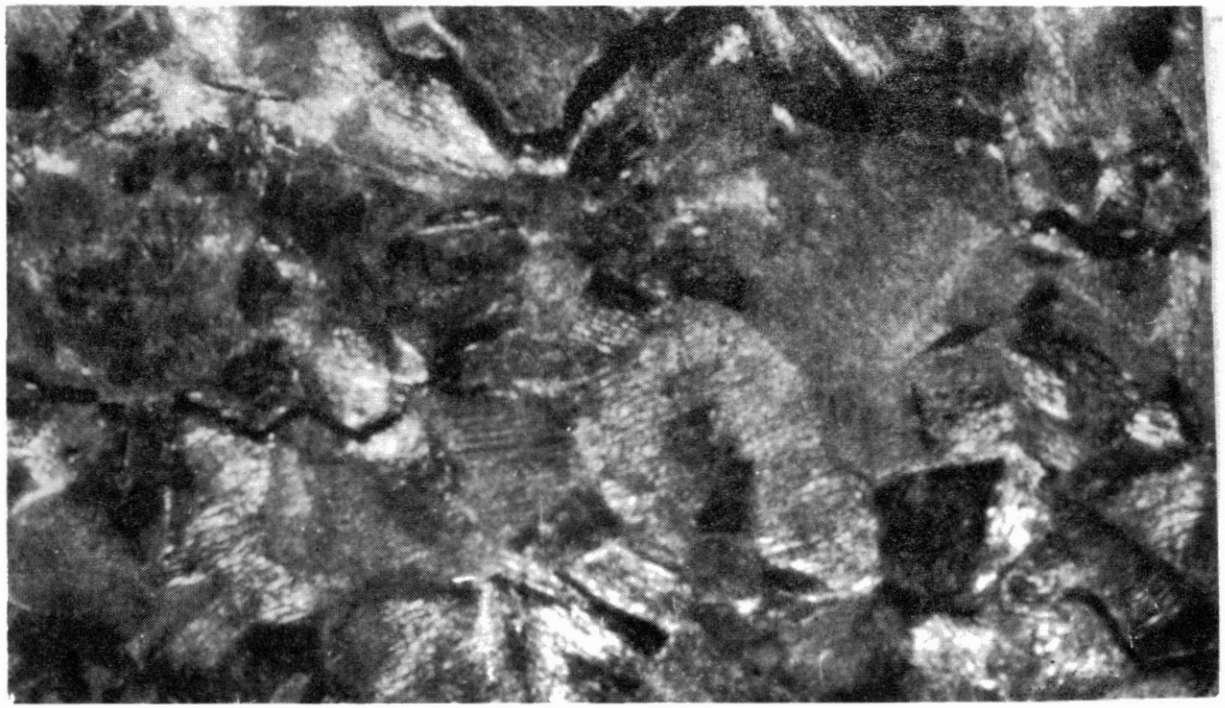

Figure 38. Optical Micrograph Showing Crack Growth Occurring Mostly Along Grain Boundaries

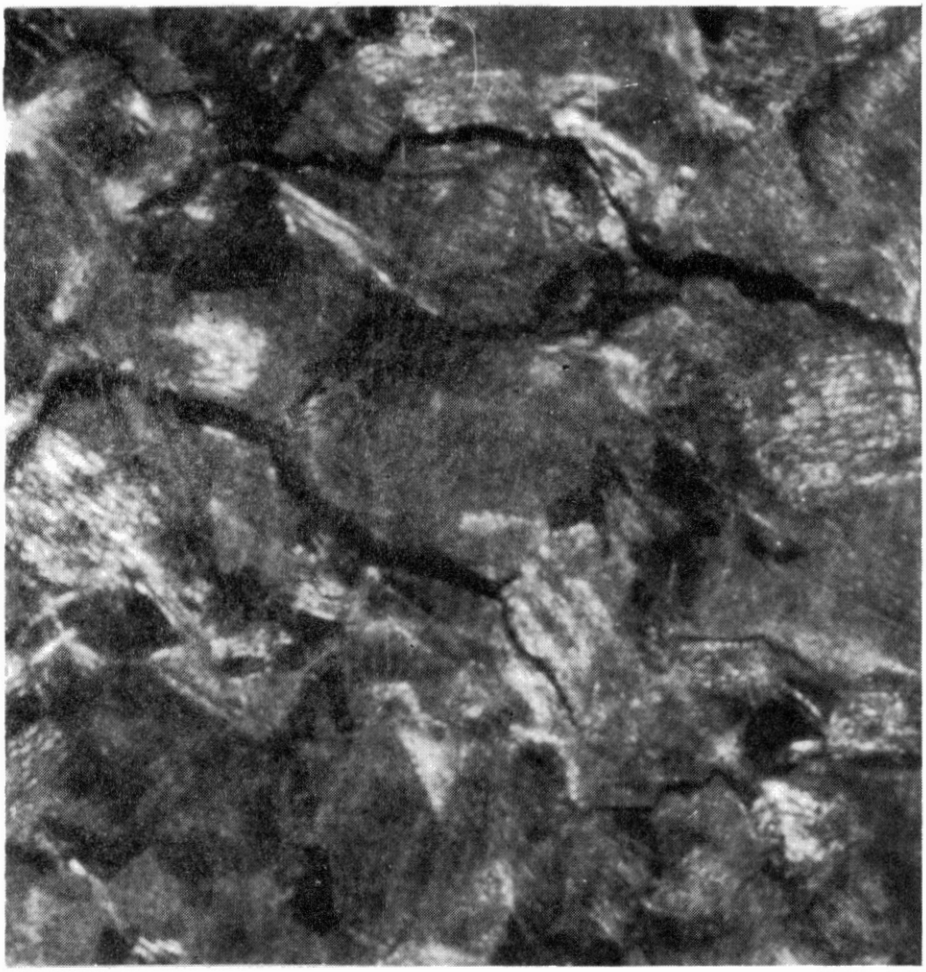

Figure 39. Optical Micrograph Showing Crack Spreading Into a Zone of Reduced Stress and Turning Into a Slip Band Within a Grain

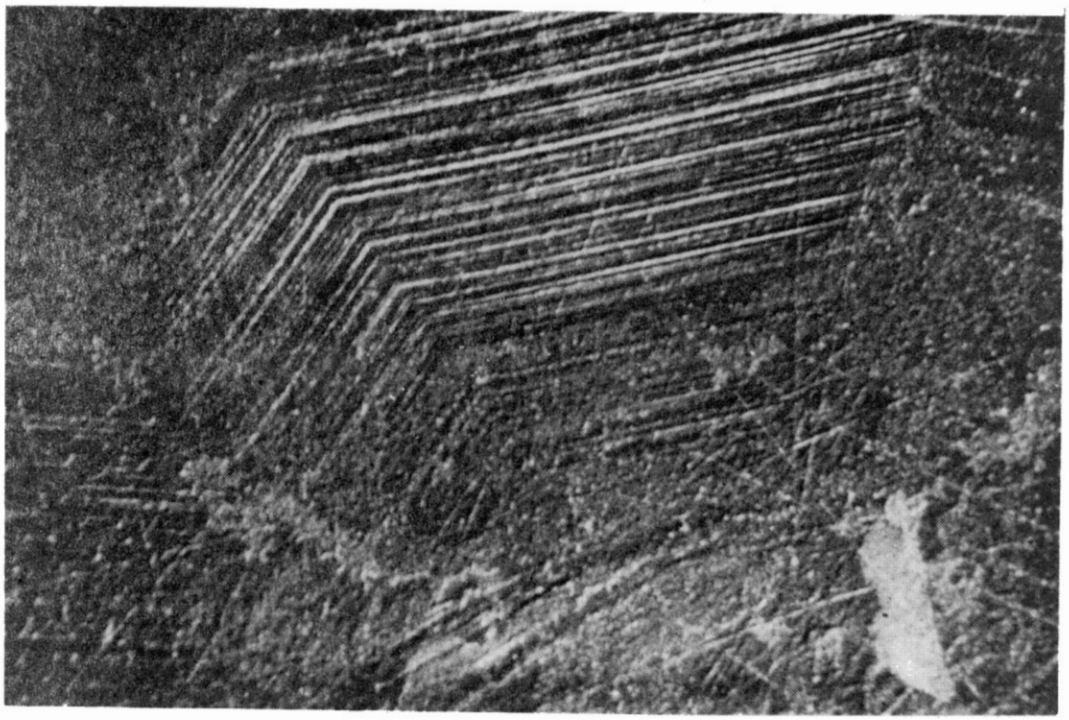

(a) Replica After 4 Cycles, 1000x

Figure 40. Scanning Electron Micrographs of Specimen Surface

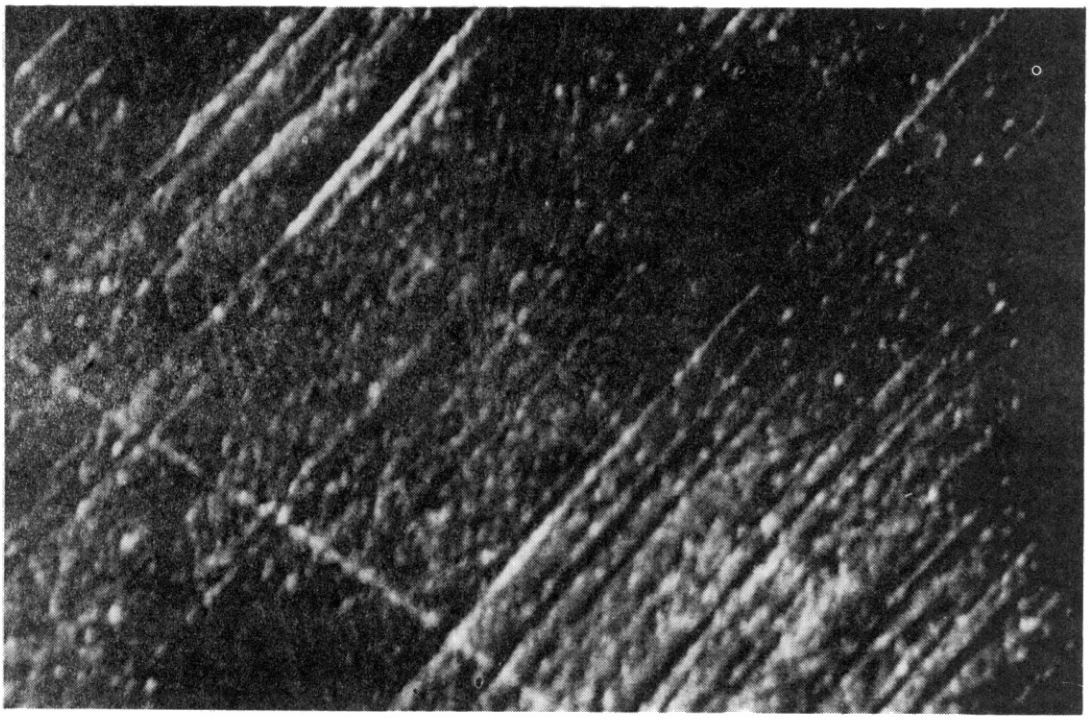

(b) Replica After 4 Cycles, 2000x

Figure 40. (Continued)

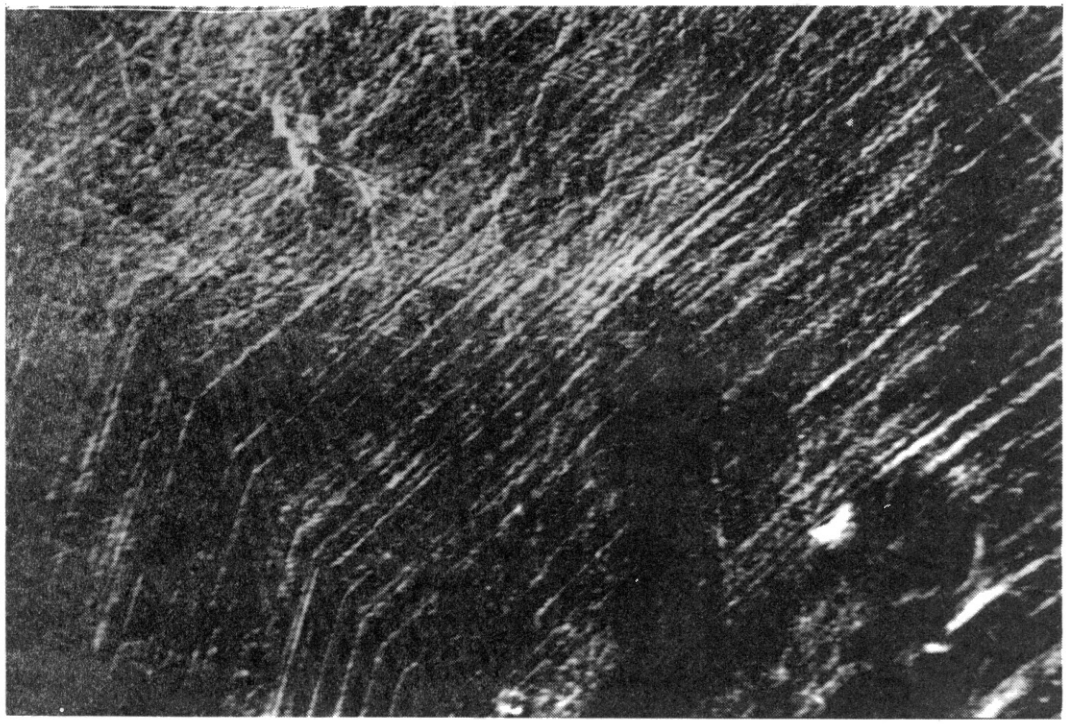

(c) Replica After 8 Cycles, 1000x

Figure 40. (Continued)

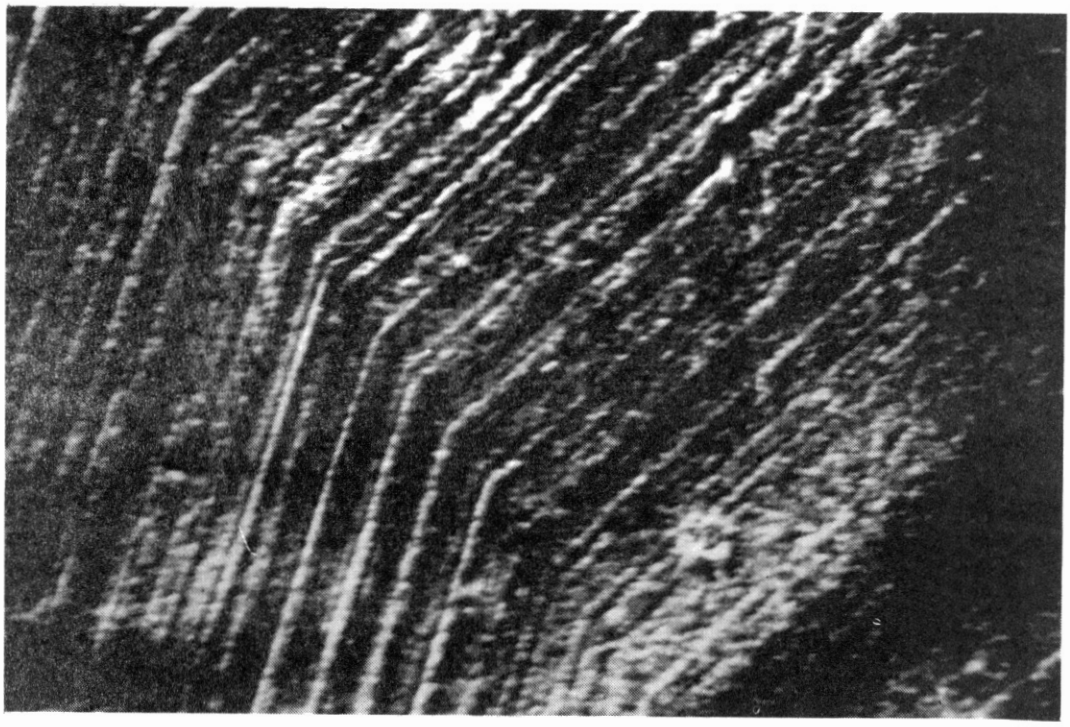

(d) Replica After 8 Cycles, 2000x

Figure 40. (Continued)

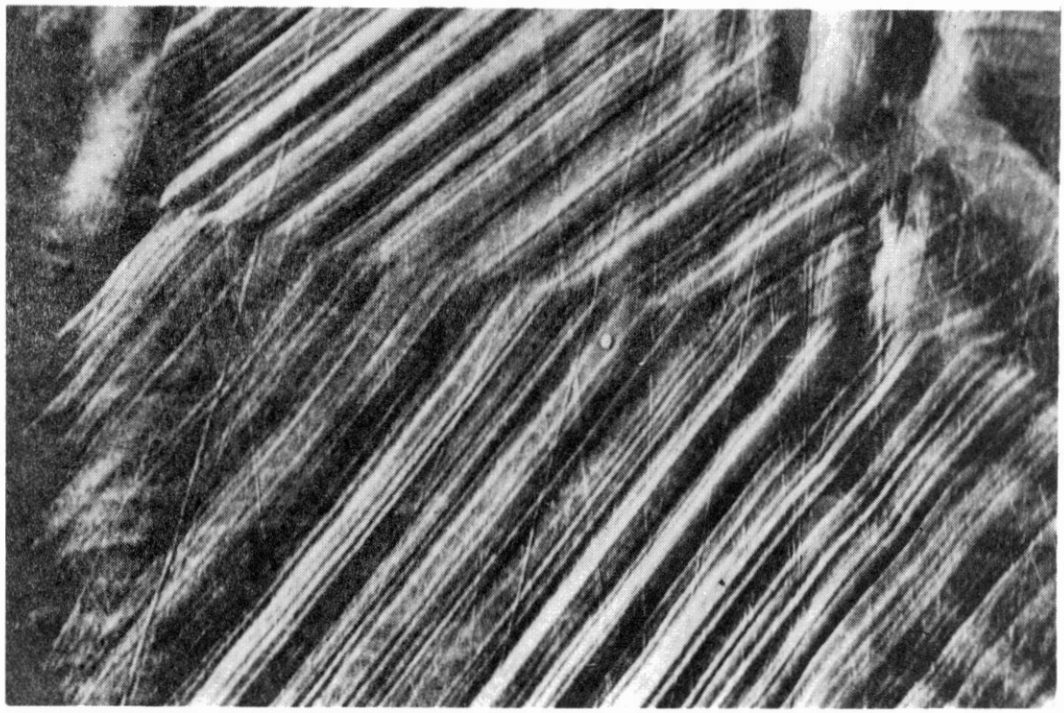

(e) Replica After 16 Cycles, 1000x

Figure 40. (Continued)

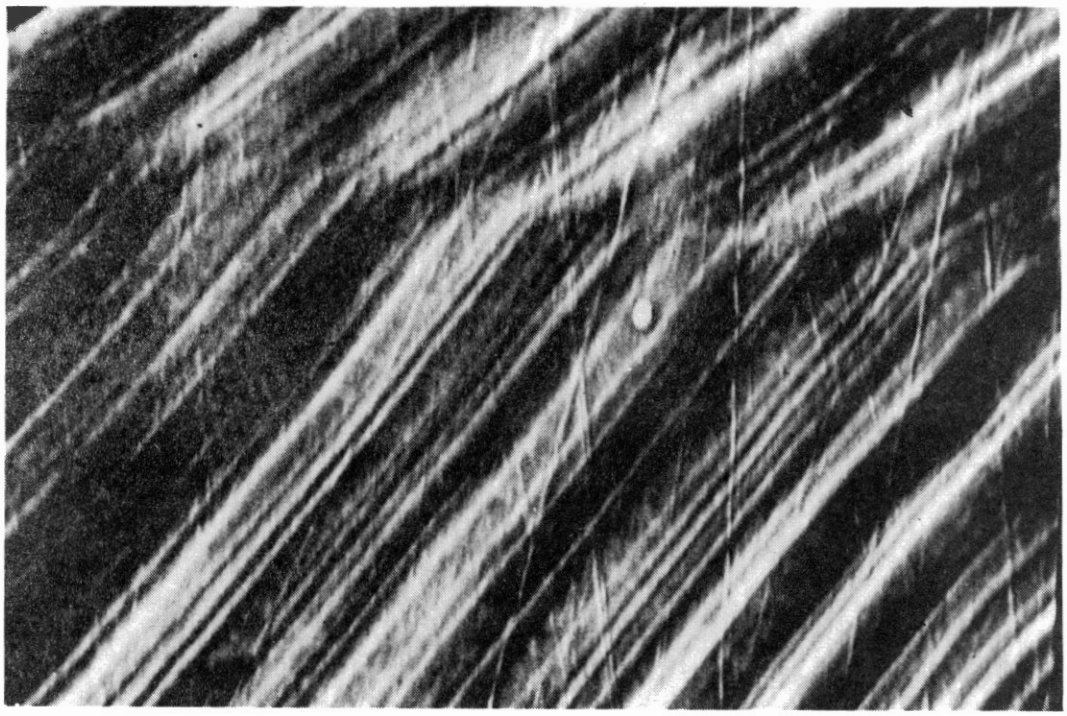

(f) Replica After 16 Cycles, 2000x

Figure 40. (Continued)

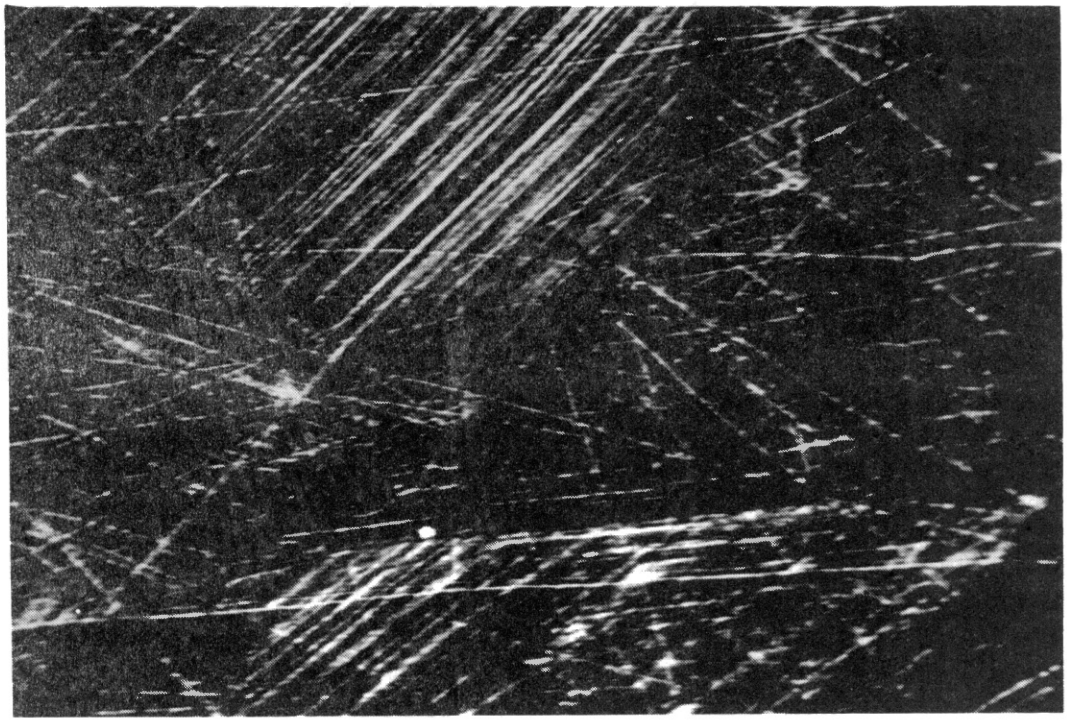

(g) Replica After 32 Cycles, 1000x

Figure 40. (Continued)

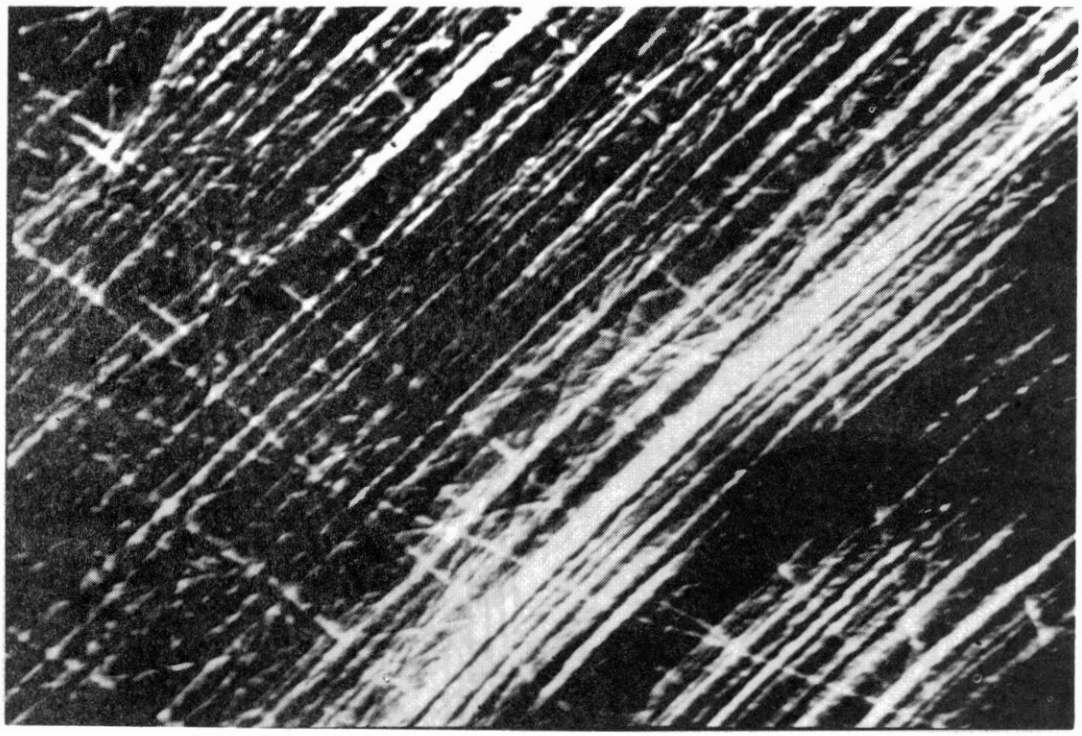

(h) Replica After 32 Cycles, 2000x

Figure 40. (Continued)

5.5" x 3.7"

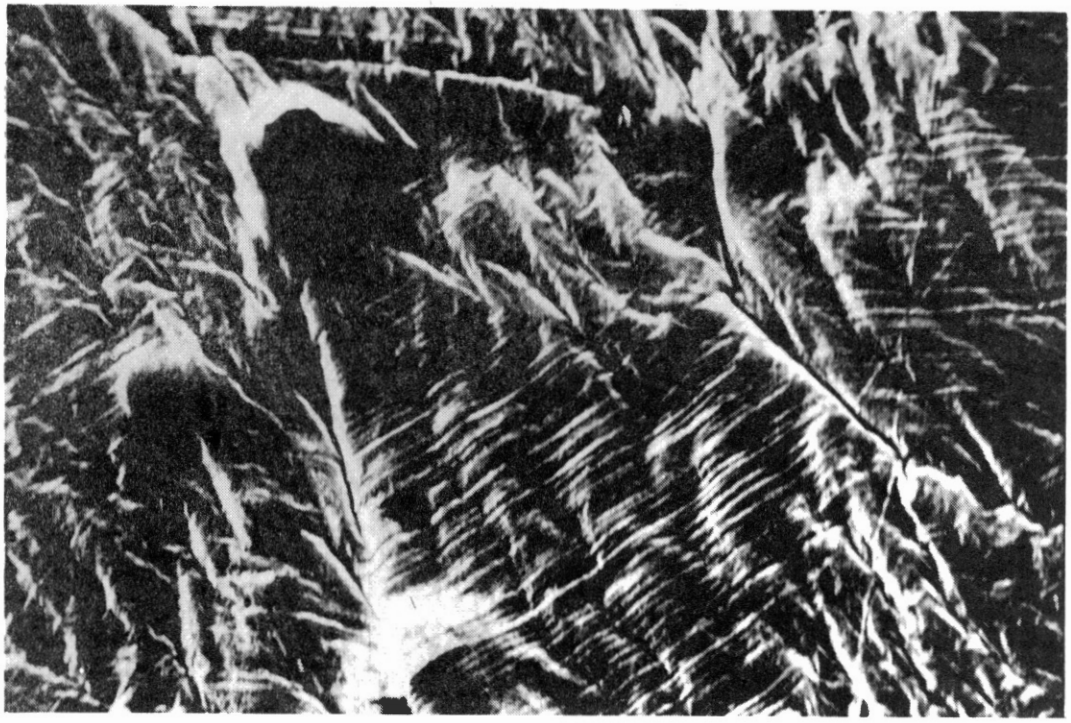

(i) Replica After 32 Cycles, 1000x

Figure 40. (Continued)

(j) Replica After 32 Cycles, 2000x

Figure 40. (Continued)

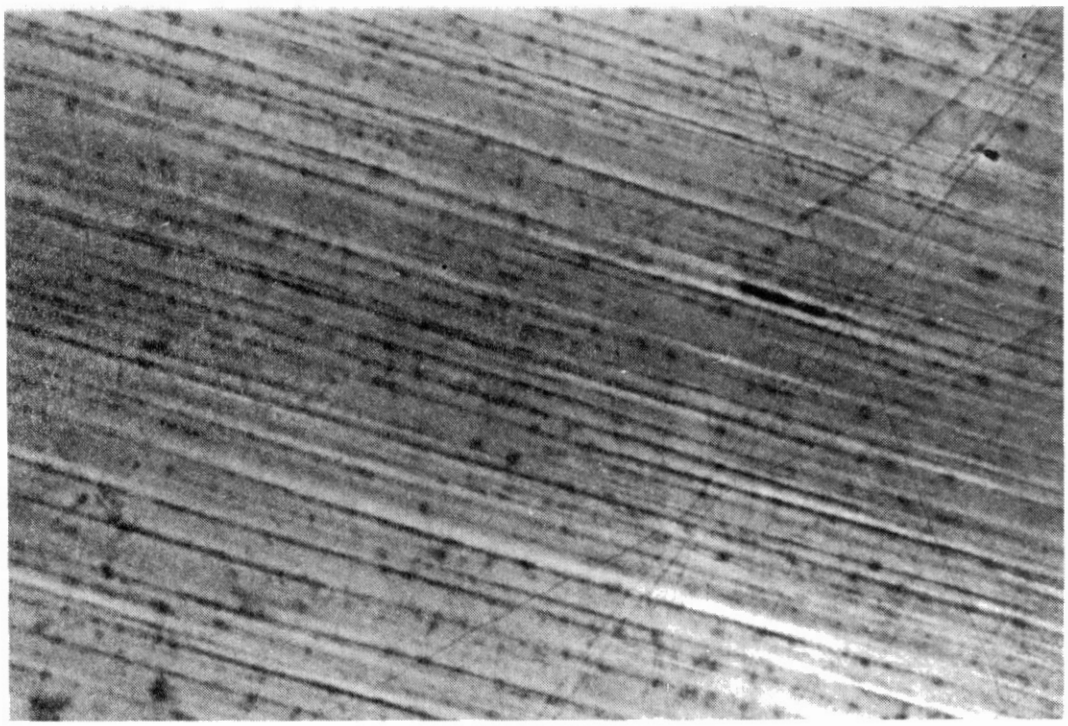

(k) Real Specimen After 32 Cycles, 1000x

Figure 40. (Continued)

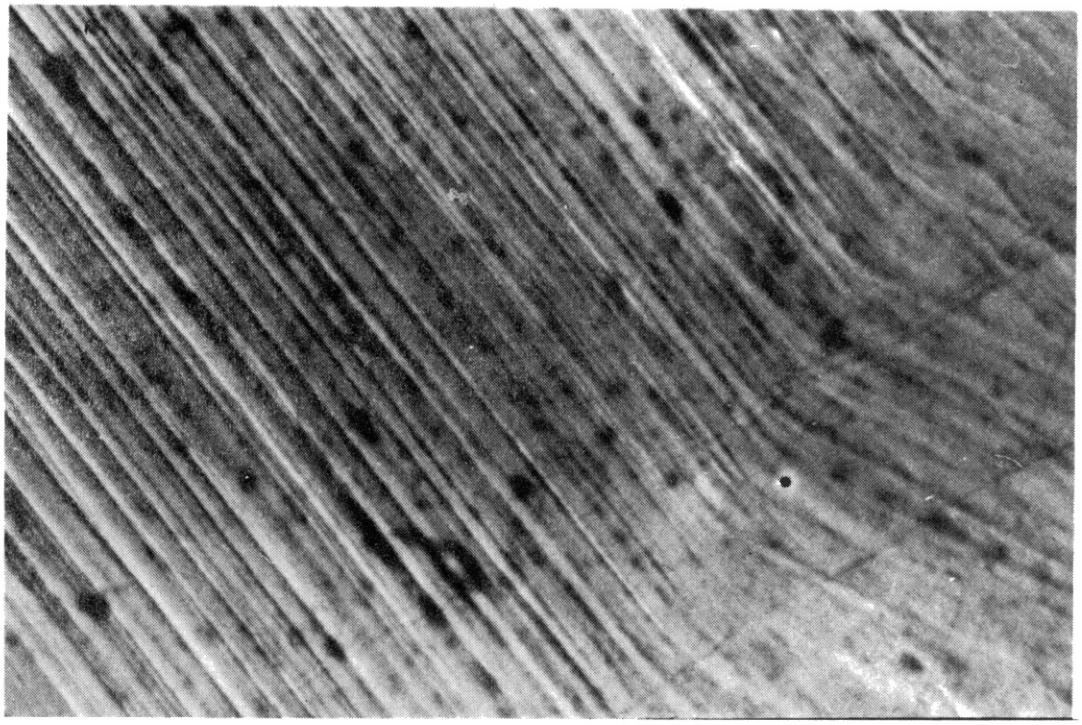

(1) Real Specimen After 32 Cycles, 2000x

Figure 40. (Continued)

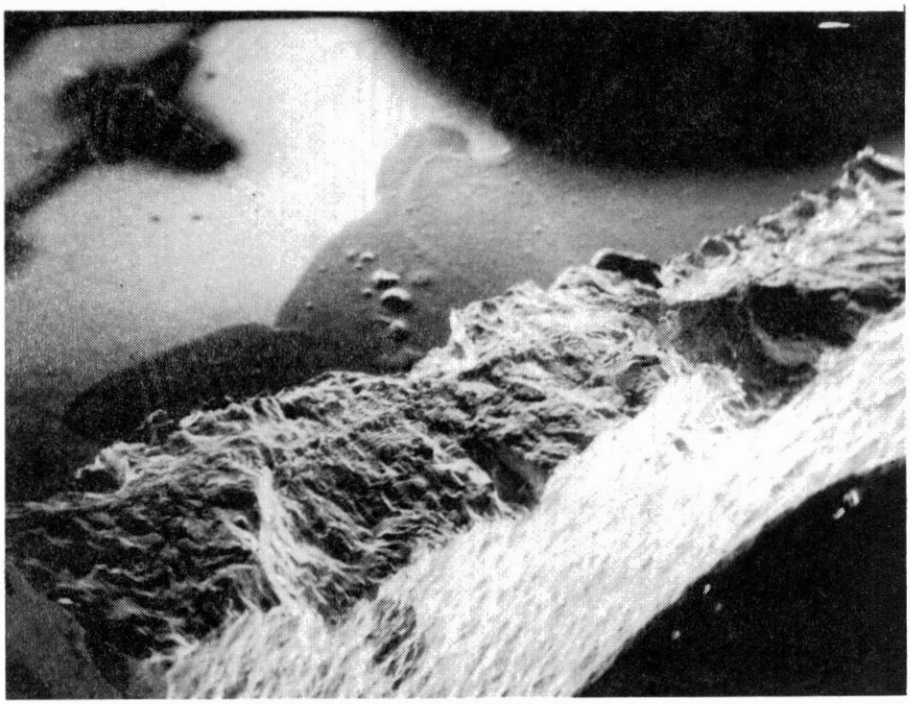

(a) Fracture Surface of Specimen at 50x

Figure 41. Scanning Electron Micrographs of the Fracture Surface

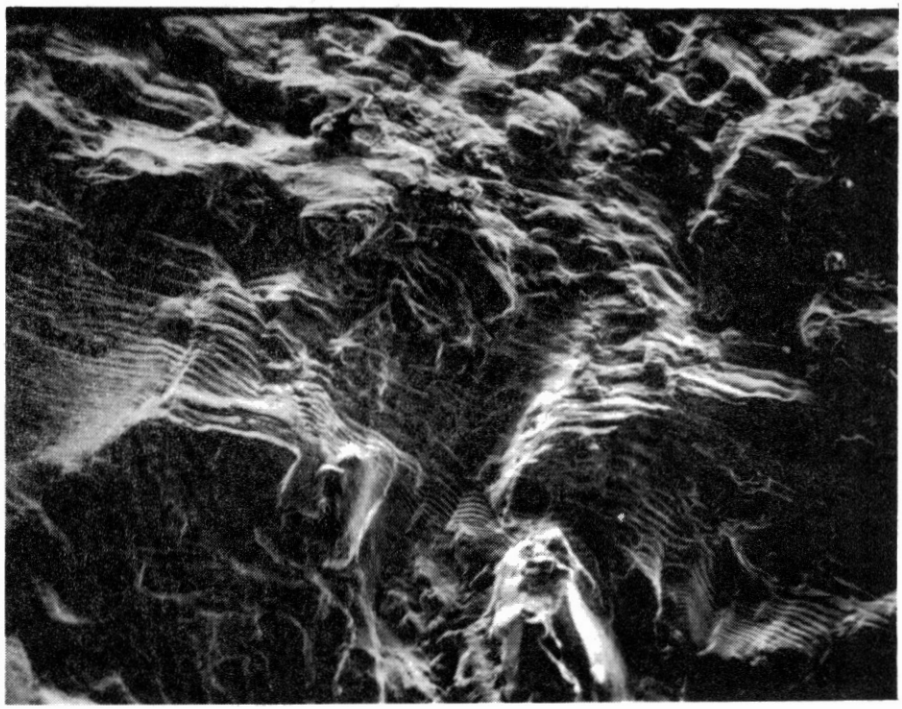

(b) Fracture Surface of Specimen at 100x

Figure 41. (Continued)

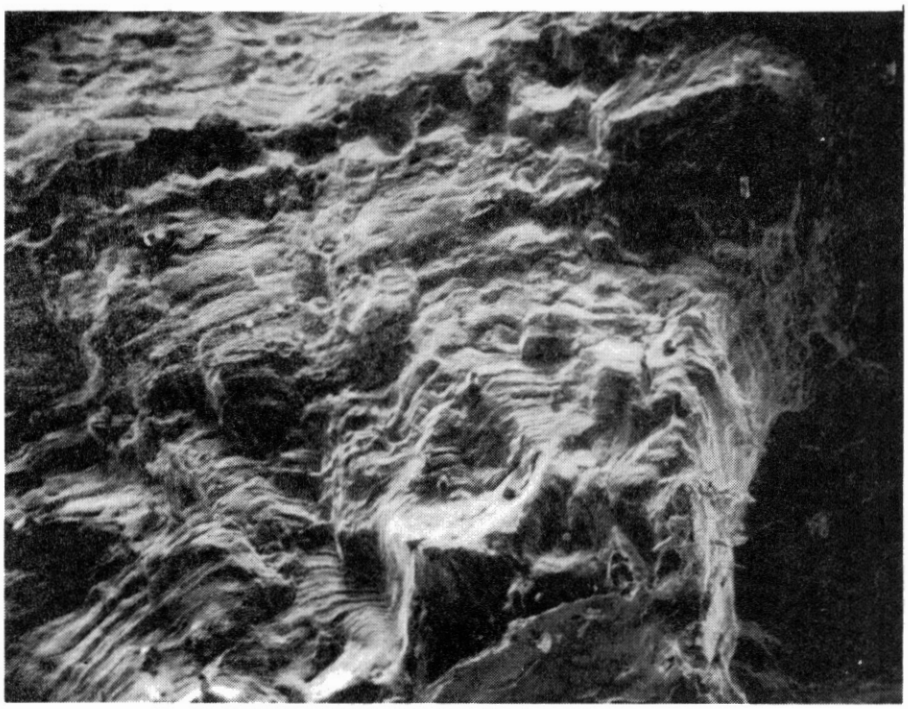

(c) Fracture Surface of Specimen at 200x

Figure 41. (Continued)

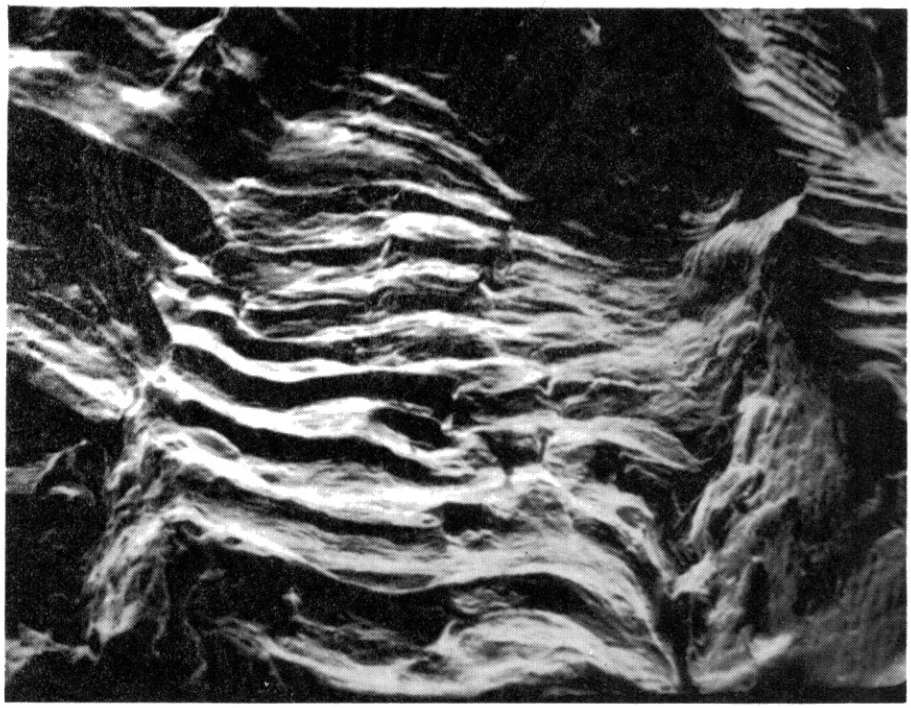

(d) Fracture Surface of Specimen at 700x

Figure 41. (Continued)

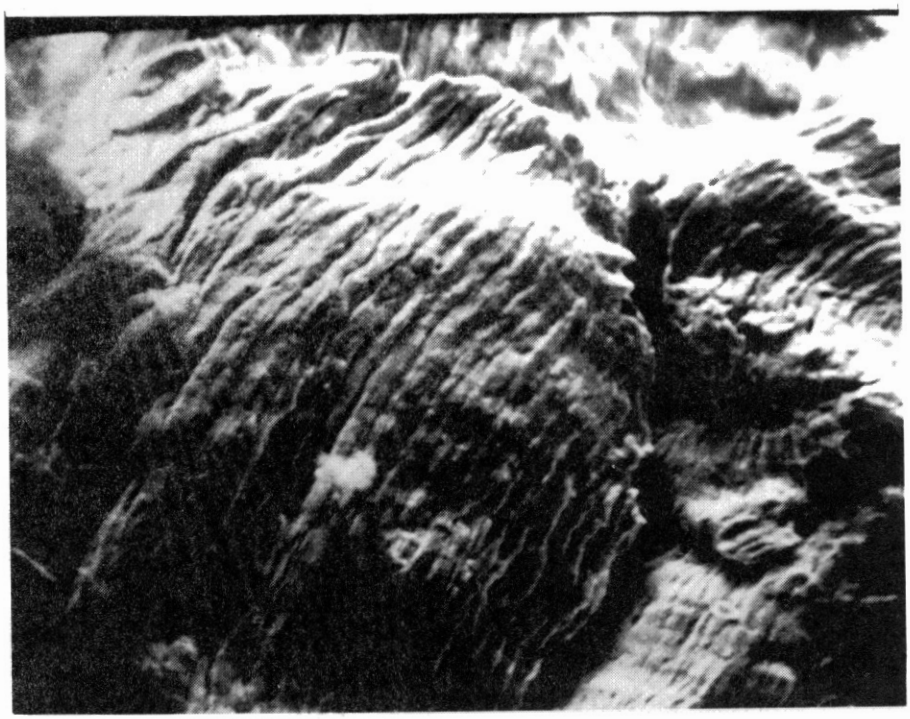

(e) Fracture Surface of Specimen at 1000x

Figure 41. (Continued)

APPENDIX C

SUMMARY OF TABULATED SURFACE HARDNESS VALUES FOR ANNEALED NICKEL 200 ALLOY SPECIMENS SUBJECTED TO FULLY REVERSED BENDING

Surface Hardness Data Form

Date of Test 12/12/77 Spec. No. 4A Surface Treatment Vacuum Annealed

Temperature: Start 71°F End 72°F

Relative Humidity: Start 52% End 54%

Specimen Size: Standard X Long ___

Indenter: Vickers X Knoop ___

Eccentricity Setting No. 1 Vernier Setting 16.7

d_1 / d_2

d_{avg}

Hv

N \ W	15 gr	50 gr	200 gr	300 gr	500 gr
N = 0	14.0 / 14.2	29.4 / 27.2	58.0 / 56.2	77.0 / 70.0	101.6 / 100.0
	14.15	28.30	57.10	73.50	100.80
	141	116	114	103	91
N = 1/2	13.6 / 13.6	25.0 / 26.6	54.9 / 55.0	69.4 / 69.8	90.8 / 92.6
	13.60	25.80	54.95	69.60	91.70
	150	139	123	115	111
N = 1	12.2 / 12.0	24.4 / 25.0	52.0 / 55.0	69.0 / 69.0	89.1 / 88.6
	12.10	24.70	53.50	69.00	88.85
	190	152	130	117	116
N = 2	11.9 / 12.0	25.0 / 24.3	53.5 / 52.0	65.5 / 66.5	87.0 / 86.0
	11.95	24.65	52.75	66.00	86.50
	194	153	134	128	124
N = 4	11.4 / 11.9	24.0 / 22.6	50.5 / 52.0	63.0 / 64.6	84.5 / 83.5
	11.65	23.30	51.25	63.80	84.00
	204	171	142	137	131
N = 8	11.4 / 11.3	22.2 / 23.0	50.0 / 52.0	63.0 / 62.1	80.5 / 83.5
	11.35	22.60	51.00	62.55	82.00
	216	182	143	143	138
N = 16	11.1 / 10.8	21.0 / 23.0	51.0 / 50.0	61.7 / 62.0	81.0 / 83.0
	10.95	22.00	50.50	61.85	82.00
	232	192	145	146	138
N = 32	10.8 / 10.9	22.0 / 21.0	49.1 / 48.6	64.0 / 63.1	78.0 / 80.0
	10.85	21.50	48.85	63.55	79.00
	238	201	156	138	189
N = 64	10.8 / 11.5	22.0 / 21.0	49.6 / 48.2	61.2 / 62.0	82.6 / 82.2
	11.15	21.50	48.90	61.60	82.4
	224	201	155	149	137

Comments: Initial cracks appeared at cycles; specimens failed at N_f = 821 cycles.

Surface Hardness Data Form

Date of Test _____ Spec. No. __ Surface Treatment Vacuum Annealed

Temperature: Start ____ End ____

Relative Humidity: Start ____ End ____

Specimen Size: Standard X Long ___

Indenter: Vickers X Knoop ___

Eccentricity Setting No. 1 Vernier Setting ____

d_1 / d_2

d_{avg}

Hv

Summary

N \ W	15 gr	50 gr	200 gr	300 gr	500 gr
N = 0	142	126	111	101	97
N = 1/2	153	140	123	116	111
N = 1	159	152	128	121	116
N = 2	164	156	133	125	124
N = 4	180	163	137	131	129
N = 8	192	178	148	144	136
N = 16	205	188	153	151	145
N = 32	202	191	156	158	151
N = 64	211	194	159	159	155

Comments:

Surface Hardness Data Form

Date of Test _____ Spec. No. __ Surface Treatment Vacuum Annealed

Temperature: Start ____ End ____

Relative Humidity: Start ____ End ____

Specimen Size: Standard X Long ___

Indenter: Vickers X Knoop ___

Eccentricity Setting No. 2 Vernier Setting ____

d_1 / d_2

d_{avg}

Hv

Summary

N \ W	15 gr	50 gr	200 gr	300 gr	500 gr
N = 0	133	126	113	103	99
N = 1/2	143	136	121	114	107
N = 1	151	141	127	118	113
N = 2	160	149	133	125	124
N = 4	167	153	137	129	126
N = 8	179	158	142	135	131
N = 16	183	162	148	141	136
N = 32	196	171	156	147	145
N = 64	201	171	155	151	144

Comments:

Surface Hardness Data Form

Date of Test _____ Spec. No. __ Surface Treatment Vacuum Annealed

Temperature: Start ____ End ____

Relative Humidity: Start ____ End ____

Specimen Size: Standard X Long ___

Indenter: Vickers X Knoop ___

Eccentricity Setting No. 3 Vernier Setting ____

d_1 / d_2

d_{avg}

Hv

Summary

N \ W	15 gr	50 gr	200 gr	300 gr	500 gr
N = 0	130	123	112	96	98
N = 1/2	140	132	118	104	105
N = 1	151	143	127	112	112
N = 2	160	151	132	118	121
N = 4	167	155	138	130	126
N = 8	170	158	140	133	128
N = 16	178	160	146	138	135
N = 32	184	172	150	151	147
N = 64	200	180	151	151	149

Comments:

Surface Hardness Data Form

Date of Test _____ Spec. No. __ Surface Treatment Vacuum Annealed

Temperature: Start ____ End ____

Relative Humidity: Start ____ End ____

Specimen Size: Standard X Long ___

Indenter: Vickers X Knoop ___

Eccentricity Setting No. 4 Vernier Setting ____

d_1 / d_2

d_{avg}

Hv

Summary

N \ W	15 gr	50 gr	200 gr	300 gr	500 gr
N = 0	128	125	112	58	95
N = 1/2	142	130	117	106	102
N = 1	147	134	120	110	108
N = 2	155	137	123	112	110
N = 4	159	141	126	120	112
N = 8	164	145	129	124	119
N = 16	172	151	135	132	126
N = 32	185	152	137	140	135
N = 64	208	156	142	146	140

Comments:

Surface Hardness Data Form

Date of Test _____ Spec. No. __ Surface Treatment Vacuum Annealed

Temperature: Start ____ End ____

Relative Humidity: Start ____ End ____

Specimen Size: Standard X Long ___

Indenter: Vickers X Knoop ___

Eccentricity Setting No. 5 Vernier Setting ____

d_1 / d_2

d_{avg}

Hv

Summary

N \ W	15 gr	50 gr	200 gr	300 gr	500 gr
N = 0	126	124	112	99	97
N = 1/2	133	127	114	105	100
N = 1	139	126	116	106	103
N = 2	142	129	119	107	105
N = 4	145	129	120	108	107
N = 8	156	133	122	111	105
N = 16	170	136	123	115	110
N = 32	174	141	125	118	112
N = 64	190	149	129	125	119

Comments:

APPENDIX D

COMPLETE SET OF DRAWINGS FOR CONSTRUCTION OF THE EXPERIMENTAL BENDING MACHINE

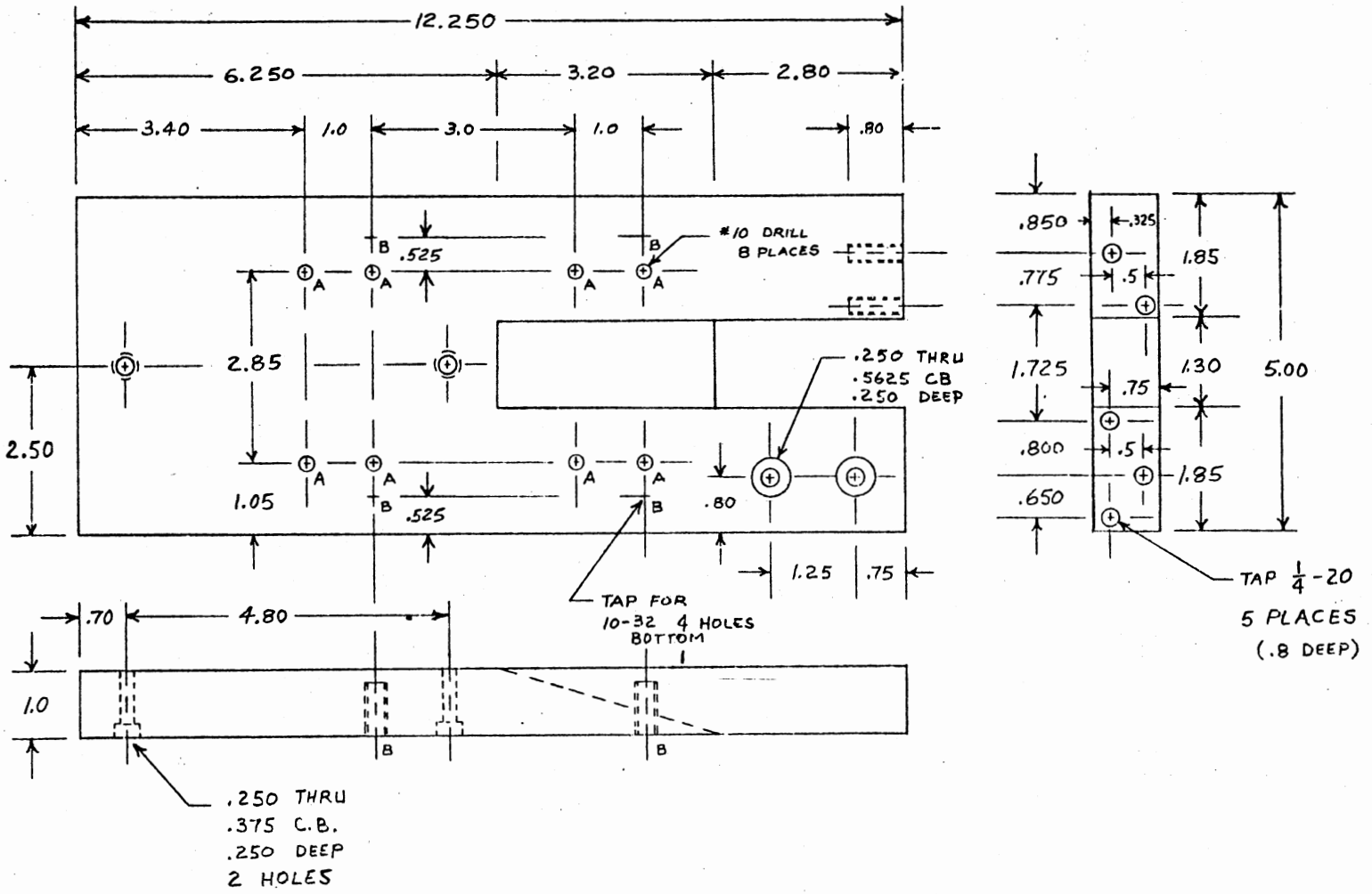

Figure 42. Mounting Base

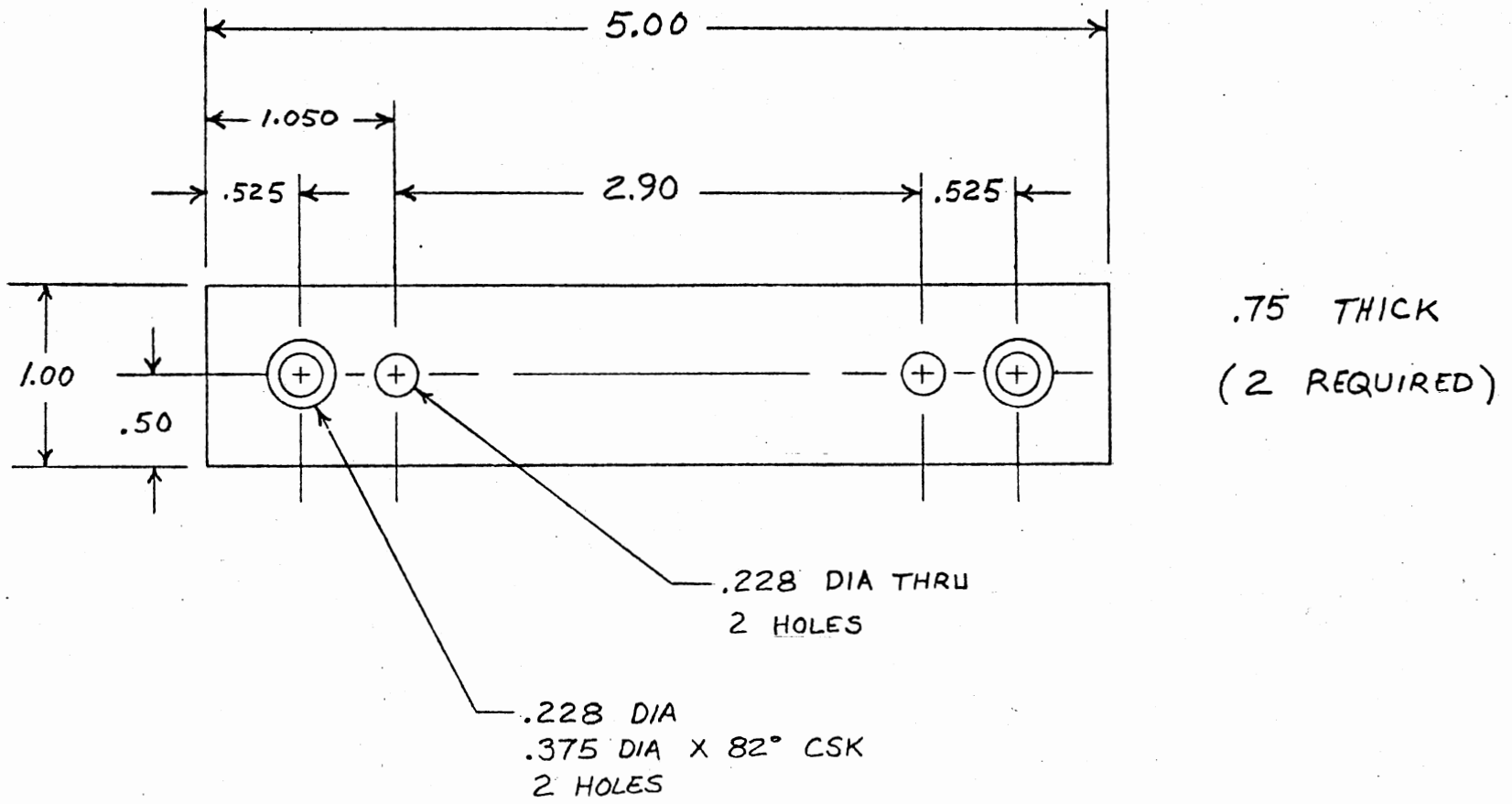

Figure 43. Mounting Base Support Block

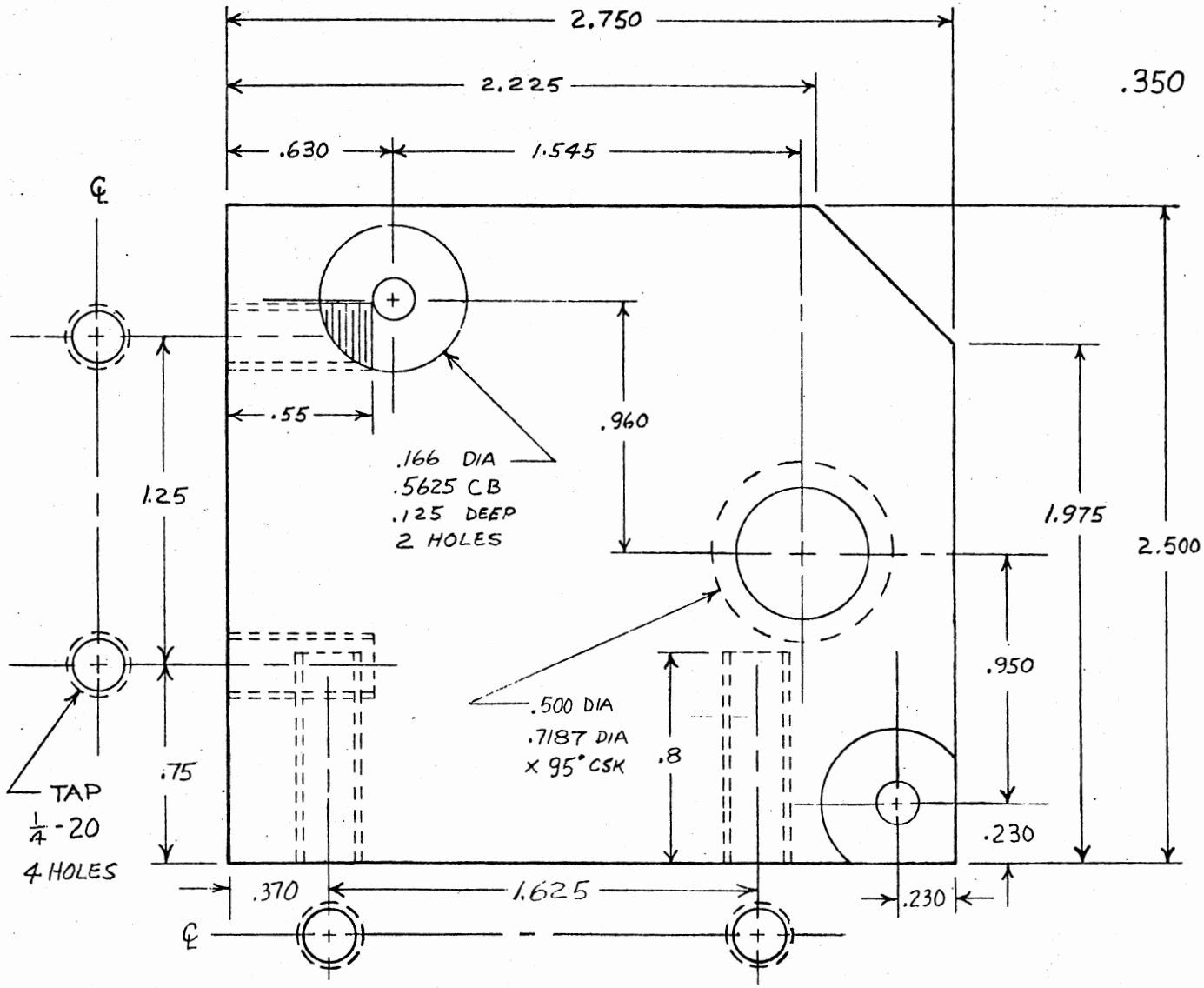

Figure 44. Electric Motor Mounting Block

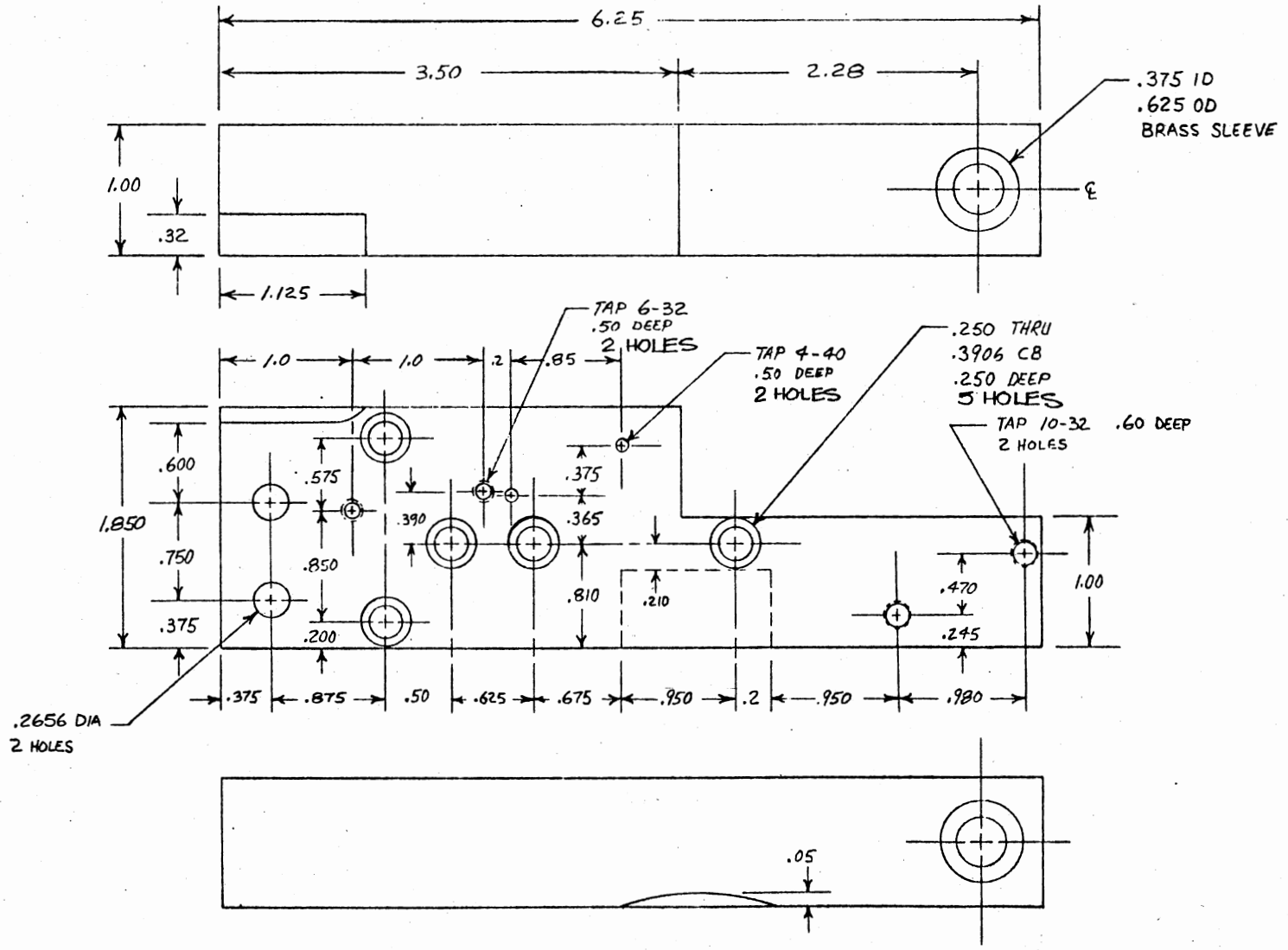

Figure 45. Motor and Drive Gear Support

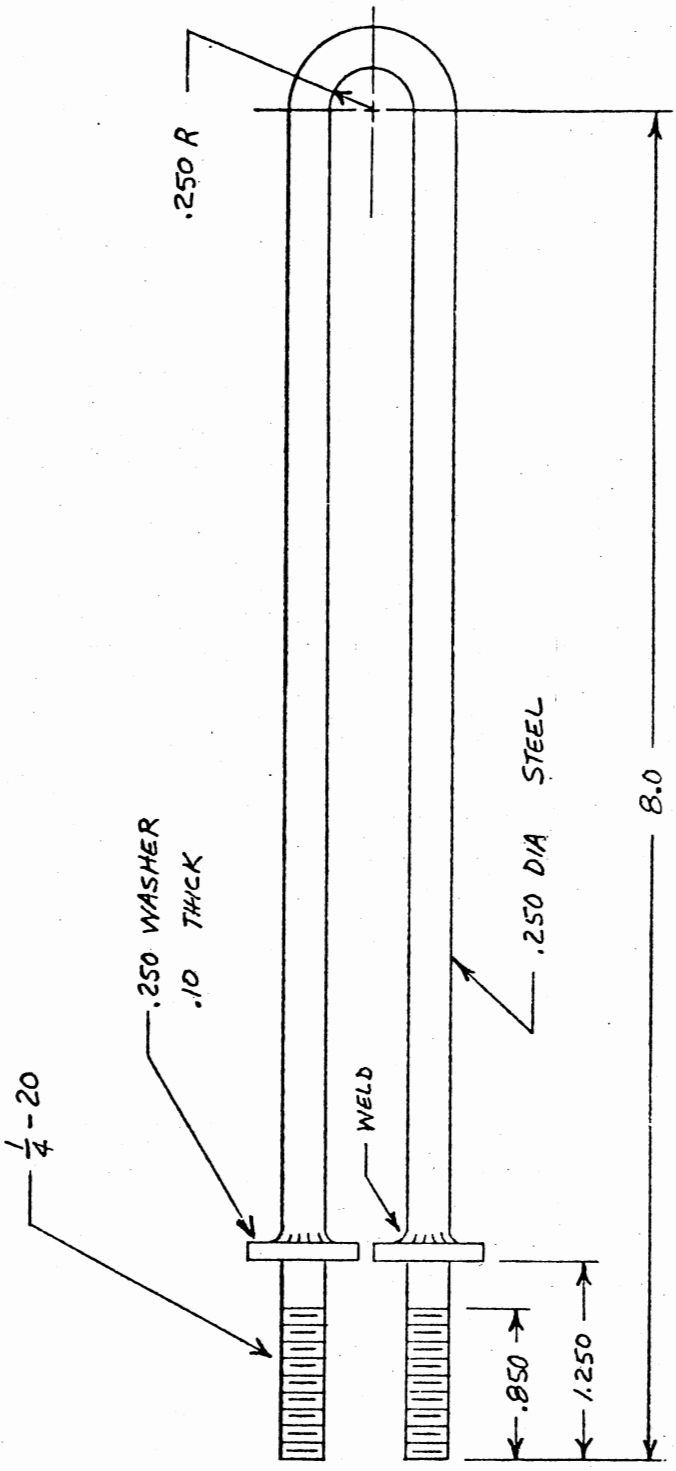

Figure 46. Microswitch Support Rod

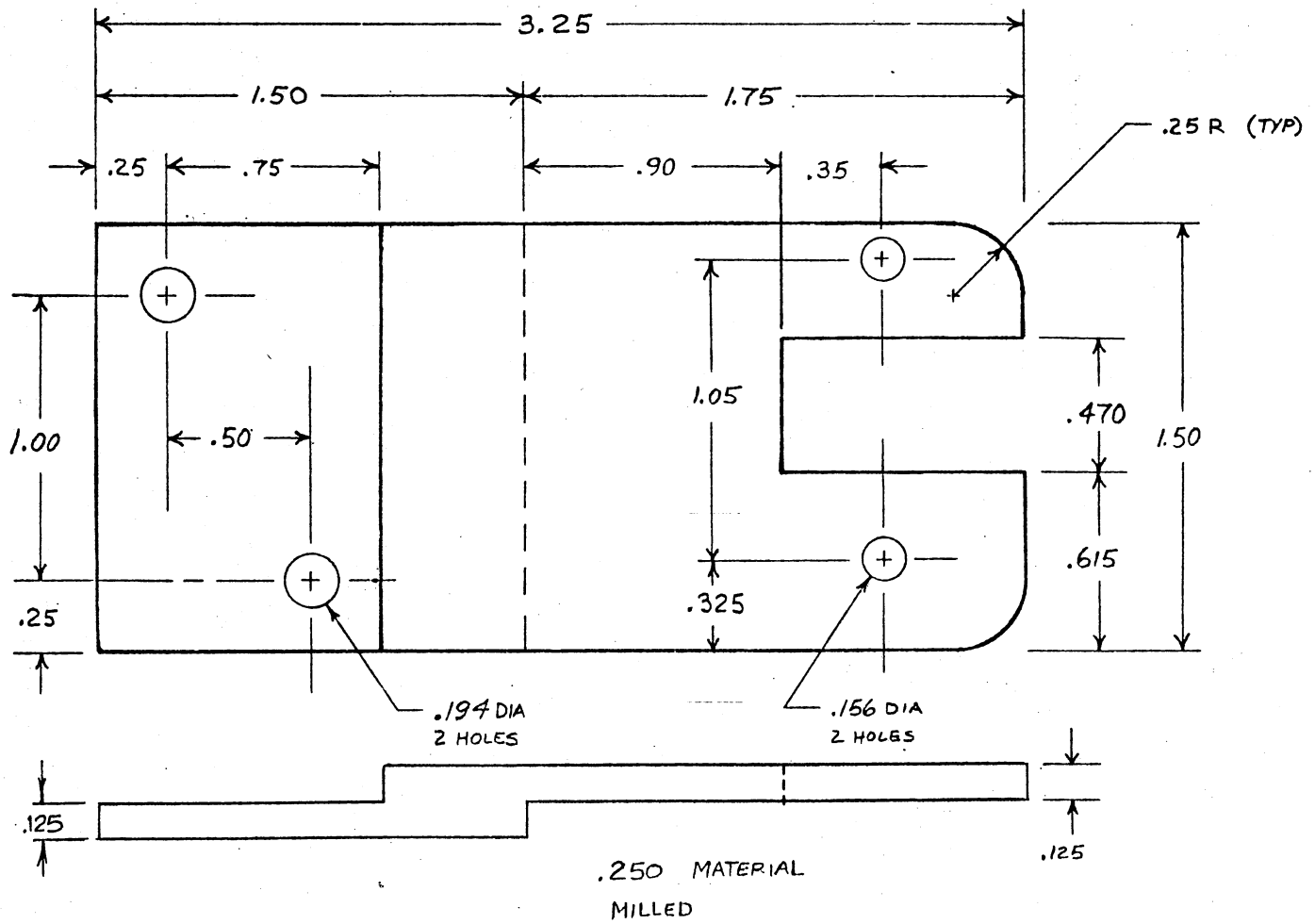

Figure 47. Counter Support Plate

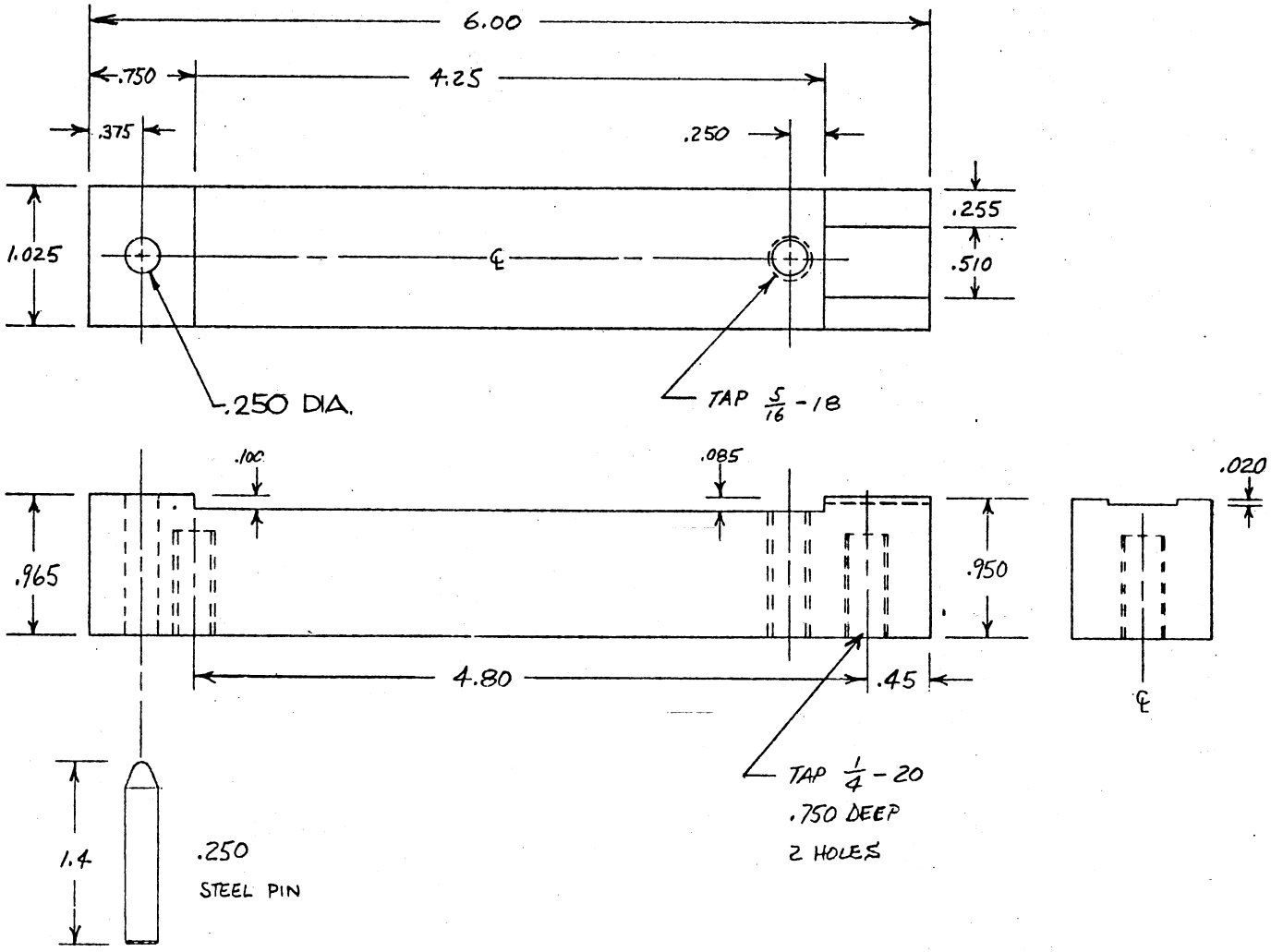

Figure 48. Fixed Clamping Jaw, Lower Part

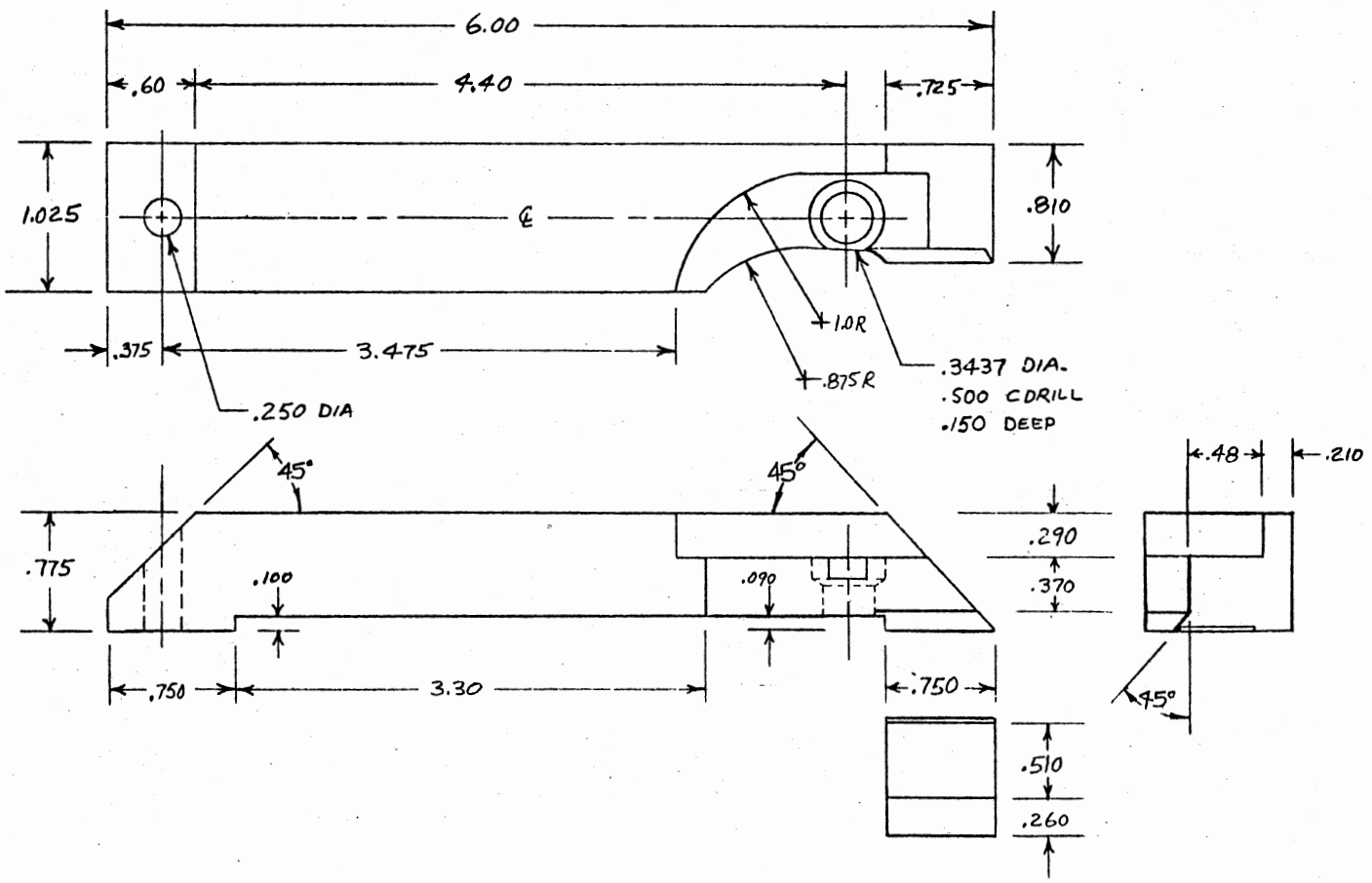

Figure 49. Fixed Clamping Jaw, Upper Part

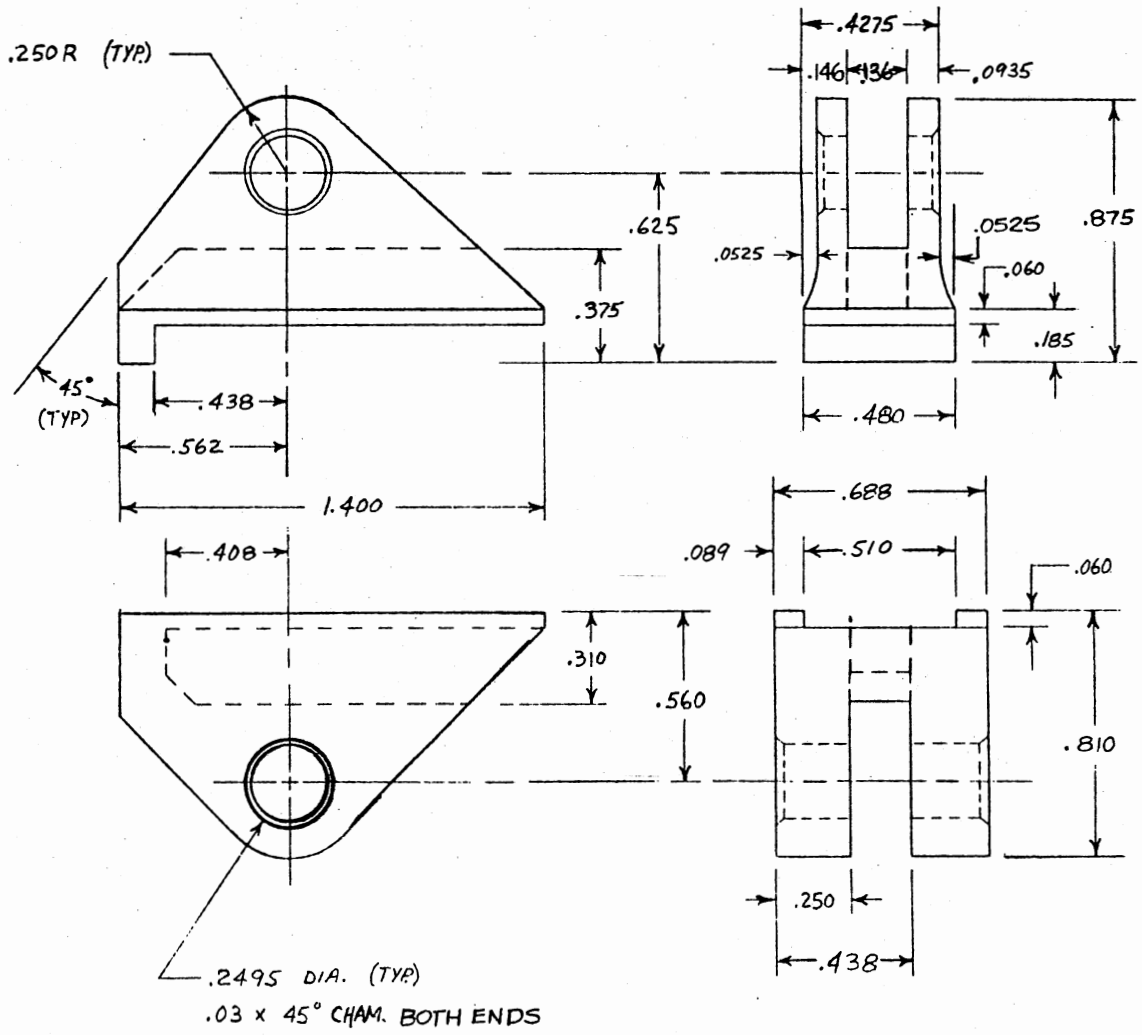

Figure 50. Movable Chuck Clamping Jaws

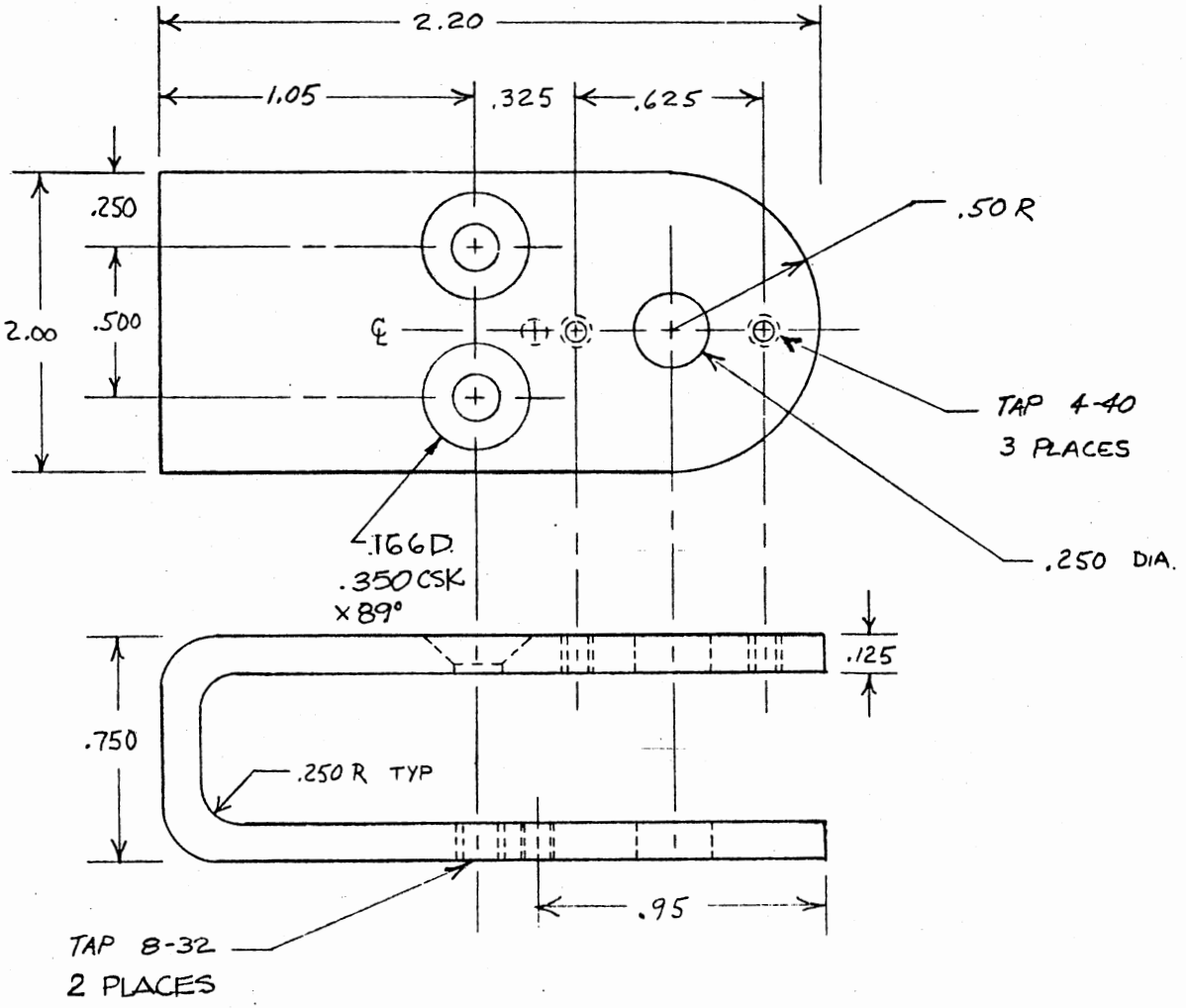

Figure 51. Movable Clamp Mounting Support

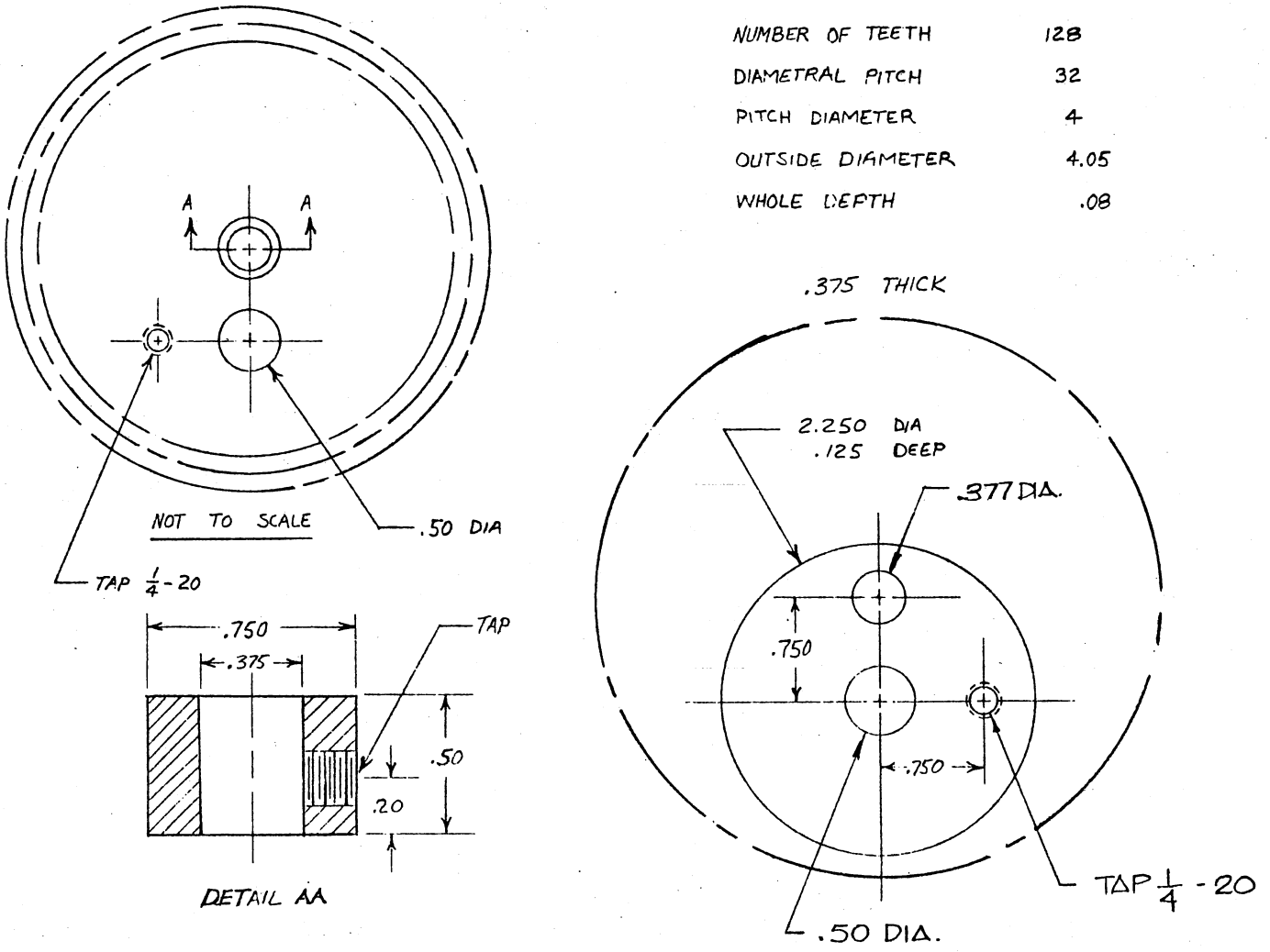

Figure 52. Main Gear, Eccentric Cam

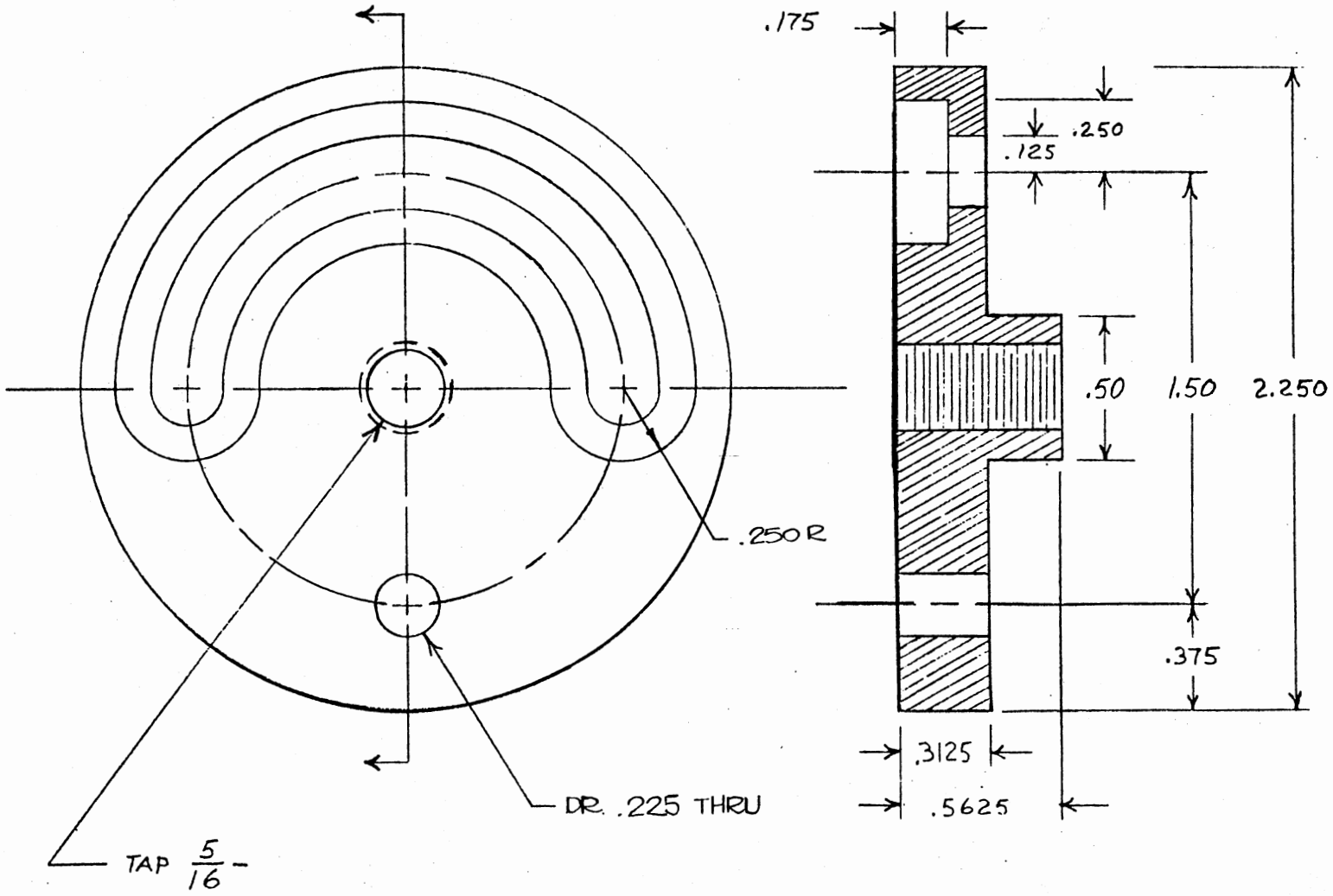

Figure 53. Eccentric Loading Cam

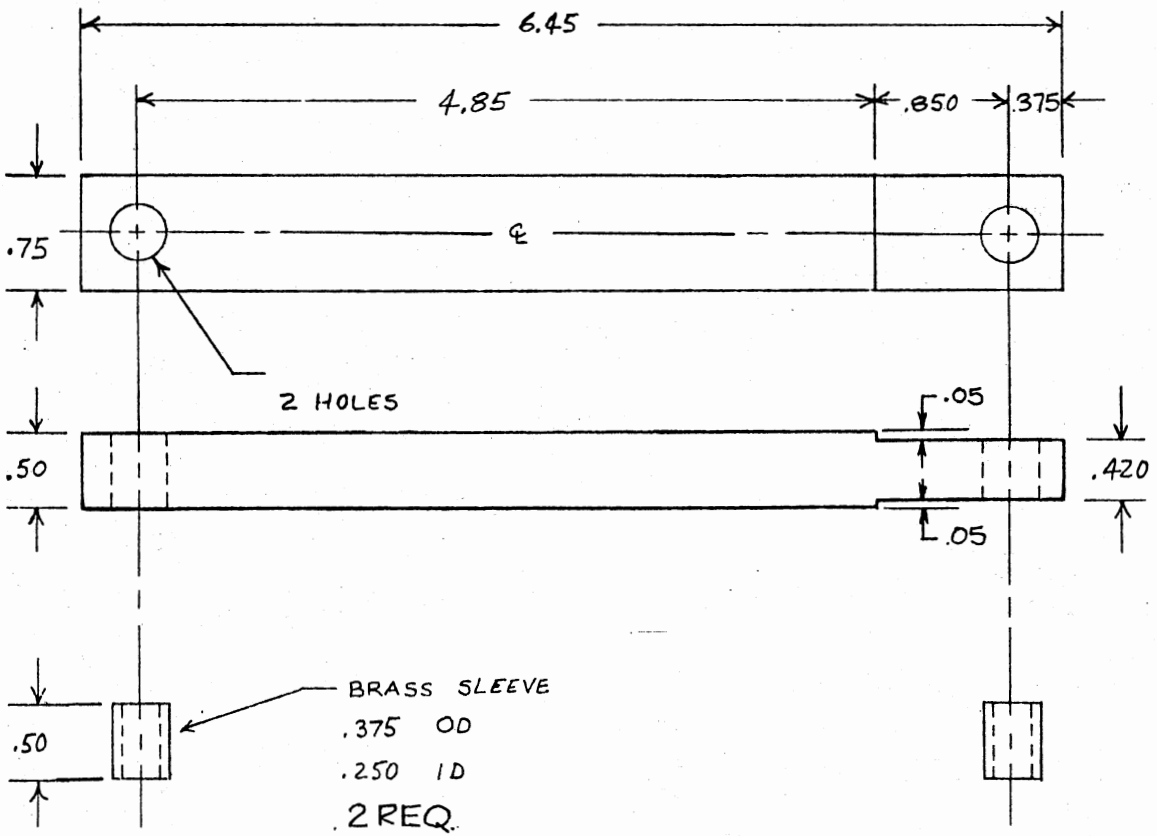

Figure 54. Loading Connecting Rod, Brass Sleeve

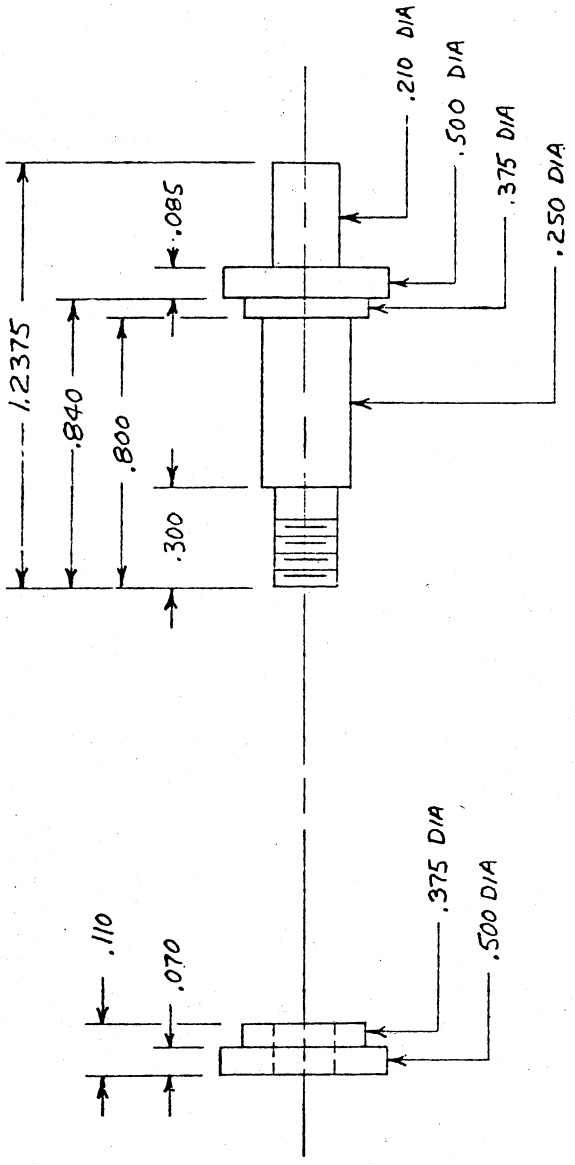

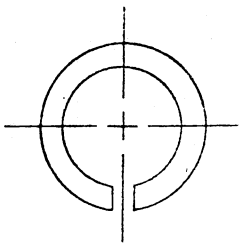

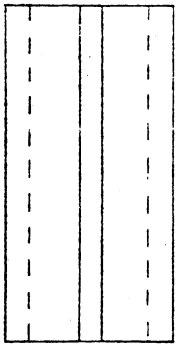

Figure 55. Drive Shaft, Sleeve, and Bushing

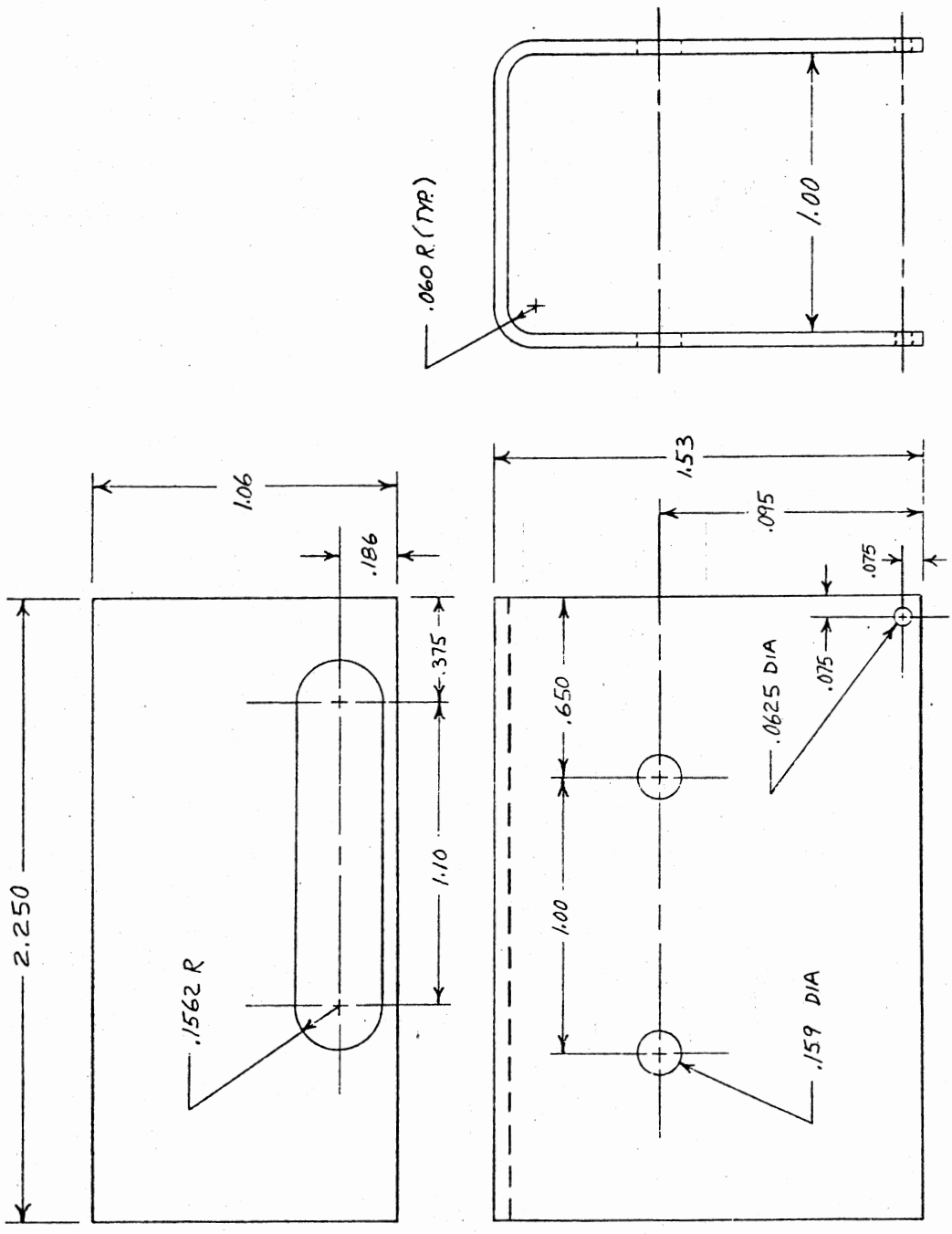

Figure 56. Microswitch Housing

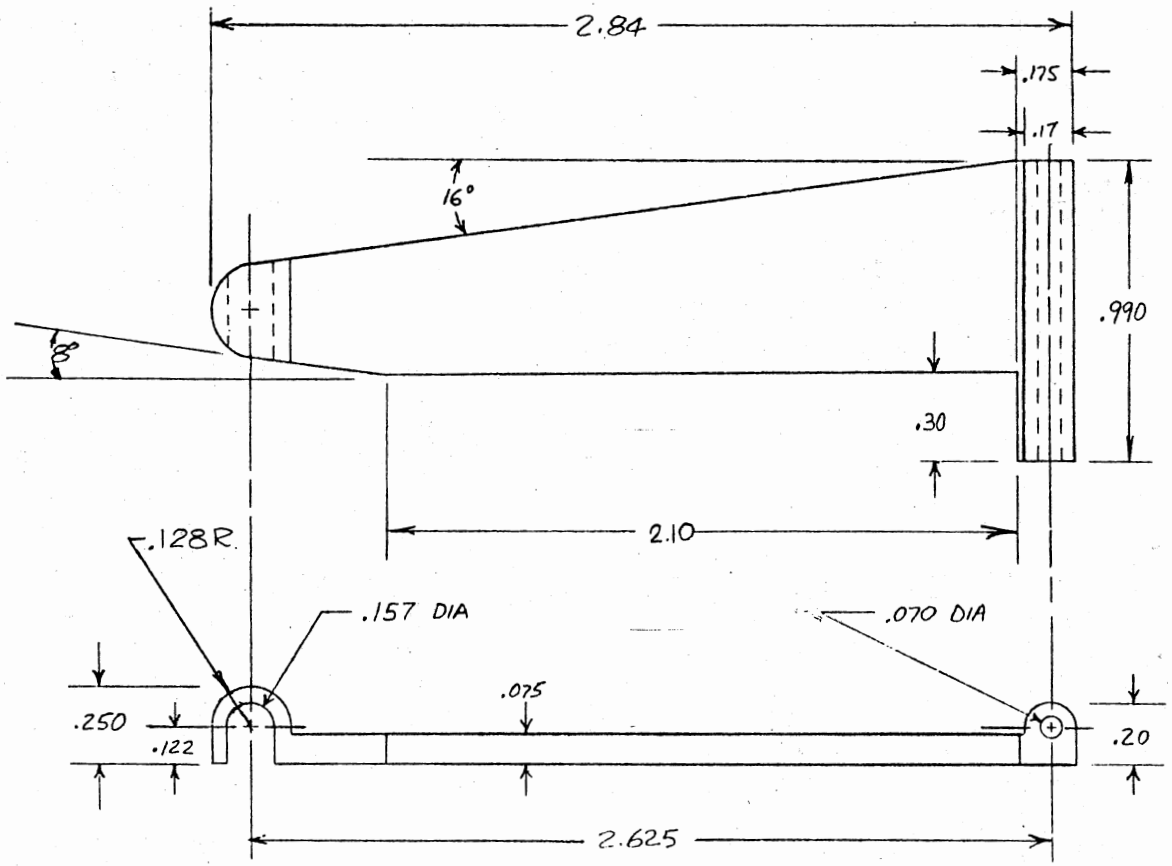

Figure 57. Microswitch Release Flapper

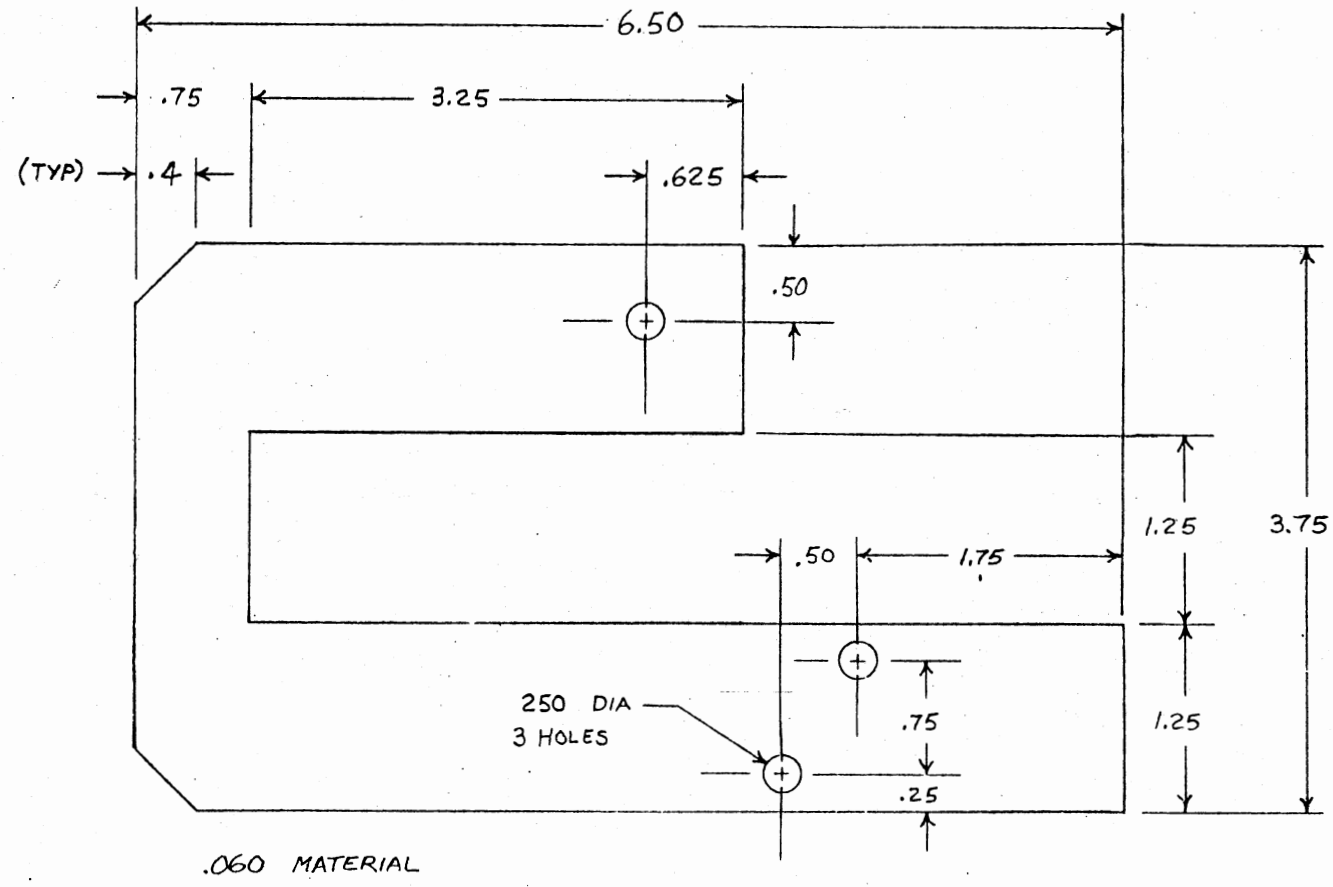

Figure 58. Guard Plate

VITA[2]

Jesa H. Kreiner

Candidate for the Degree of

Doctor of Philosophy

Thesis: A STUDY OF SURFACE ZONE DETERIORATION OF NICKEL LEADING TO FATIGUE CRACK INITIATION IN LOW CYCLE FATIGUE

Major Field: Mechanical Engineering

Biographical:

Personal Data: Born in Belgrade, Yugoslavia, on November 16, 1934, the son of Herman and Marija Krajner. Married to Yael Shildkrout, August 23, 1970; father of son Gideon and daughter Abigail.

Education: Graduated from Public High School #8, Belgrade, Yugoslavia, 1954. Received the Degree of Diplom Ingineur from the University of Belgrade in February, 1961. Completed requirements for the Doctor of Philosophy degree at Oklahoma State University in May, 1979.

Professional Experience: Twelve years of industrial experience; thirteen years of teaching experience, and twelve technical publications.

Organizations: American Society for Engineering Education; Society for Advancement of Materials and Process Engineering; United Professors of California; American Society of Mechanical Engineers; Society of Manufacturing Engineers; American Society for Metals; Louisiana Engineering Society; member of Sigma Pi Sigma (national honorary fraternity).